Simulating Star Formation in Molecular Cloud Cores

by

Rhianne Attwood

A thesis submitted to the

University of Wales

for the degree of

Doctor of Philosophy

September 2008

ProQuest LLC
789 East Eisenhower Parkway
P.O. Box 1346
Ann Arbor, MI 48106-1346

ACKNOWLEDGMENTS

First and foremost, I would like to thank my supervisor, Professor Ant Whitworth, for all his support over the last 4 years, as a supervisor, and as a friend. This thesis would certainly not exist without his help and advice. I would also like to thank him for his keen eye for my particularly bad grammar. I am forever in his debt, thank you Ant. I would also like to thank Dimitris Stamatellos for all his help with the work presented in this thesis, as well as his patience for dealing with my continual, often stupid, questions. I hope you like working on my two desks, take care of them.

Thank you to all the other members of our, now somewhat busy, office. A special thank you goes to several other star formers, past and present, including David Hubber for our serious conversations about numerical codes, and even more serious conversations about the affairs of Welsh Rugby. Thanks also goes to Sumedh Anathpindika, Thomas Bisbas, Annabel Cartwright, Richard Wunsch and Derek Ward-Thompson. Simon Goodwin, thanks for allowing me to use and break DRAGON, and for then explaining how to use and not break DRAGON.

I'd also like to thank the many friends I have made in Cardiff. Dave Nutter, thank you for putting up with my random questions about observational astronomy, which would often start, 'You know like, observations and stuff, ...'. My tea time breaks won't be the same without you. Thank you to James for keeping me sane for all, or maybe most, of the time I was writing up. Your timing for suggesting a visit to the pub was impeccable. I'll always remember all the great Friday evenings spent in the Tut 'n' Shive (or 33 The Place if we were feeling flush) with James, Bruce & Emma, Rob & Jane, Pete and Andreas, followed by a trip to Kismet for a five pound three-course meal. I'll miss those nights.

Becki thank you for being so understanding about how terrible I am at keeping in touch, even though we just slip back into the conversation. To the Poola guys, thanks for making Saturday afternoons so much fun, regardless of how incredibly good or incredibly bad the rugby is. Supporting Pontypool RFC has almost been as challenging as completing this PhD.

Thank you to Douglas for putting up with me through all of this, you have been my rock. Last but most certainly not least, I'd like to thank my family for all their love and support, not just for the last few years but throughout. Mam, Dad, Anna, Ross and Ashley, thank you.

ABSTRACT

In this thesis we investigate the influence of certain physical effects on the collapse and fragmentation of isolated, low-mass, low-turbulence cores, in particular on the mass distribution, binary statistics and kinematics of the resulting stars.

We perform numerical simulations using a Smoothed Particle Hydrodynamics code to model this mode of star formation. Firstly we model acoustic oscillations of a self-gravitating isentropic monatomic gas sphere using our SPH code and find that if the smoothing lengths are adjusted so as to keep the number of neighbours in the range $N_{\rm NEIB} \pm \Delta N_{\rm NEIB}$, $\Delta N_{\rm NEIB}$ should be set to zero, to reduce the level of numerical dissipation and diffusion. We suggest that this should become a standard test for codes simulating star formation, since pressure waves generated by the switch from approximate isothermality to approximate adiabaticity play a crucial role in the fragmentation of collapsing cores.

We perform a large ensemble of SPH simulations of cores having different levels of turbulence, using a new, more realistic treatment of thermodynamics, developed by Stamatellos et al. (2007), which takes into account the thermal history of protostellar gas and captures the thermal inertia effects. We compare the results with simulations using a standard barotropic equation of state. We find that increasing the level of turbulence generally tends to reduce the fraction of the core mass which is converted into stars, and increase the number of stars formed by a single core. Using the new treatment results in more protostellar objects being formed, and a higher proportion of brown dwarfs. Of the multiple systems that form, they tend to have shorter periods, higher eccentricities and higher mass ratios. We also note that in our simulations the process of fragmentation is often bimodal, in the following sense. The first protostar to form is usually, at the end, the most massive, i.e. the primary. However, frequently a disc-like structure subsequently forms round this primary, and then, once it has accumulated sufficient mass, quickly fragments to produce several secondaries. We believe that this delayed fragmentation of a disc-like structure is likely to be an important source of very low-mass stars in nature (both low-mass hydrogen-burning stars and brown dwarf stars).

We also model the evolution of an ensemble of prestellar cores in the Ophiuchus Main

Cloud using initial conditions for the sizes and levels of turbulence constrained by the observations of Motte et al. (1998) and André et al (2007), and the recently revised core masses of Stamatellos et al. (2007). We find that star formation in these core is extremely efficient with typically the formation of a single star, but we also see the formation of multiple systems in a number of cores. We find that the number of stars formed by a core is highest if the core has high mass, and/or if it has a high initial level of turbulence, and/or if it starts from a low initial density. We explain why.

Finally we explore the effect metallicity has on the mass distribution and binary statistics of stars formed from low-mass low-turbulence cores. We find that reducing the metallicity decreases the number of stars formed from a single core and reduces the number of brown dwarfs formed. It also reduces the binary frequency.

Contents

List of Figures

List of Tables

Chapter 1

Introduction

Star formation is a dynamical, violent process, which we do not yet fully understand. The aim of astronomy is to understand how the Universe has previously evolved and will continue to evolve. Since stars influence the structure of galaxies, which are an important element in the structure of the universe, star formation plays a powerful and crucial role.

Over the last few decades there have been some major developments in the observational techniques used to study star formation. We have seen the introduction of infrared (IR) telescopes, such as IRAS and Spitzer, and also sub-millimetre telescopes such as JCMT. We can now map clouds at a higher sensitivity than ever before, and even observe young stellar objects and determine their properties, without the problems of dust obscuration as in optical observations. The future of star formation research is also very promising, with the commissioning of SCUBA-2, a second generation instrument, designed to map large areas of sky up to 1000 times faster than SCUBA. This will provide us with a phenomenal amount of data, allowing us to probe the early stages of star formation with increasing depth and accuracy.

Numerical simulations are required to explain the physics behind these observations. Star formation is a rapid, dynamical process which can scale over 20 orders of

magnitude in density, and involves self-gravitating, non-LTE fluid dynamics, so numerical simulations require very powerful modern supercomputers.

In this thesis we perform numerical simulations to gain an insight into the way in which stars are formed from dense molecular cores. Before we present the results, we shall discuss the main stages of star formation to put our results into context.

1.1 Star formation in molecular clouds

Most young stellar objects form from the contraction of dense regions in huge molecular clouds. These clouds are large condensations of interstellar gas and are concentrated in the galactic disk near the spiral arms of a galaxy. Typically, their sizes range from $\sim$ 0.1 pc to $\sim$ 100 pc in diameter, with masses from $\sim 10^2\,M_\odot$ to $\sim 10^6\,M_\odot$. Clouds with masses exceeding $10^4\,M_\odot$ tend to be called Giant Molecular Clouds (GMCs). The gas in GMCs is so cold and dense, with temperatures below 100 K and densities from 10^{-22}g cm^{-3} to 10^{-20}g cm^{-3}, that the gas is predominantly molecular hydrogen.

GMCs have a hierarchical structure, consisting of small subclouds within large subclouds. Their general structure can be mapped via molecular line observations of CO (e.g. Myers et al. 1983; Myers & Benson 1983). Observations show they tend to be filamentary in shape, rather than spherical. An example of this is shown in Fig. 1.1 for the Taurus molecular cloud. Dense clumps have been observed in molecular clouds, such as in Ophiuchus (Motte et al. 1998), also dense cores (André et al. 2007) which are thought to be the precursors of protostars. These higher density regions within the clouds can be mapped using the lines of NH_3 (e.g. Myers & Benson 1983), N_2H^+, CS and HC_3N.

One of the most intensively researched star-forming regions is Orion, which is $\sim$ 100 pc in size and has a mass of $10^5\,M_\odot$. This molecular cloud complex is located at a

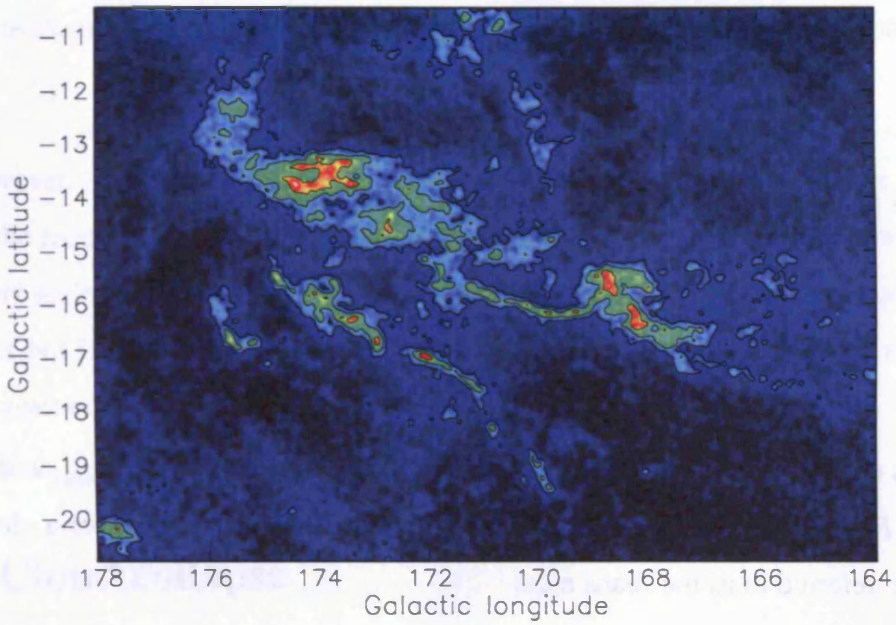

Figure 1.1: Taurus molecular cloud seen in extinction, taken from Dobashi et al. (2005) and modified by Nutter (private communication). The contour levels are A_V=1, 2, 4.

distance of $\sim$ 450 pc. A closer example is the quiescent low-mass star-forming region Taurus, which is $\sim$ 140 pc away (see Fig. 1.1). The stars most visible in Taurus are referred to as T-Tauri stars; they have masses in the range of $0.5 - 1.0\,M_\odot$, and are found in small groups of $\lesssim 10$ members. This region is smaller in size than Orion, spanning $\sim$ 20 pc. Orion is a far more violent region than Taurus, producing both high- and low-mass stars, whereas Taurus appears to produce just low-mass stars.

The actual sites of star formation are in the dense cores within molecular clouds. Here the densities are exceptionally high ($\gtrsim 10^{-20}$g cm^{-3}), and the temperatures are very low ($\lesssim$ 10 K). When a core becomes gravitationally unstable, it contracts and reaches sufficient densities for hydrogen fusion to occur. Hence, a star is formed. The first stage of star formation occurs when a molecular cloud becomes gravitationally unstable.

Consider a non-rotating, non-magnetic molecular cloud of radius R, mass M, density $\rho_\circ$ and temperaure T. If this cloud is gravitationally bound, its maximum radius is given by the Jeans length

$$R_{\text{JEANS}} \approx \left(\frac{15}{4\pi G\rho_\circ}\right)^{1/2} a_\circ, \qquad (1.1)$$

where G is the gravitational constant, $a_\circ$ is the isothermal sound speed

$$a_\circ = \left(\frac{kT}{\bar{m}}\right)^{1/2}, \qquad (1.2)$$

and $\bar{m}$ is the mean gas particle mass. This cloud will contract if $R > R_{\text{JEANS}}$, and collapse if $R \gg R_{\text{JEANS}}$. We can also define a minimum mass that is required for a cloud to be unstable, referred to as the Jeans mass

$$M_{\text{JEANS}} \approx \left(\frac{375}{4\pi}\right)^{1/2} \frac{a_\circ^3}{G^{3/2}\rho_\circ{}^{1/2}}. \qquad (1.3)$$

In this case, the cloud will contract if $M > M_{\text{JEANS}}$, and collapse if $M \gg M_{\text{JEANS}}$[1].

Substituting a temperature of $\sim$ 10K and a density of 10^{-22}gcm^{-3} for molecular hydrogen results in a Jeans length far smaller than the size of a typical molecular cloud and so these clouds should collapse. However, this is not what happens, since, if it were the case, the rate of star formation in the Galaxy would be much higher than we observe. There must be some form of support that prevents collapse occurring on freefall timescales. Thermal pressure alone is insufficient, so it is presumed that there are other supporting mechanisms. Supersonic velocity dispersions are found to exist on large scales within the clouds, which suggests the presence of turbulence (Larson 1981). This

[1]These expressions for the Jeans radius and mass are derived on the basis of the time-dependent Virial Theorem applied to a uniform-density cloud. If instead one invokes a critical Bonner-Ebert sphere, the expressions become

$$R_{\text{JEANS}} = 1.82\frac{a_\circ}{(G\rho_c)^{1/2}} = 0.763\frac{a_\circ}{(G\bar{\rho})^{1/2}},$$
$$M_{\text{JEANS}} = 4.43\frac{a_\circ^3}{G^{3/2}\rho_c^{1/2}} = 1.86\frac{a_\circ^3}{G^{3/2}\bar{\rho}^{1/2}};$$

where ρ_c is the central density, and $\bar{\rho}$ is the mean density

could provide the support against collapse. Magnetic fields may also contribute to the support.

However, searching for a mechanism to provide this additional support may not actually be required, since evidence suggests that the lifetime of a cloud is less than the 1 Gyr timescale previously thought. Therefore, molecular clouds are not equilibrium structures but instead may be transient structures which assemble, produce stars, and disperse over only a few dynamical times (Elmegreen 2000).

1.2 Cloud collapse

Magnetic fields may play an integral role in regulating cloud collapse. In molecular clouds, the magnetic field is frozen to the gas, provided that the conductivity of the gas is sufficiently high. The charged particles are then constrained to move along the field lines by the Lorentz force. The neutral particles experience this Lorentz force indirectly, when they collide with charged particles and transfer momentum. This causes there to be an 'ion-neutral friction' generated when the neutrals slip relative to the ions and field, making it hard for the neutral particles to move relative to the ions.

This process can be dealt with in two ways, via Magneto-hydrodynamics, MHD. In ideal MHD, also referred to as single fluid MHD, we ignore the motion of the neutral particles relative to the ions and hence relative to the field. However, in some situations, this may not incorporate the whole process entirely and so we require non-ideal MHD, also referred to as multifluid MHD. Here, the neutral particles diffuse through the ions and the magnetic field. This is referred to as ambipolar diffusion (Mestel & Spitzer 1956). Modelling ambipolar diffusion requires at least two fluids, an ion fluid and a neutral fluid, instead of just one as in the case of ideal MHD.

The process of ambipolar diffusion results in magnetic support being lost from the

region and hence cloud collapsing occurring (Mestel & Spitzer 1956). Ambipolar diffusion is quite rapid in molecular clouds because the ionisation fraction is low, typically in the range of 10^{-8} to 10^{-6} (Caselli et al. 1998).

An indication of whether magnetic support is sufficient to prevent collapse is given by the ratio of the mass M of the cloud to the magnetic flux Φ_B through it (Mouschovias 1976)

$$\left(\frac{M}{\Phi_B}\right)_{cr} \sim \frac{0.15^{1/2}}{G} . \tag{1.4}$$

For the cloud to undergo gravitational collapse, the mass to flux ratio must exceed this critical value, making it magnetically supercritical. For it to withstand self gravity, the cloud must be magnetically subcritical, with its mass to flux ratio less than the critical value (Mouschovias & Spitzer 1976).

In a dense core, ambipolar diffusion acts to increase the mass to flux ratio, not by dissipating magnetic flux, but by redistributing the matter in the central flux tubes (Mouschovias 1976). Eventually self gravity overcomes the forces supporting the cloud causing it to become gravitationally unstable to collapse.

Once the cloud becomes gravitationally unstable, collapse proceeds. During the initial stages of collapse when the density is less than $10^{-13}\mathrm{gcm}^{-3}$, the condensation is optically thin and the gravitational potential energy released is freely radiated away at such a rate that the cloud remains isothermal at a temperature of $\simeq$ 10K. The cloud collapses on a timescale close to the freefall time,

$$t_{\mathrm{FF}} = \left(\frac{3\pi}{32G\rho_{\mathrm{o}}}\right)^{1/2} , \tag{1.5}$$

where ρ_{o} is the central density. When the density in the core exceeds $\simeq 10^{-13}\mathrm{gcm}^{-3}$, the core becomes opaque to its own radiation and so increases in temperature. Eventually, the thermal pressure in the core becomes high enough to slow down further collapse, at $\simeq$ 200K. The core then contracts quasistatically. At a temperature of 2000K, molecular

hydrogen in the core is dissociated. The energy generated from the cloud collapse is used in this dissociation and so the core remains at almost a constant temperature. Collapse of the core continues once the dissociation of hydrogen is complete and the temperature continues to increase once again. Finally, an opaque hydrostatic protostar forms at the centre. This central protostar can then accumulate mass from the surrounding infalling envelope and accretion disk.

1.3 Prestellar cores

A prestellar core represents the phase in which a gravitationally bound core has formed in a molecular cloud and evolves through gravity towards higher degrees of central condensation, but does not yet have a central protostar (André et al. 2000; Ward-Thompson et al. 2007). Sometimes this term is confused with the term 'starless core' but the term 'starless core' includes both prestellar cores *and* cores that are not gravitationally bound (and therefore presumably will not form stars). Observations of a double-peaked velocity profile with a blue shifted larger peak shows the presence of infall in these prestellar cores (Ward-Thompson et al. 1994).

Prestellar cores are very cold, and so they emit at far IR and sub-mm wavelengths. The density profiles of prestellar cores have a flattened central region and then fall as $r^{-\eta}$ with $2 \leq \eta \leq 5$ in the outer regions, until eventually merging with the background (e.g. Ward-Thompson et al. 1994; André et al. 1996; Ward-Thompson et al. 1999; André et al. 2000).

Many different factors affect the timescale on which these prestellar cores collapse to form one or multiple stars. More realistic models of core collapse include magnetic fields, turbulence and rotation. However, we must be clear what effect each of these physical processes have on the results, since many authors include all of these processes simultaneously. In this thesis, we are concerned with exploring the collapse of prestellar

cores, by means of numerical simulations, with a view to evaluating (a) how the statistical properties of the resulting protostars depend on the initial conditions, and (b) what role is played by thermal, chemical and radiative processes. Therefore, we adopt an analytic approach. That is to say, we do not seek to implement all the deterministic physical effects, and hence we do not expect to reproduce all the observed aspects of real star formation. Rather, we seek to establish whether particular physical effects, namely the thermal and radiative processes, influence the outcome in a systematic way. Given the complexity of star formation, and the limitations of numerical codes, this seems a more fruitful approach to take.

1.4 Evolutionary stages of star formation

A low-mass prestellar core evolves to form a young stellar object (YSO). YSOs are all at different evolutionary stages and so we divide their evolution into 4 classes, forming a sequence (Lada 1987; André et al. 1993). We note that this sequence is only well established for low-to-intermediate mass stars.

Class 0

This is the earliest stage of protostar formation (André et al. 1993). Here, the protostar, which has just formed inside the core, has a mass less than that of the envelope. Its spectral-energy distribution (SED) resembles a single temperature blackbody at ~ 15 - 30K. The SED peaks in the sub-mm, due to the dust grains in the infalling envelope absorbing the radiation and re-emitting it in the sub-mm (André et al. 1993). The protostar cannot be observed directly at this stage since it is deeply embedded in the core. However, we may see indirect evidence of its presence either through a radio continuum source, a collimated CO outflow, or an internal heating source. This is the main accretion phase, lasting for ~ 10^4yrs with a rate of accretion onto the central object of $\gtrsim 10^{-5}M_{\odot}yr^{-1}$. At the end of this stage, the protostar should have reached approximately half of its final mass.

Class I

Objects that are in the Class I stage are sometimes referred to as late or evolved protostars. Here, a disk has started to form, through which the material with high angular momentum can accrete onto the protostar. However, traces of the envelope can still be seen. Whilst the SED still peaks in the sub-mm, there is also an excess of IR emission. This is likely to be from the circumstellar disc being heated up by the central protostar. There is no optical emission from the central protostar due to it still being deeply embedded. The Class I stage lasts for a few 10^5yrs, now with a lower accretion rate ($\sim 10^{-6}M_\odot yr^{-1}$) compared to the Class 0 phase.

Class II

These objects are also known as classical T-Tauri stars. This phase corresponds to a stage where the majority of the envelope has been dissipated and there now exists a geometrically-thin optically-thick disc of mass $\sim 0.01M_\odot$. These discs have been directly observed using the Hubble Space Telescope. The central object is no longer embedded but is now optically revealed. Its SED peaks at IR wavelengths, attributed to the heating of the dust in the disk and re-emission in the IR. The accretion rate has now fallen to $\sim 10^{-8}M_\odot yr^{-1}$. The material accreting onto the stellar surface produces a strong Hα emission line and veiling of the UV absorption lines. This phase lasts for $\sim 1 - 4 \times 10^6$yrs.

Class III

Class III objects are also known as weak-line T-Tauri stars. Their SEDs show weak Hα emission and no major IR excess, which must signify that the disk has dissipated and there is little or no accretion occurring. After $\sim 10^7$yrs of this stage, the protostar evolves onto the main sequence.

1.5 Accretion Disks

Accretion discs form when circumstellar gas and dust attempt to fall onto the central protostar, but are prevented from doing so by centrifugal forces. The angular velocity of the material increases and therefore forces it to collapse down to form a circumstellar disc. The disc then evolves through angular momentum transport outwards and mass transport inwards onto the protostar, increasing its mass. This process of angular momentum transport is required to solve the problem of conservation of momentum in star formation. We know that molecular cloud cores possess angular momentum, which may be revealed as ordered rotation (velocity ~ 0.1 kms^{-1}) or as turbulence. However, this angular momentum cannot be conserved minutely and so must be removed or redistributed otherwise centrifugal forces will prevent collapse and hence star formation (Mestel & Spitzer 1956). The redistribution of angular momentum through the disk could be driven by gravitational torques, or by viscosity. Another possible process is magnetic braking. Here, angular momentum is transported to the outer regions via Alfvén waves. These waves are generated from the magnetic field lines which are twisted into a helical pattern from the rotation of the cloud.

Indirect observational evidence for the existence of discs can be found in the SEDs of the protostellar cores. Dust in the disc is heated by stellar irradiation, compression and viscous dissipation, which produces an IR excess in the SED. In the last few years discs have been directly observed. Many of these observations have been made by the Hubble Space Telescope, and by ground-based adaptive optics. Observations show that these discs span $10 - 1000$ AU with masses $0.001 - 0.1\,M_{\odot}$. As mentioned earlier, they are present from very early in the evolution of a collapsing core to the final stages such as in CTTs and WTTs.

Observations have shown that a small fraction of the accreted material is ejected in bipolar jets or outflows (e.g. Richer et al. 2000), which are perpendicular to the disk. These are thought to carry away the excess angular momentum of the infalling matter.

The jets extend to lengths of 10^{-2} to 1 pc and are highly collimated, reaching velocities of hundreds of kms^{-1}.

Density perturbations can grow in protostellar discs causing them to become gravitationally unstable. A measure of their stability against fragmentation is the Toomre stability parameter (Toomre 1964);

$$Q = \frac{c\kappa}{\pi G\Sigma}, \tag{1.6}$$

where c is the sound speed, κ is the epicyclic frequency, and Σ is the mass surface density within the disc. For a disc to remain stable against self gravity, Q must exceed 1.

If a disc becomes gravitationally unstable and fragments, it is possible for multiple systems to be formed. It has also been shown that discs can promote the formation of low-mass stars in binaries and also boost the number of triple and quadruple systems formed, via star-disc interactions (e.g McDonald & Clarke 1995).

1.6 Main Sequence stars and brown dwarfs

Once a star becomes sufficiently dense and hot enough to begin hydrogen burning, it enters the main sequence phase. Here the energy created from the thermonuclear reactions that convert hydrogen into helium provides enough pressure to stop further collapse of the core. Not all stars at this stage have the required density and mass and so they never reach the main sequence. These stars are called brown dwarfs. They are sometimes referred to as 'failed stars'. This is due to their masses being insufficient (approximately $< 0.08M_{\odot}$) for hydrogen burning to occur. Hence, they do not have a main sequence phase. Instead, they are dense enough to be supported by electron degeneracy pressure. Observations of brown dwarfs are extremely difficult to make since these objects are very faint, with luminosities $< 10^{-4}L_{\odot}$. A significant number of young brown dwarfs

have disks. Evidence of this is shown by the IR excess in their SEDs.

With improved sensitivity of telescopes, brown dwarfs are now routinely observed (e.g. Martín et al. 2001; Wilking et al. 2004; Luhman 2004). However, the mechanism behind their formation has not yet been confirmed. It is not known whether they form in the same way as more massive stars, or whether a different process is involved.

There currently exist many possible theories, all plausible but none yet confirmed. One theory is that brown dwarfs are formed by the ejection of low mass stellar embryos from their prestellar cores (Reipurth & Clarke 2001). This is a result of fragmentation producing multiple systems which then grow by competitive accretion. These systems then interact dynamically, ejecting the lowest mass object. This could explain the lack of brown dwarfs in close orbits around Sun-like main sequence stars (the Brown Dwarf Desert). This method seems quite possible since it only requires a protostar of $0.08M_{\odot}$ being in existence with two other protostars, which will almost inevitably result in the lowest mass object being ejected. However, we see evidence of brown dwarfs in multiple systems whereas this mechanism usually produces single brown dwarfs (Whitworth & Goodwin 2005). Also, during the ejection process it is unlikely that they will retain their disks.

Other theories of brown dwarf formation involve gravitational instabilities in circumstellar disks (Stamatellos et al. 2007b), opacity limited fragmentation in turbulent molecular clouds (Boyd & Whitworth 2005) or photo-evaporation of massive cores where a stable pre-existing core is overrun by a HII region (Whitworth & Zinnecker 2004).

1.7 Plan of thesis

In this thesis, we investigate star formation in molecular cloud cores, with the aim of understanding how the physical processes influence the mass distribution, kinematics and binary statistics of the resulting hydrogen-burning stars and brown dwarfs.

In Chapter 2, we discuss the algorithms and features of the numerical code that we use to model the prestellar cores. The code uses Smoothed Particle Hydrodynamics, and we describe the additional features we have added to our code to improve its speed and accuracy.

In Chapter 3, we test our numerical code by performing acoustic oscillations of an isentropic sphere. This test is designed to measure the numerical dissipation and numerical diffusion in a code. We show that it is an important test for codes used in simulating star formation.

In Chapter 4, we simulate the collapse and fragmentation of isolated, low-mass cores having different levels of turbulence. To treat the energy equation and associated radiative transport, we use a new technique developed by Stamatellos et al. (2007a). We discuss the effect this has on the resulting stars compared to those formed using a barotropic equation of state.

In Chapter 5, we perform simulations of the prestellar cores in the Ophiuchus Main Cloud. Each core has a different mass, a different initial density and a different initial level of turbulence. We discuss the effects these parameters have on the mass distribution, kinematics and binary statistics of the resulting stars.

In Chapter 6, we investigate how the metallicity of the gas effects the mass distribution and binary frequency of stars formed from a low-mass core.

In Chapter 7, we summarise the main conclusions drawn from this work and discuss

our future plans.

Chapter 2

Smoothed Particle Hydrodynamics

In this chapter, we review Smoothed Particle Hydrodynamics (SPH), the technique we employ to simulate astrophysical problems, in particular star formation. SPH is a particle method in which we represent a fluid by using particles, and follow their evolution under the influence of certain forces such as pressure or gravity. We discuss the hydrodynamical equations and how we incorporate these into the code. We also discuss modifications made to the code to improve its efficiency, such as an octal spatial-decomposition tree to calculate the gravitational acceleration of a particle, and modifications to improve the accuracy, such as artificial viscosity for shocked regions.

2.1 Self-Gravitating Compressible Flow

Numerical simulations play an increasingly important role in the study of star formation, and of other non-linear phenomena involving self-gravitating gas dynamics. These include the development of cosmological structure, galaxy formation, star formation and stellar collisions. To model such phenomena, we need to look at the equations of hydrodynamics.

In order to describe the evolution of a self-gravitating, viscous, compressible, non-

magnetic fluid, we must solve the continuity equation, Euler's momentum equation and the energy equation. By solving these we can determine the flow properties in terms of the velocity $\mathbf{v}$, pressure P, specific internal energy u and density ρ of each fluid element.

There are two possible forms for the equations; Eulerian and Lagrangian. In the Eulerian formulation, the properties of the fluid are functions of position and time. We define a fixed volume in space upon which the fluid moves. The time derivatives that are calculated in this formulation are therefore partial derivatives and give the rate of change of a quantity at a fixed position $\mathbf{r}$. The equations of continuity, momentum and energy take the following Eulerian forms:

- **Continuity equation**

$$\frac{\partial \rho}{\partial t} = -\nabla \cdot (\rho \mathbf{v}) \tag{2.1}$$

This describes the conservation of mass i.e. the rate of decrease in density in an infinitesimal volume of space at $\mathbf{r}$ equals the divergence of the flux of matter at that position.

- **Euler's momentum equation**

$$\frac{\partial \mathbf{v}}{\partial t} = -\mathbf{v} \cdot \nabla \mathbf{v} - \frac{\nabla P}{\rho} + \mathbf{a}_{\text{GRAV}} \tag{2.2}$$

Here the terms on the righthand side give the contributions to the rate of increase in velocity due to (i) advection of momentum into the volume, (ii) the acceleration due to the hydrodynamic pressure forces, and (iii) the gravitational acceleration.

- **Energy equation**

$$\frac{\partial u}{\partial t} = -\mathbf{v} \cdot \nabla \mathbf{u} - \frac{P \nabla \cdot \mathbf{v}}{\rho} + \mathcal{H}_{\text{RAD}} \tag{2.3}$$

The terms on the right hand side give the contributions to the rate of increase in internal energy in an infinitesimal volume of space at $\mathbf{r}$ due to (i) advection of internal energy into the volume, (ii) compressional heating, and (iii) radiative heating.

This is the formulation upon which most finite difference codes are based. The fluid

quantities are defined on a regular spatial grid.

In the Lagrangian formulation, the properties of the fluid are associated with a particular fluid element. Equations (2.1), (2.2) and (2.3) now take the Lagrangian forms:

• **Continuity equation**

$$\frac{d\rho}{dt} = -\rho\nabla \cdot \mathbf{v} \tag{2.4}$$

• **Euler's momentum equation**

$$\frac{d\mathbf{v}}{dt} = -\frac{\nabla P}{\rho} + \mathbf{a}_{\text{GRAV}} \tag{2.5}$$

• **Energy equation**

$$\frac{du}{dt} = -\frac{P\nabla \cdot \mathbf{v}}{\rho} + \mathcal{H}_{\text{RAD}} \,. \tag{2.6}$$

In both formulations we relate the pressure of a gas to its density ρ and temperature T via an equation of state. It is generally of the form $P = P(\rho, u)$. If the gas is isothermal, the equation of state is given by

$$P = a_\circ^2 \rho \tag{2.7}$$

where $a_\circ$ is the constant isothermal sound speed.

Grid based codes have certain advantages over Lagrangian codes, depending on the type of physics we wish to model. However, during the evolution of a star formation simulation, the local density may increase by many orders of magnitude and as a result there may be a need for very high spatial resolution in certain parts of the computational domain. Adaptive mesh refinement (AMR) has been developed to address this problem (Truelove et al. 1998). Here a high resolution grid is reconstructed at each new

timestep in order to calculate accurate spatial derivatives where they are needed. This can be computationally expensive, much more so than Lagrangian codes. Lagrangian codes automatically concentrate resolution in regions where matter is concentrated, and as these tend to be the regions where greater resolution is required, there is no need for complex refinement algorithms. In this way they resolve regions of high density without wasting computational effort on regions of low density. In addition, particle-based Lagrangian methods have no imposed geometrical constraints, and make much less use of imposed grids. They are therefore well suited to handling complex geometries. These are the two main reasons we choose to adopt a Lagrangian formulation.

2.2 The concept of SPH

Smoothed Particle Hydrodynamics (SPH) is a numerical technique introduced by Lucy (1977) and Gingold & Monaghan (1977). It is used to model complex, non-axisymmetric situations in astrophysics, for example star formation and also many problems in other areas of physics and industry, such as geophysics and engineering. SPH is a particle method in which the fluid is represented by discrete points (particles) whose motion, and therefore evolution, can be followed under the influence of forces representing pressure, gravity, viscosity and magnetic fields.

Each of the N SPH particles is defined by its own physical properties, such as position, mass and velocity. These properties are distributed or 'smoothed' over a finite volume, to represent a continuous fluid. We compute the physical variables at the position of particle i by summing contributions from all its neighbours j. A list of neighbours of each particle is found by searching through an octal tree, as explained in Section 2.7.1.

A smoothing kernel is used to interpolate over the neighbouring particles. The kernel is a weighting function and determines the strength and extent of a particle's

influence. The value of a continuum variable A at position $\mathbf{r}$ is given exactly by

$$A(\mathbf{r}) = \int A(\mathbf{r}')\delta(\mathbf{r} - \mathbf{r}')d^3\mathbf{r}' \tag{2.8}$$

where $\delta(\mathbf{r} - \mathbf{r}')$ is the Dirac delta function centred at $\mathbf{r}$. In order to smooth over the particles we replace the delta function by a finite interpolation kernel, $W(\mathbf{r} - \mathbf{r}', h)$. This kernel has a scale length h and a radius of interaction of $2h$. The chosen kernel function should satisfy two conditions. Firstly the kernel must tend to a delta function as the smoothing length tends to zero, i.e.

$$\lim_{h\to 0}[W(\mathbf{r} - \mathbf{r}', h)] = \delta(\mathbf{r} - \mathbf{r}'). \tag{2.9}$$

Secondly, the kernel must be normalised such that

$$\int W(\mathbf{r} - \mathbf{r}', h)d^3\mathbf{r}' = 1. \tag{2.10}$$

With the substitution of the kernel, the smoothed value of A at position $\mathbf{r}$ is therefore

$$\langle A(\mathbf{r})\rangle = \int_{-\infty}^{\infty} A(\mathbf{r}')W(\mathbf{r} - \mathbf{r}', h)d^3\mathbf{r}'. \tag{2.11}$$

In order to find the value of function A at the position of particle i, we approximate the integral interpolant (2.11) by a summation interpolant over the neighbouring particles, j,

$$A(\mathbf{r}_i) = \sum_j \frac{m_j}{\rho_j} A_j W(\mathbf{r}_i - \mathbf{r}_j, h), \tag{2.12}$$

where m_j is the mass of the particle, ρ_j is the density at $\mathbf{r}_j$, and A_j is the value of the parameter A of j. Here m_j/ρ_j replaces the volume element $d^3\mathbf{r}'$. The gradient of A can then be calculated by differentiating (2.12), so

$$\nabla A(\mathbf{r}_i) = \sum_j \frac{m_j}{\rho_j} A_j \nabla W(\mathbf{r}_i - \mathbf{r}_j, h). \tag{2.13}$$

2.3 Kernels

The first type of kernel used by Gingold & Monaghan (1977) was a Gaussian. Since then, many kernels have been tested, but the most extensively used to date is the cubic spline M_4 kernel developed by Monaghan & Lattanzio (1985), and this is used in our work. In 3-dimensions, the M_4 kernel is

$$M_4(|\mathbf{r}_i - \mathbf{r}_j|, h) = \frac{1}{\pi h^3} \begin{cases} 1 - \frac{3}{2}u^2 + \frac{3}{4}u^3, & \text{for } 0 \leq u \leq 1, \\ \frac{1}{4}(2-u)^3, & \text{for } 1 \leq u \leq 2, \\ 0, & \text{otherwise,} \end{cases} \tag{2.14}$$

where $u = |\mathbf{r}_i - \mathbf{r}_j|/h$ (Monaghan & Lattanzio 1985). The first derivative of this kernel is

$$M_4'(|\mathbf{r}_i - \mathbf{r}_j|, h) = -\frac{1}{\pi h^4} \begin{cases} 3u - \frac{9}{4}u^2, & \text{for } 0 \leq u \leq 1, \\ \frac{3}{4}(2-u)^2, & \text{for } 1 \leq u \leq 2, \\ 0, & \text{otherwise.} \end{cases} \tag{2.15}$$

This kernel has compact support, i.e. it is of finite extent. This is a realistic approach because physical quantities such as ρ and P are local and so need not be smoothed over the entire fluid in the computional domain. This is a great advantage computationally since it means smoothed variables only have contributions from a small number of close neighbouring particles. By using the M_4 kernel, particles that are more than $2h$ away from i do not interact and so are not considered, keeping the computational cost low. In contrast, the Gaussian kernel of Gingold & Monaghan (1977) extends over the entire spatial domain so that all particles in the simulation contribute to summations. If large numbers of particles are used, this is computationally very expensive.

2.4 SPH equations

With the use of SPH interpolation, the equations describing the evolution of a self-gravitating, compressible flow, as given in Section 2.1, can be rewritten as;

• Continuity equation

The summation interpolant (2.12) can be used to give an expression for the density ρ_i at $\mathbf{r}_i$,

$$\rho_i = \sum_{j=1}^{N} m_j W_{ij}, \tag{2.16}$$

where $W_{ij} \equiv W|(\mathbf{r}_i - \mathbf{r}_j, h|$. Using the time derivative of this expression (2.13), we can rewrite the continuity equation as

$$\frac{d\rho_i}{dt} = \sum_{j=1}^{N} m_j \mathbf{v}_{ij} \cdot \nabla_i W_{ij} \tag{2.17}$$

where $\mathbf{v}_{ij} \equiv \mathbf{v}_i - \mathbf{v}_j$.

• Momentum equation

We can symmetrise the pressure force between two particles by using the identity

$$\frac{\nabla P}{\rho} = \nabla\left(\frac{P}{\rho}\right) + \frac{P}{\rho^2}\nabla\rho\,. \tag{2.18}$$

Using this expression, the momentum equation then takes the form

$$\frac{d\mathbf{v}_i}{dt} = \left[-\sum_{j=1}^{N} m_j\left(\frac{P_i}{\rho_i^2} + \frac{P_j}{\rho_j^2}\right)\nabla_i W_{ij}\right] + \mathbf{a}_{\text{GRAV}}\,. \tag{2.19}$$

Therefore the pressure force between two particles is symmetric, hence linear and angular momentum are conserved.

• **Energy equation**

We can symmetrise the energy equation using the identity

$$\frac{P}{\rho}\nabla\cdot\mathbf{v} = \nabla\cdot\left(\frac{P}{\rho}\mathbf{v}\right) - \mathbf{v}\cdot\nabla\left(\frac{P}{\rho}\right). \tag{2.20}$$

The rate of change of the specific internal energy of an SPH particle becomes

$$\frac{du_i}{dt} = -\frac{1}{2}\sum_{j=1}^{N} m_j\left(\frac{P_i}{\rho_i^2} + \frac{P_j}{\rho_j^2}\right)(\mathbf{v}_i - \mathbf{v}_j)\cdot\nabla_i W_{ij} + \mathcal{H}_{\text{RAD}}\,. \tag{2.21}$$

2.5 Smoothing Lengths

The smoothing length essentially determines the level of resolution in SPH. The choice of h is extremely important, since we must ensure we are resolving on a scale comparable with or less than the scale of the physical processes we are interested in. Failing to resolve on these scales means we may smooth over some important features.

When SPH was first introduced, smoothing lengths were constant in time and uniform in space (Gingold & Monaghan 1977). However it has since been demonstrated that if each particle has its own h which is allowed to vary in time, the spatial resolution is substantially improved (Hernquist & Katz 1989). By having a smoothing length that varies in time and space, the number of neighbours of each particle can remain roughly constant. This means that high density regions can be better resolved since a smaller h is required in order to meet this condition.

The smoothing length of a particle is adjusted so that its neighbour list contains N_{NEIB} other particles. The choice of N_{NEIB} is a compromise between good sampling and good resolution. If N_{NEIB} is increased, the sampling is improved and hydrodynamic variables are smoother, but resolution is degraded. Conversely if N_{NEIB} is reduced, sampling is degraded and hydrodynamic variables are noisier, but resolution is improved. Having

a larger $N_{\rm NEIB}$ also increases the computational time, so it is important to strike the right balance. Experience suggests that $N_{\rm NEIB} \approx 50$ is a good compromise. Many SPH simulations in the literature allow $N_{\rm NEIB}$ to fluctuate within some tolerance $\Delta N_{\rm NEIB}$. In Chapter 4, we show that if the tolerance is set to zero, there is a marked reduction in the rates of numerical dissipation and diffusion .

Some SPH codes (e.g. Price & Monaghan 2004) do not specify the number of neighbours, but instead, for each particle, iterate around a loop,

$$h_i = h_0 \left[\frac{m_i}{\rho_i}\right]^{1/3} \tag{2.22}$$

$$\rho_i = \sum_j \left\{\frac{m_j}{h_i^3} W\left(\frac{|\mathbf{r}_j - \mathbf{r}_i|}{h_i}\right)\right\} \tag{2.23}$$

until fractional changes in ρ_i drop below a user-defined tolerance, ϵ. Here h_0 is a constant of order unity, and the summation is over all neighbours j for which $|\mathbf{r}_j - \mathbf{r}_i| < 2\,h_i$ (i.e. all particles within the smoothing kernel of particle i). Provided ϵ is sufficiently small, this is statistically equivalent to setting $N_{\rm NEIB} = 32\pi h_0^3/3$ and $\Delta N_{\rm NEIB} = 0$.

2.6 Artificial Viscosity

Artificial viscosity is introduced in order to treat shocks correctly. When shocks are simulated in SPH, small oscillations can occur behind the shock front. This is a result of the discrete nature of the particles, and so the oscillations are unphysical. Another problem that arises here is colliding streams of particles travelling at high Mach numbers can penetrate each other. In these situations, an extra pressure term is added to the momentum equation which produces a repulsive force between particles that are close and rapidly approaching each other. This effectively slows the colliding streams down and, in the case of shocks, allows the shocked region to be approximately resolved.

The standard form of artificial viscosity is described by Monaghan (1992). With

artificial viscosity, the equation of motion for particle i is given by

$$\frac{d\mathbf{v}_i}{dt} = -\sum_j m_j\left(\frac{P_i}{\rho_i^2} + \frac{P_j}{\rho_j^2} + \Pi_{ij}\right)\nabla_i W_{ij} + \mathbf{a}_{\text{GRAV}}\,, \tag{2.24}$$

where Π_{ij} is

$$\Pi_{ij} = \begin{cases} \frac{-\alpha\bar{c}_{ij}\mu_{ij}+\beta\mu_{ij}^2}{\bar{\rho}_{ij}} & (\mathbf{v}_{ij}.\mathbf{r}_{ij}) < 0; \\ 0 & (\mathbf{v}_{ij}.\mathbf{r}_{ij}) > 0; \end{cases} \tag{2.25}$$

and

$$\mu_{ij} = \frac{(\mathbf{v}_{ij}.\mathbf{r}_{ij})\bar{h}_{ij}}{|\mathbf{r}_{ij}|^2 + 0.01\bar{h}_{ij}^2} \tag{2.26}$$

(Monaghan 1992). Here, $\mathbf{r}_{ij} \equiv \mathbf{r}_i - \mathbf{r}_j$, $\mathbf{v}_{ij} \equiv \mathbf{v}_i - \mathbf{v}_j$, $\bar{h}_{ij} \equiv (h_i + h_j)/2$, $\bar{\rho}_{ij} \equiv (\rho_i + \rho_j)/2$ and $\bar{c}_{ij} \equiv (\bar{c}_i + \bar{c}_j)/2$, where c_i and c_j are the sound speeds for particles i and j respectively. Similarly, the energy equation becomes

$$\frac{du_i}{dt} = -\frac{1}{2}\sum_{j=1}^{N} m_j\left(\frac{P_i}{\rho_i^2} + \frac{P_j}{\rho_j^2} + \Pi_{ij}\right)(\mathbf{v}_i - \mathbf{v}_j)\cdot\nabla_i W_{ij} + \mathcal{H}_{\text{RAD}}\,. \tag{2.27}$$

We stress that this extra viscosity is only incorporated when particles are approaching i.e. $(\mathbf{v}_{ij}.\mathbf{r}_{ij}) < 0$, as required in shocks. α and β are user defined parameters which control the strength of the viscosity. Good results are obtained with $\alpha = 1.0$ and $\beta = 2.0$ (Monaghan 1992). The α term is a bulk velocity, and is dominant for small velocity differences e.g. subsonic velocity oscillations. The β term is a second order, von Neumann-Richtmyer-type viscosity, and is dominant when there are large velocity gradients e.g. high Mach number shocks. Standard artificial viscosity is symmetric, so that two approaching particles, i and j, exert equal and opposite forces on each other, and therefore linear momentum and angular momentum are conserved. This means we can capture the basic jump conditions across a shock with acceptable accuracy.

However, this prescription is applied to the whole fluid, even though it is only required where and when shocks occur. This can cause problems, because in regions away from shocks where there are shear flows, it can lead to angular momentum being

transported unphysically. To limit the level of shear viscosity produced, various switches and forms of artificial viscosity have been devised, such as the Balsara switch and time-dependent viscosity.

2.6.1 Time-dependent viscosity

This approach to reducing the amount of shear viscosity was proposed by Morris & Monaghan (1997). In standard artificial viscosity, α, one of the parameters controlling the strength of viscosity, is set at a fixed value for all particles in the simulation. In time-dependent viscosity, each particle is given its own viscosity parameter α_i. α_i is then evolved according to the equation

$$\frac{d\alpha_i}{dt} = -\frac{\alpha_i - \alpha^\star}{\tau} + S_i . \tag{2.28}$$

$\alpha^\star$ is the minimum value that α_i decays to in the absence of shocks, over a timescale τ. Morris & Monaghan (1997) adopt $\alpha^\star = 0.1$, because it allows the effect of viscosity to be reduced by an order of magnitude for particles away from the shock, but still treats the particles in the shocked region with the required bulk velocity. S_i is a source term, which Rosswog et al. (2000) take as

$$S_i = \max(-\nabla \cdot \mathbf{v}, 0)(2.0 - \alpha) . \tag{2.29}$$

S_i is chosen such that the viscosity grows as the particle approaches a shock front. The timescale on which α_i decays is chosen to be

$$\tau_i = \frac{h_i}{c_i C} . \tag{2.30}$$

c_i is the local sound speed in the fluid and C is a dimensionless parameter with value $0.1 \leq C \leq 0.2$. Morris and Monaghan (1997) recommend $C = 0.1$ to obtain good results. β_i is then set to $2\alpha_i$.

2.6.2 Balsara switch

Rather than having the level of viscosity decay for particles away from shocked regions as in time-dependent viscosity, the Balsara switch (Balsara 1995) is designed to simply turn on viscosity for particles in shocked regions only. Here, a dimensionless factor f is defined for a particle i and its neighbour j. It describes the local flow for each particle and is given by

$$f_i = \frac{|\nabla \cdot \mathbf{v}|_i}{|\nabla \cdot \mathbf{v}|_i + |\nabla \times \mathbf{v}|_i + 0.0001 c_i/h_i}. \tag{2.31}$$

For each particle-particle interaction, Π_{ij} is multiplied by $f_{ij} = (f_i + f_j)/2$. The factor approaches unity in regions of strong compression i.e. shocked regions, since here $|\nabla \cdot \mathbf{v}| \gtrsim |\nabla \times \mathbf{v}|$. In regions of pure shear flow, the factor approaches zero, since $|\nabla \cdot \mathbf{v}| \ll |\nabla \times \mathbf{v}|$.

2.7 Gravity

In each form of the momentum equation given in this chapter, we have included a term to describe the gravitational acceleration of i due to all of the other particles. For a system of point masses, this is given by

$$\mathbf{a}_{\mathrm{GRAV},i} = -\sum_{j=1\, j\neq i}^{N} \frac{m_j \mathbf{r}_{ij}}{|\,\mathbf{r}_{ij}\,|^3}. \tag{2.32}$$

Here we are using units such that $G = 1$. Generally SPH codes use kernel-softened gravity to calculate the gravitational acceleration when the separation of particles is less than $2h_{ij}$; this is to avoid violent gravitational scatterings. For all other situations, i.e. when the separation is greater than $2h_{ij}$, tree gravity is used.

2.7.1 Tree Code Gravity

An accurate estimate of the gravitational acceleration can be made much more efficiently using a tree to organise the particles into groups. We incorporate the Barnes-Hut octal tree (Barnes & Hut 1986) in our star formation code. An alternative is to perform a direct summation over all particles, but this is extremely computionally expensive. For $\mathcal{N}$ particles, a direct summation requires $O(\mathcal{N}^2)$ calculations, whereas using a tree we can reduce this to $O(\mathcal{N}log\mathcal{N})$.

The tree is constructed as follows. Firstly, we set the entire computational domain as the rootcell of the hierarchy. This rootcell is then subdivided into 2^n subcells (where n is the number of dimensions) and these in turn are repeatedly subdivided. This subdivision continues until a cell contains a single particle or no particle at all. The rootcell is at the top level of this hierarchy and its 2^n subcells are the next level down. Any cell that does not directly contain particles, but is subdivided, stores the centre of mass due to all its lower level subcells. This means that the rootcell contains the centre of mass of the whole computational domain. Each cell is defined by its total mass, centre of mass and pointers to its subcells. The structure of a 2-dimensional tree constructed for a simple distribution is shown in Fig. 2.1.

To calculate the gravitational acceleration on a particle, we must decide whether we can treat the particles in a cell as a group. In order to make this decision, the following criterion is applied to each cell in turn, starting at the top of the tree,

$$\frac{S}{d} < \theta. \tag{2.33}$$

d is the distance from i to the cell in question, S is the linear size of the cell, and θ is the maximum opening angle. If this condition is obeyed, the particles in the cell and all its subcells are treated as a cluster. If not, the cell is opened and the subcells are examined. If the cell contains a single particle then the gravitational acceleration is found by direct calculation, i.e. a particle-particle interaction is calculated. Accurate estimation of the

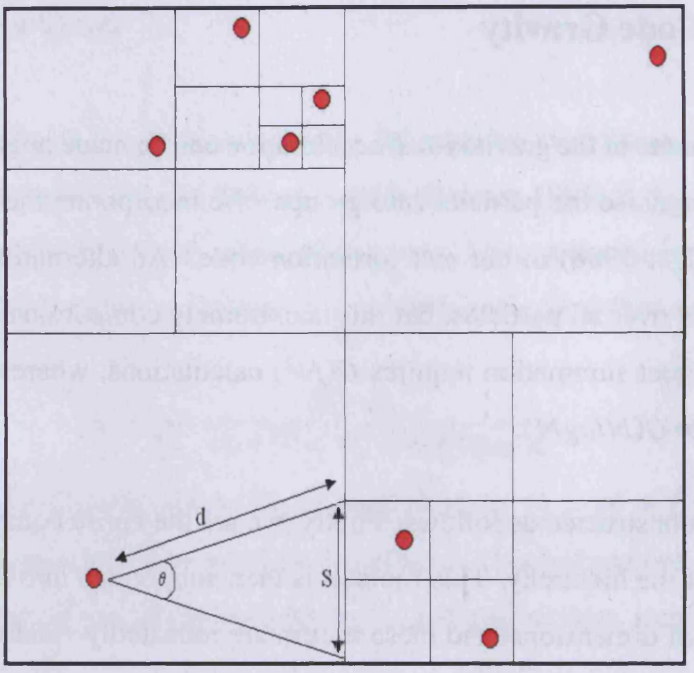

Figure 2.1: The structure of a 2-dimensional tree constructed for a simple distribution. Depending on the value of θ, we can determine whether to calculate the gravitational accelerations directly or approximate the particles as a cluster.

gravitational acceleration requires $\theta < 0.577$ (Salmon, Warren & Winckelmans 1994). We use $\theta = 0.5$.

In addition to calculating the gravitational acceleration in an efficient manner, we can use a tree to construct lists of the neighbours of each particle, which are required for SPH summations.

2.7.2 Kernel Softened Gravity

From the calculation for the gravitational acceleration in Equation (2.32), due to the $1/r^2$ term, particles at small separations can experience large forces and hence violent accelerations. To avoid this we soften these interactions by smoothing the particle, no longer treating it as a point mass. In this scenario the particles are taken to be spherically symmetric with finite extent of $2h$. When the inter-particle separation is less than $2h_{ij}$, i.e.

the particles overlap, we use Gauss' gravitational theorem to calculate the gravitational acceleration.

In the vicinity of particle i, the mass interior to radius sh_i is $m(s) = m_i W^*(s)$ where

$$W^*(s) = \int_0^s 4\pi s^2 W(s) ds. \tag{2.34}$$

In accordance with Gauss's gravitational theorem, we neglect the mass of particle i outside of sh_i. Hence, the contribution to the gravitational acceleration of particle j due to particle i is

$$\mathbf{a}_{\text{GRAV},j} = -m_i W^*\left(\frac{|\mathbf{r}_{ij}|}{\bar{h}_{ij}}\right)\frac{\mathbf{r}_{ij}}{|\mathbf{r}_{ij}|^3}. \tag{2.35}$$

The gravitational potential at distance r_{ij} from particle i is then

$$\Phi_{ij} = \int_\infty^{r_{ij}} \frac{m_i}{r^2} W^*\left(\frac{r}{\bar{h}_{ij}}\right) dr. \tag{2.36}$$

Integrating by parts and multiplying by m_i, the mutual potential energy of particles i and j is given by

$$m_i \Phi_{ij} = -\frac{m_i m_j}{r_{ij}}[W^*(s) + W^{**}(s)] \tag{2.37}$$

where

$$W^{**}(s) = s\int_s^\infty 4\pi s' W(s') ds'. \tag{2.38}$$

For the M_4 kernel, W^* and W^{**} are

$$W^* = \frac{1}{30}\begin{cases} 40s^3 - 36s^5 + 15s^6, & \text{for } 0 \le s \le 1, \\ 80s^3 - 90s^4 + 36s^5 - 5s^6 - 2, & \text{for } 1 \le s \le 2, \\ 30, & \text{for } s \ge 2; \end{cases} \tag{2.39}$$

$$W^{\star\star} = \frac{s}{10}\begin{cases} 14 - 20s^2 + 15s^4 - 6s^5, & \text{for } 0 \le s \le 1, \\ (2s+1)(2-s)^4, & \text{for } 1 \le s \le 2, \\ 0, & \text{for } s \ge 2. \end{cases} \tag{2.40}$$

2.8 Integration Scheme

In order to update the positions, velocities and accelerations of the SPH particles with time, we use a second-order Runge-Kutta integration scheme. To advance a particle i from the n^{th} to the $(n+1)^{th}$ step, separated by time Δt, we need the current acceleration $\mathbf{a}_i^n$. This is found from Equation (2.19) which we write formally as

$$\mathbf{a}_i^n = f(\mathbf{r}_i^n, \mathbf{v}_i^n)\,. \tag{2.41}$$

The positions and velocities at the half timestep are then

$$\begin{aligned} \mathbf{r}_i^{n+1/2} &= \mathbf{r}_i^n + \mathbf{v}_i^n \Delta t/2, \\ \mathbf{v}_i^{n+1/2} &= \mathbf{v}_i^n + \mathbf{a}_i^n \Delta t/2. \end{aligned} \tag{2.42}$$

We then use these to calculate the acceleration at the half timestep

$$\mathbf{a}_i^{n+1/2} = f(\mathbf{r}_i^{n+1/2}, \mathbf{v}_i^{n+1/2}). \tag{2.43}$$

This then gives the new positions, velocities and accelerations

$$\begin{aligned} \mathbf{r}_i^{n+1} &= \mathbf{r}_i^n + \mathbf{v}_i^{n+1/2} \Delta t, \\ \mathbf{v}_i^{n+1} &= \mathbf{v}_i^n + \mathbf{a}_i^{n+1/2} \Delta t, \\ \mathbf{a}_i^{n+1} &= f(\mathbf{r}_i^{n+1}, \mathbf{v}_i^{n+1}). \end{aligned} \tag{2.44}$$

The choice of timestep Δt is of particular importance to avoid non-physical effects. We choose the minimum of each timescale to prevent the timestep being so long that it

evolves a particle for a time longer than that appropriate for the local conditions.

For each particle i, the maximum timestep Δt_i is

$$\Delta t_i = \gamma MIN\left[\frac{h_i}{|\mathbf{v}_i|}, \left(\frac{h_i}{|\mathbf{a}_i|}\right)^{1/2}, \frac{h_i}{\sigma_i}\right]. \tag{2.45}$$

Analysing Equation (2.45), we see it is dependent on various factors. The first two terms inside the brackets, $(h_i/|\mathbf{v}_i|)$ and $(h_i/|\mathbf{a}_i|)^{1/2}$, ensure that the change in position is small. The final term (h_i/σ_i) ensures that the courant condition is obeyed, i.e. no disturbance propagates faster than the local effective signal propagation speed,

$$\sigma_i = c_i + 1.2(\alpha c_i + \beta MAX[\mu_{ij}]). \tag{2.46}$$

α and β are the same viscosity parameters described in Section (2.6). γ is the Courant number and is usually set at 0.3.

2.9 Multiple Particle Timesteps

Multiple particle timesteps (MPT) is a scheme whereby each particle is assigned an individual timestep which can vary from step to step according to its needs (e.g. Bhattal 1996). This method is beneficial in simulations where both rapidly evolving regions (requiring short timesteps) and slowly evolving regions (not requiring such short timesteps) coexist. This means that particles are only evolved when necessary and so computation time is decreased.

MPT creates a hierarchy of timestep bins each containing particles whose timesteps are twice that of those in the next lower bin. To keep the system synchronised at regular intervals, particles are only allowed to move through these time bins and not with arbitrary sized timesteps. The maximum timestep is Δt_{max}, and each discrete timestep used by particles in different bins is calculated as a fraction of this maximum timestep.

Therefore the timesteps can have the values

$$\Delta t_{max},\ \Delta t_{max}/2,\ \Delta t_{max}/4,\ \Delta t_{max}/8,\ ...,\ \Delta t_{max}/2^{N_{bins}-1}, \tag{2.47}$$

where N_{bins} is the total number of available time bins.

At any time in the simulation $\Delta t_{max} = \Delta t_{min} 2^{N_{min}-1}$ and so we can express the current position along the largest timestep as $s\Delta t_{min}$ where s is the step position of value $s = 0, 1, 2, 3; ..., 2^{N_{min}-1}$. At $s = 0$, particles are in-synch since this is at the start of the maximum timestep.

The maximum timestep length Δt_i for a given particle i is initially calculated from Equation (2.45). The particle is then put into the next smaller time bin n with $\Delta t = \Delta t_{max}/2^n$, where n is given by

$$n = INT\left(\frac{ln(\Delta t_{max}/\Delta t_i)}{ln2}\right) + 1. \tag{2.48}$$

It is required that all particles are synchronised at the end of Δt_{max}. In order to ensure this, a timestep may only be used if the time from the beginning of the Δt_{max} period is a multiple of the time this bin represents. If this is not the case, we use the next descending acceptable time bin.

For example, if $N_{\min} = 5$, this gives $\Delta t_{max} = 16\Delta t_{min}$. If the timestep we are checking is $\Delta t = \Delta t_{max}/4$ ($n = 2$), we can only use it if $s = 0, 4, 8, 12$. Otherwise, we assign it the timestep $\Delta t = \Delta t_{max}/8$ ($n = 3$) if $s = 2, 6, 10, 14$. If s is odd, we assign it the lowest available timestep (here, $n = 4$). This is graphically represented in Fig. 2.2.

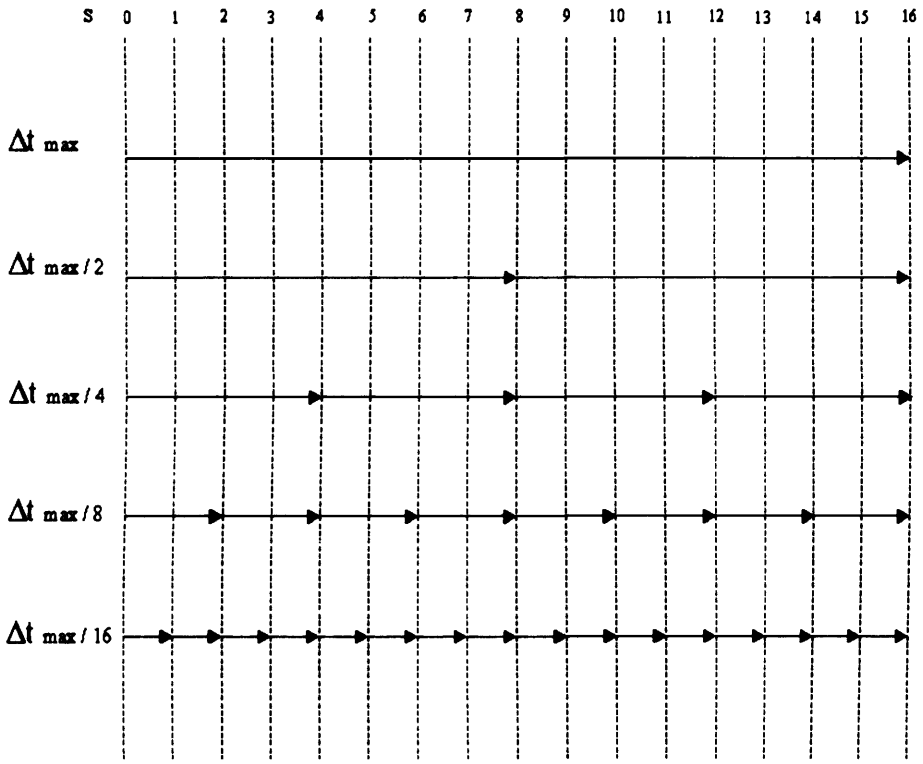

Figure 2.2: Graphical representation of MPT for when $n = 5$. Arrows indicate the steps that are allowed. By enforcing this, all particles will remain synchronised at the end of Δt_{max}.

2.10 Sink particles

In simulations of the collapse and fragmentation of a molecular cloud, the gas in the cloud reaches very high densities. The particles that represent these regions become so tightly packed that their smoothing lengths become very small. At this stage, the timestep required to follow their evolution becomes increasingly small, according to Equation (2.45). This is not ideal, because eventually all the computational resources are being used to follow the first protostellar condensation that forms. The simulation grinds to a halt, preventing us from following the formation of any further stars, or determining what their properties might have been. A solution to the problem has been proposed by Bate et al. (1995). They introduce the concept of replacing high density fragments with non-gaseous accreting particles, referred to as 'sink particles'.

If we are not interested in the internal structure of a dense region, it can be replaced by a sink particle only if it satisfies all of the following criteria:

- The density of one of the SPH particles i exceeds a particular threshold, $\rho_{\rm SINK}$. Typically we set $\rho_{\rm SINK} = 10^{-11}\,{\rm g\,cm^{-3}}$, though it must be ensured $\rho_{\rm SINK}$ is selected according to the resolution requirement of the simulation, to prevent spurious sink formation. Bate et al. (1995) suggest $\rho_{\rm SINK}$ should be 10^5 times the initial cloud density. An alternative approach for determining $\rho_{\rm SINK}$ involves using the Jeans criterion (Jeans 1928). In SPH the mass resolution of a code is $M_{\rm MIN} = N_{\rm NEIB} M_{\rm TOT}/N_{\rm TOT}$, where $M_{\rm TOT}$ is the total mass in the computational domain. $M_{\rm MIN}$ is the minimum mass required to resolve any features and $N_{\rm TOT}$ is the total number of SPH particles. The Jeans condition requires the minimum resolvable mass to be smaller than the Jeans mass, $M_{\rm JEANS}$, where

$$M_{\rm JEANS} = \left(\frac{375}{4\pi}\right)^{1/3} \frac{a_o^3}{G^{3/2}\rho^{1/2}}. \qquad (2.49)$$

Failure to do this means that gravitational instability can not be resolved properly

(Bate & Burkert 1997). This can lead to clouds fragmenting when they should be Jeans stable. However, with the kernel that we use it can be shown (Whitworth 1998; Hubber et al. 2006) that this does not lead to artificial fragmentation. Rearranging Equation (2.49), the highest resolvable density $\rho_{\rm JEANS}$ is given as

$$\rho_{\rm JEANS} = \left(\frac{375}{4\pi}\right)^{2/3} \frac{a_o^3}{G^3 N_{\rm NEIB}^2 M_{\rm TOT}^2} . \tag{2.50}$$

$\rho_{\rm SINK}$ must be smaller than $\rho_{\rm JEANS}$, in order for the condition to be satisfied.

- Particle i has negative velocity divergence.
- Particle i and its neighbours have net negative energy i.e. are bound.

By fulfilling these criteria, we can be sure that the region in question would continue to collapse under gravity to form a single star or a close multiple system, had it not been replaced by a sink particle.

When a sink is formed, it incorporates all the neighbours of particle i within a distance $R_{\rm SINK}$. Typically, we set $R_{\rm SINK} \sim 5$ AU, depending on the resolution requirements near the sink. Any particle which subseqently passes within $R_{\rm SINK}$ and is bound to that sink, is accreted. The mass, linear monentum and angular momentum of the accreted particle is added to that of the sink. Removing particles reduces the number of force calculations at each timestep, and hence speeds up the simulation. Therefore, incorporating sink particles enables the evolution of the cloud and resulting protostars to be followed. This is particularly important since observations of main sequence stars show that most stars are in binary or multiple systems (Duquennoy & Mayor 1991). We must therefore aim to explain their formation, and using sink particles is a way in which to do this.

2.11 Summary

In this chapter we have described the concept of Smoothed Particle Hydrodynamics, the technique we use to simulate star formation. We have discussed the features of a typical SPH code, including the integration scheme, multiple-particle timesteps and artificial viscosity. In our work we use the Cardiff star formation code DRAGON (Goodwin et al. 2004a). It is a standard SPH code, has all the features described in this chapter, and has been extensively tested and optimised. The following chapters report the results of simulations of certain star-forming scenarios performed using DRAGON.

Chapter 3

Acoustic oscillations of an isentropic monatomic gas sphere

In this chapter, we investigate the levels of numerical dissipation and diffusion in our SPH code. To do this, we simulate acoustic oscillations of a self-gravitating isentropic monatomic gas sphere. This test was originally performed by Lucy (1977), and is a highly relevant test for star formation codes. This is because pressure waves generated by the switch from approximate isothermality to approximate adiabacity play a crucial role in the fragmentation of collapsing cores. We find that, if the smoothing lengths in an SPH code are adjusted so as to keep the number of neighbours in the range $N_{\rm NEIB} \pm \Delta N_{\rm NEIB}$, $\Delta N_{\rm NEIB}$ *should be set to zero, to reduce the level of numerical dissipation and diffusion.*

3.1 Introduction

It is important to test numerical codes using known analytic or semi-analytic solutions. Such tests play an integral role in verifying that the code can model the same physical phenomena that occur during star formation, such as gravitational fragmentation. They also provide a good way of investigating the validity of different numerical modelling

techniques. It is well known that an adaptive mesh refinement finite difference code is in general more expensive computationally that an SPH code. However, ultimately neither method is useful, unless it can be shown that the results are converged and are not compromised by numerical artefact.

We propose such a test here, and in this chapter we apply it to our SPH code DRAGON. This test involves acoustic oscillations of a self-gravitating, isentropic, monatomic gas sphere in the fundamental radial mode. This test was originally performed by Lucy (1977) in his seminal paper introducing SPH, and therefore we shall refer to it as the Lucy test. It has been performed subsequently (e.g. Steinmetz & Müller 1993; Nelson & Papaloizou 1994), but infrequently. It is an appropriate test because it measures (i) the level of dissipation associated with artificial viscosity, in the absence of shocks; (ii) the extent to which transients, due to the discrete nature of particles (or cells), remove energy from genuine modes and transfer it to other spurious modes (i.e. numerical diffusion); (iii) the ability of the code to model acoustic oscillations, and in particular adiabatic bounces; and (iv) the ability of the code to deal with free (or nearly free) boundaries.

Point (iii) is particularly important because it seems that collapsing prestellar cores are most prone to fragment at the stage when the gas switches from being approximately isothermal to being approximately adiabatic (e.g. Boss et al. 2000). Fragmentation at this juncture is presumably due to interactions between the complex system of pressure waves which is generated by adiabatic bounces in a converging but disordered inflow, and it is therefore essential that spurious waves are not being generated. In this context it is worth noting that the isentropic assumption is not strictly the same as adiabaticity, and is made here for analytic convenience rather than realism. In simulations where shocks develop, artificial viscosity must be incorporated, in which case, *either* the resulting energy dissipation must be included in the energy equation, *or* – if the thermal timescale is sufficiently short, and the main concern is not with the detailed structure of the shock front – a barotropic equation of state may be invoked. There are no shocks in the present simulation, and therefore the rate of energy dissipation due to artificial viscosity is low,

but not negligible. The isentropic assumption then simply implies that the small amount of energy dissipated by artificial viscosity is replenished from the background radiation field.

It is also appropriate to point out that, although the gas in prestellar cores is largely molecular, it behaves as a monatomic gas (i.e. the effective adiabatic exponent $\gamma = 5/3$) until the temperature rises above $\sim$ 100 K. At lower temperatures the rotational degrees of freedom are not significantly excited, since para-H_2 has its first excited level ($J = 2$) at $k_B(512\,\mathrm{K})$, and ortho-H_2 has its first excited level ($J = 3$) at $k_B(854\,\mathrm{K})$ (e.g. Black & Bodenheimer 1975). Neglect of this fact can lead to artificially enhanced fragmentation of collapsing prestellar cores, since with $\gamma = 5/3$ the Jeans mass increases quite rapidly with increasing density in the adiabatic regime ($M_{\mathrm{JEANS}} \propto \rho^{1/2}$), whereas with $\gamma = 7/5$ it increases much more slowly ($M_{\mathrm{JEANS}} \propto \rho^{1/10}$).

3.2 Initial Conditions

The gas sphere modelled in these simulations is isentropic and monatomic. An isentropic gas has the equation of state

$$P = K\rho^{\gamma} \equiv K\rho^{1+\frac{1}{n}} \tag{3.1}$$

where K, γ and n are constants; $\ln[K]$ is the specific entropy and γ is the adiabatic exponent. For a monatomic gas $\gamma = 5/3$ and therefore $n = 3/2$. To set up a polytrope of this type, we must first visit the Lane-Emden equation and its functions.

3.2.1 Lane-Emden Equation

If a spherically symmetric self-gravitating polytrope is to be in hydrostatic balance we require

$$\frac{1}{\rho(r)}\frac{dP(r)}{dr} = g(r) = -\frac{GM(r)}{r^2}, \tag{3.2}$$

where r is defined as the radial distance from the centre, $\rho(r)$ is the density at r and $M(r)$ is the mass interior to r. This can be written as

$$M(r) = -\frac{r^2}{G\rho(r)}\frac{dP(r)}{dr}, \tag{3.3}$$

which differentiates to

$$\frac{dM(r)}{dr} = -\frac{1}{G}\frac{d}{dr}\left(\frac{r^2}{\rho(r)}\frac{dP(r)}{dr}\right). \tag{3.4}$$

Applying conservation of mass gives

$$M(r) = \int_{r'=0}^{r'=r} \rho(r')4\pi r'^2 dr' \tag{3.5}$$

and hence

$$\frac{dM(r)}{dr} = \rho(r)4\pi r^2. \tag{3.6}$$

By equating (3.4) with (3.6) we obtain

$$\frac{d}{dr}\left(\frac{r^2}{\rho(r)}\frac{dP(r)}{dr}\right) + 4\pi G r^2 \rho(r) = 0\,. \tag{3.7}$$

Substituting (3.1) in (3.7) gives

$$\frac{d}{dr}\left(r^2\rho^{(1/n-1)}(r)\frac{d\rho(r)}{dr}\right) + \frac{4\pi G r^2 \rho(r) n}{K(1+n)} = 0. \tag{3.8}$$

We introduce the dimensionless variables ξ and θ_n, defined as

$$\xi = \frac{r}{R_0}, \tag{3.9}$$

and

$$\theta_n(\xi) = \left(\frac{\rho(r = \xi R_0)}{\rho_c}\right)^{1/n}, \tag{3.10}$$

where ρ_c is the central density and R_0 is a scale length, given by

$$R_0 = \left(\frac{K(n+1)}{4\pi G}\rho_c^{(1/n-1)}\right)^{1/2}. \tag{3.11}$$

With substitution of these dimensionless variables, (3.8) reduces to the form

$$\frac{1}{\xi^2}\frac{d}{d\xi}\left(\xi^2\frac{d\theta_n}{d\xi}(\xi)\right) + (\theta_n(\xi))^n = 0. \tag{3.12}$$

Equation (3.12) is the Lane Emden (LE) equation.

3.2.2 Lane-Emden Functions

In order to solve the LE equation, we must find solutions which satisfy the boundary conditions, which are as follows.

Firstly, from the definition of the dimensionless variable θ in (3.10), it follows that

$$\rho(0) = \rho_c[\theta_n(\xi = 0)]^n = \rho_c\,. \tag{3.13}$$

Therefore

$$\theta_n(0) = 1. \tag{3.14}$$

The second boundary condition can be deduced from realising that there is no gravitational acceleration at the centre due to there being no central point mass. Therefore,

the pressure gradient must be zero at the centre.

$$\frac{dP}{dr}(r=0) = K\left(1+\frac{1}{n}\right)\rho^{1/n}(r=0)\frac{d\rho}{dr}(r=0) \tag{3.15}$$

$$= K\frac{(n+1)}{R_0}\rho_c{}^{(1+1/n)}[\theta_n(\xi=0)]\frac{d\theta_n}{d\xi}(\xi=0) \tag{3.16}$$

$$= 0. \tag{3.17}$$

Therefore,

$$\frac{d\theta_n}{d\xi}(0) = 0. \tag{3.18}$$

There exist three analytical LE functions corresponding to $n = 0$, 1 and 5. However, the polytrope to be examined is one in which $n = 3/2$, and so the LE function for this case can only be found by numerical integration of the LE equation.

In order to divide this second-order equation into two first-order equations, we define the dimensionless variable

$$\phi = -\xi^2\frac{d\theta}{d\xi}. \tag{3.19}$$

Hence, by differentiating we obtain

$$\frac{d\phi}{d\xi} = \xi^2\theta^n, \tag{3.20}$$

which has the boundary condition

$$\phi(\xi=0) = 0. \tag{3.21}$$

Also, by rearranging (3.19), we obtain

$$\frac{d\theta}{d\xi} = -\frac{\phi}{\xi^2}, \tag{3.22}$$

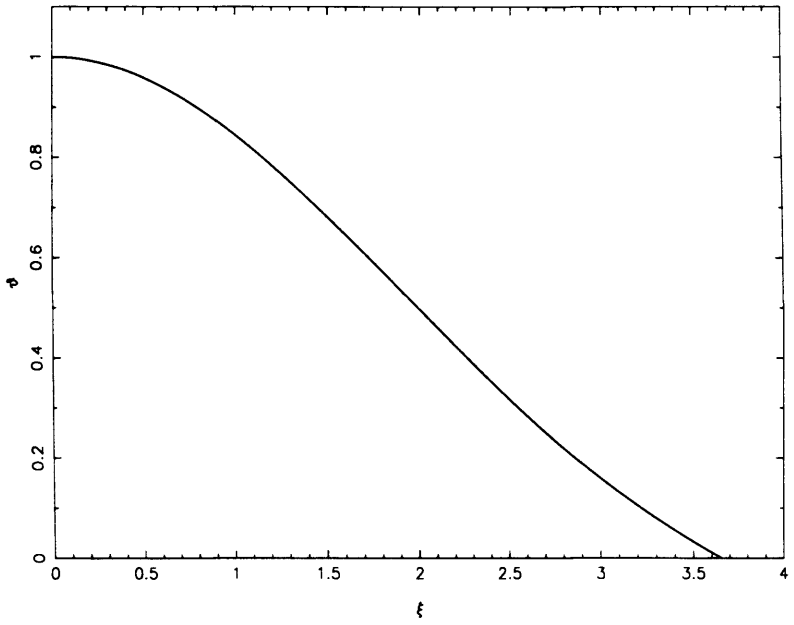

Figure 3.1: Solution to the Lane Emden equation for $n = 3/2$

which has the boundary condition

$$\theta(\xi = 0) = 0. \tag{3.23}$$

(3.20) and (3.22) must therefore be integrated in order to produce a tabulation of ξ and the corresponding values θ and ϕ. Since Equation (3.22) is singular at the origin, we start with a series expansion valid for small ξ, i.e.

$$\theta \approx 1 - \frac{1}{6}\xi^2 + \frac{n}{120}\xi^4 - ... \tag{3.24}$$

From (3.19), it follows that

$$\phi \approx \frac{1}{3}\xi^3 - \frac{n}{30}\xi^5 + ... \tag{3.25}$$

By incorporating this series expansion, θ and ϕ are calculated accurately when $\xi \ll 1$. The variation of θ with ξ is shown in Fig. 3.1. θ and ϕ are required for the next section in which we set up a uniform density sphere and then stretch it radially to reproduce the density profile of a polytrope with exponent 5/3.

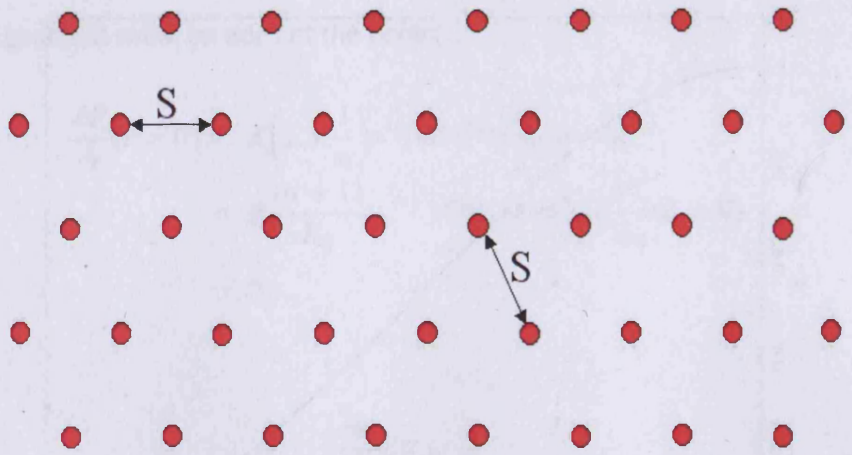

Figure 3.2: The two-dimensional lattice with inter-particle separation s.

3.2.3 Constructing the gas sphere

To set up the equilibrium isentropic sphere, we place equal-mass particles on an hexagonal close-packed array within a sphere of radius unity. Each particle has exactly 12 neighbours at an inter-particle separation s. This is achieved by firstly making a row of equally spaced particles along the x-axis. This row is then copied into the $x-y$ plane by translating each particle by the vector $n\mathbf{r}$, where $n = \pm 1, \pm 2, ...$, and

$$\mathbf{r} = \frac{s}{2}\hat{\mathbf{i}} + \frac{\sqrt{3}}{2}s\hat{\mathbf{j}}, \tag{3.26}$$

to produce an hexagonal close-packed layer. This layer is illustrated in Fig. 3.2.

In order to produce the next layer of the lattice, we translate each particle in this layer by the vector $n'\mathbf{r}'$, where $n' = \pm 1, \pm 2, ...$,

$$\mathbf{r}' = \frac{s}{2}\hat{\mathbf{i}} + \frac{\sqrt{3}}{6}s\hat{\mathbf{j}} + \sqrt{\frac{2}{3}}s\hat{\mathbf{k}}. \tag{3.27}$$

A sphere of radius $R_\circ$ is then cut out of this array.

The next step is to stretch this uniform-density sphere radially to reproduce the density profile of a polytrope with exponent 5/3.

The sphere is initially of radius $R_\circ$ with particle i at a radius r_i. Therefore, the mass interior to that particle is

$$M\left(\frac{r_i}{R_\circ}\right)^3. \tag{3.28}$$

In order to make an isentropic sphere with $\gamma = 5/3$, but still imposing that the radius and mass are unity, this particle must be moved to a new radius $r_i^\star$, conserving the mass interior to it. This position is defined as

$$r_i^\star = \xi_i R_\circ. \tag{3.29}$$

In the polytrope, each particle has a radius ξ/ξ_b, where ξ_b is the value of ξ at the boundary, and a mass $\phi(\xi_i)/\phi(\xi_b)$ interior to it. Hence, for each particle we must set the new radius by first finding the value of ξ_i which satisfies

$$\phi(\xi_i) = \phi(\xi_b)\left(\frac{r_i}{R_\circ}\right)^3. \tag{3.30}$$

The factor F by which the particle's position must be scaled is then

$$F = \frac{r_i^\star}{r_i} = \frac{\xi_i R_\circ}{r_i}, \tag{3.31}$$

and so each particle is now at a position

$$\begin{aligned} x_i^\star &= F x_i; \\ y_i^\star &= F y_i; \\ z_i^\star &= F z_i. \end{aligned} \tag{3.32}$$

Fig. 3.3 shows the overall structure of the sphere for $N_{\text{TOT}} = 5,895$ particles. The density profile of this unsettled sphere, compared to the analytical profile, is shown in Fig. 3.4.

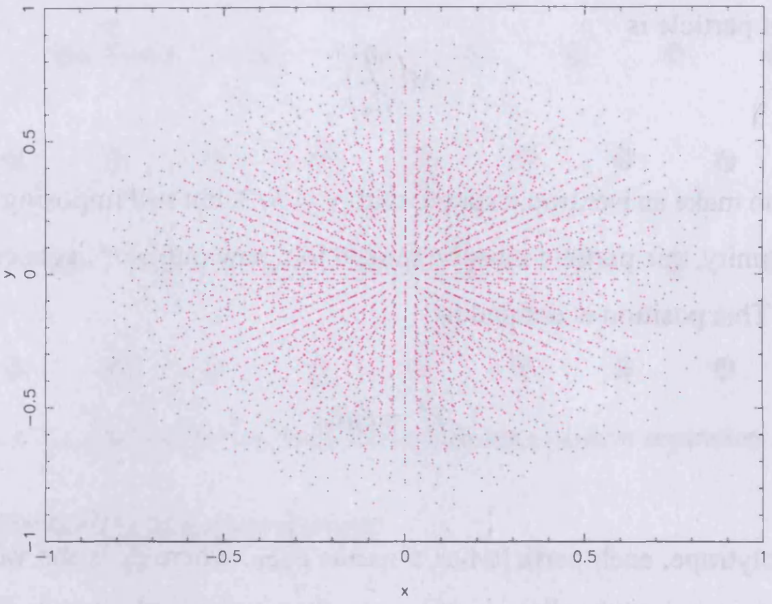

Figure 3.3: 2-D plot of the isentropic monatomic sphere, constructed as described in section 3.2.3.

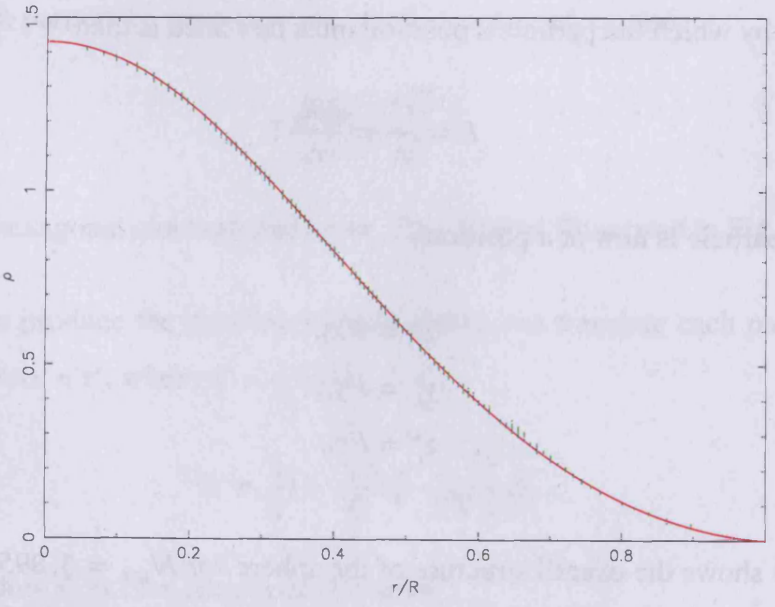

Figure 3.4: Density profile of sphere before settling. Red line represents the analytical solution; green points represent the actual particle densities.

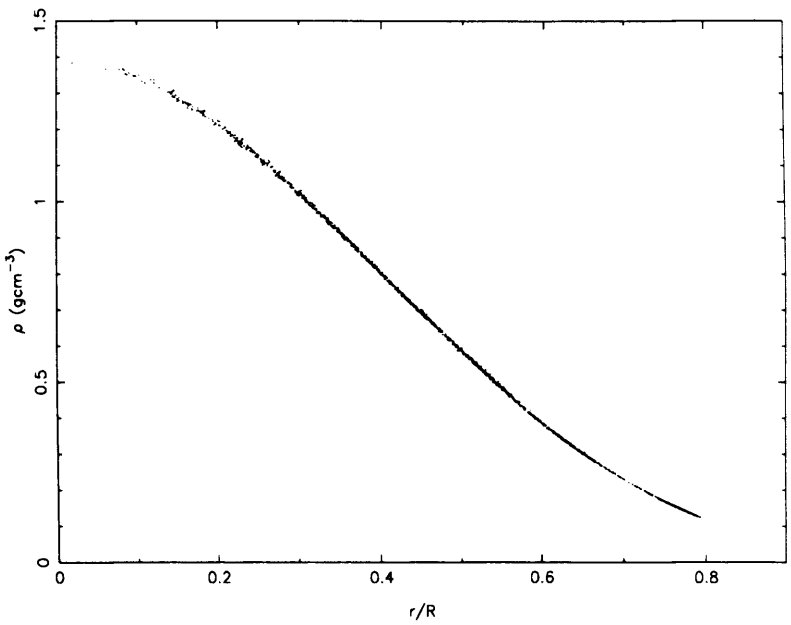

Figure 3.5: Density profile of the settled distribution.

The system is then relaxed by evolving the particle positions using the SPH code, until the net kinetic energy falls to a very small value (relative to the magnitude of the gravitational potential energy). The settled density profile is shown in Fig. 3.5. Another check to ensure the sphere is settled is to look at the magnitude of the hydrostatic accleration and gravitational acceleration of each particle. If the sphere is settled, they should be equal. A plot of this is shown in Fig. 3.6. The red open squares show the magnitude of the gravitational accelerations and the filled green circles show the magnitude of the hydrostatic accelerations, both as a function of the radius.

The next step is to perturb the sphere in order to undergo oscillation. To do this we must excite the fundamental radial mode.

3.2.4 Exciting the fundamental mode

To excite the fundamental mode, each particle is displaced radially from its equilibrium radius R to a new radius $R' = R[1 + A\zeta(R/R_\circ)]$, and then released from rest. Here $\zeta(s)$ $(0 \leq s \leq 1)$ is the eigenfunction of the fundamental radial mode of a self-gravitating

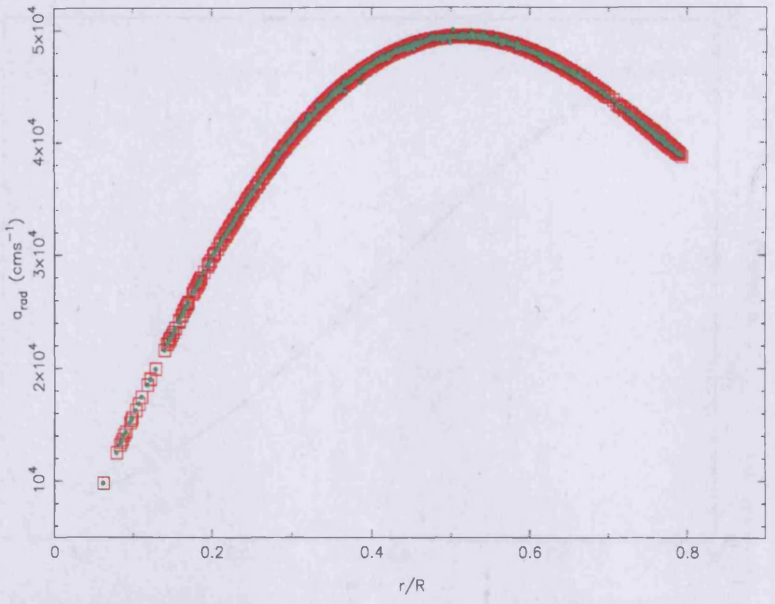

Figure 3.6: Radial components of the gravitational accelerations (red open squares) and hydrostatic accelerations (filled green circles) of the particles in a settled sphere, as a function of radius.

isentropic monatomic gas-sphere. This was very kindly supplied, in the form of a dense look-up table, by Alfred Gautschy. A is the initial amplitude of the oscillation, which we set to $A = 0.1$.

The density of the sphere then becomes

$$\rho'(R') = \rho(R)[1 + \zeta(R/R_\circ)]^{-2}\left[1 + \zeta(R/R_\circ) + R\frac{d\zeta}{dR}\right]^{-1}. \tag{3.33}$$

Originally, the gravitational acceleration is

$$a_{\mathrm{GRAV}}(R) = -\frac{GM(R)}{R^2}, \tag{3.34}$$

however, upon perturbation this acceleration then becomes

$$a'_{\rm GRAV}(R') = -\frac{GM(R)}{R'^2} \tag{3.35}$$

$$= a_{\rm GRAV}(R)[1+\zeta(R/R_\circ)]^{-2} \tag{3.36}$$

$$\simeq a_{\rm GRAV}(R)\{1-2\zeta(R/R_\circ)\}. \tag{3.37}$$

Likewise, the hydrostatic acceleration changes from being

$$a_{\rm HYDRO}(R) = -\frac{1}{\rho(R)}\frac{d\rho}{dR} \tag{3.38}$$

$$= -\gamma K\rho^{\gamma-2}(R)\frac{d\rho}{dR} \tag{3.39}$$

to

$$a'_{\rm HYDRO}(R') = -\gamma K\rho'^{(\gamma-2)}\frac{d\rho'(R')}{dR'} \tag{3.40}$$

$$= a_{\rm HYDRO}(R)[1+\zeta(R/R\circ)]^{-2(\gamma-1)}\left[1+\zeta(R)+R\frac{d\zeta}{dR}\right]^{-\gamma}\left\{1-\frac{\rho(R)}{d\rho/dR}\times\right.$$
$$\left.\left(2[1+\zeta(R/R_\circ)]^{-1}\frac{d\zeta}{dR}+\left[1+\zeta(R)+R\frac{d\zeta}{dR}\right]^{-1}\left[2\frac{d\zeta}{dR}+R\frac{d^2\zeta}{dR^2}\right]\right)\right\} \tag{3.41}$$

$$= -a_{\rm GRAV}(R)[1+\zeta(R/R_\circ)]^{-2(\gamma-1)}\left[1+\zeta(R/R_\circ)+R\frac{d\zeta}{dR}\right]^{-\gamma}\left\{1-\frac{\rho(R)}{d\rho/dR}\times\right.$$
$$\left.\left(2[1+\zeta(R/R_\circ)]^{-1}\frac{d\zeta}{dR}+\left[1+\zeta(R/R_\circ)+R\frac{d\zeta}{dR}\right]^{-1}\left[2\frac{d\zeta}{dR}+R\frac{d^2\zeta}{dR^2}\right]\right)\right\} \tag{3.42}$$

$$\simeq -a_{\rm GRAV}\left\{1-(3\gamma-2)\zeta(R/R_\circ)-\gamma R\frac{d\zeta}{dR}-\frac{\rho(R)}{d\rho/dR}\times\right.$$
$$\left.\left(2\left[2-2\zeta(R/R_\circ)-R\frac{d\zeta}{dR}\right]\frac{d\zeta}{dR}+\left[1-\zeta(R/R_\circ)-R\frac{d\zeta}{dR}\right]R\frac{d^2\zeta}{dR^2}\right)\right\}. \tag{3.43}$$

To be able to complete coherent radial oscillations, the restoring acceleration at

each radius of the perturbed sphere must be proportional to the displacement, so that

$$a'_{\rm TOTAL}(R') \equiv a'_{\rm GRAV}(R') + a'_{\rm HYDRO}(R') \tag{3.44}$$

$$\simeq a_{\rm GRAV}(R)\Big\{(3\gamma-4)\zeta(R/R_\circ) + \gamma R\frac{d\zeta}{dR} + \frac{\rho(R)}{d\rho(R)/dR}\times$$
$$\left(2\left[2-2\zeta(R/R_\circ) - R\frac{d\zeta}{dR}\right]\frac{d\zeta}{dR} + \left[1-\zeta(R/R_\circ) - R\frac{d\zeta}{dR}\right]R\frac{d^2\zeta}{dR^2}\right)\Big\} \tag{3.45}$$

$$\simeq -\omega^2 R\zeta(R/R_\circ), \tag{3.46}$$

where ω is the pulsation frequency. By ignoring the non-linear terms we obtain

$$\left\{\frac{R\rho(R)}{d\rho/dR}\right\}\frac{d^2\zeta}{dR^2} + \left\{\frac{4\rho(R)}{d\rho/dR} + \gamma R\right\}\frac{d\zeta}{dR} + \left\{3\gamma - 4 - \frac{\omega^2 R^3}{GM(R)}\right\}\zeta(R/R_\circ) = 0. \tag{3.47}$$

However, the equation of hydrostatic balance can be rewritten as

$$\frac{\rho(R)}{d\rho(R)/dR} = -\frac{\gamma K R^2 \rho^{\gamma-1}(R)}{GM(R)} \tag{3.48}$$

$$= -\frac{\gamma R^2 P(R)}{GM(R)\rho(R)}, \tag{3.49}$$

and so (3.47) simplifies to

$$\frac{d^2\zeta}{dR^2} + \left\{\frac{4}{R} - \frac{GM(R)}{R^2}\frac{\rho(R)}{P(R)}\right\}\frac{d\zeta}{dR} + \left\{\omega^2 - \frac{(3\gamma-4)GM(R)}{R^3}\right\}\frac{1}{\gamma}\frac{\rho(R)}{p(R)}\zeta(R/R_\circ) = 0. \tag{3.50}$$

The eigenfunction $\zeta(R)$ and eigenfrequency ω are obtained by solving this equation subject to

$$\zeta(R/R_\circ) = 1 \tag{3.51}$$

$$\frac{d\zeta}{dR}(R/R_\circ = 0) = 0. \tag{3.52}$$

3.2.5 Numerical Details

We represent the isentropic gas sphere with $N_{\rm TOT} = 5,895$ particles. Four simulations are performed, each with the same initial conditions, but evolved with $\Delta N_{\rm NEIB} =$ 0, 2, 5, and 10. We use the star formation code DRAGON, described in Chapter 2. The time-dependent artificial viscosity prescription is invoked (see Section 2.6.1 for a description). Each simulation is evolved for 100 freefall times.

3.3 Results

Figures 3.7 and 3.8 show oscillations simulated with $\Delta N_{\rm NEIB} = 0$, 2, 5, and 10. In Fig. 3.7, the quantity plotted is the mean x-displacement

$$\bar{x} = \frac{1}{N_{\rm TOT}} \sum_i \{|x_i|\} \tag{3.53}$$

(the mean being taken over all the particles, with equal weighting), as a function of time (normalised to the central freefall time, $t_{\rm FF}$, in the unperturbed equilbrium state). x_i is the distance of particle i from the centre of mass on the x axis. In Fig. 3.8, the quantity plotted is the total kinetic energy, normalised to the magnitude of the gravitational potential energy in the equilibrium state (i.e. $\mathcal{K}/|\Omega_0|$, where $\mathcal{K}$ is the total kinetic energy, Ω is the total gravitational potential energy, and subscript 0 refers to values in the unperturbed equilibrium state), again as a function of time (normalised to $t_{\rm FF}$). Some decay parameters are recorded in Table 3.1.

In addition to the fundamental mode, some additional modes are unintentionally excited from the outset. This is because, following relaxation, the equilibrium state of an isentropic monatomic sphere is not modelled exactly, due to the smoothing inherent in SPH. In particular, the density is underestimated near the centre and near the boundary. (This can be improved by increasing $N_{\rm NEIB}$ and $N_{\rm TOT}/N_{\rm NEIB}$, but that requires extra

computational resource.) Furthermore, the fundamental mode is excited with finite amplitude, but the eigenfunction is derived on the assumption of infinitesimal amplitude. (This can be moderated by adopting a lower value for A, but the test is not then relevant to real simulations of star formation, where ultimately we are concerned with non-linear perturbations.)

3.3.1 Decay of the fundamental mode

Setting aside the effect of other modes present in the initial conditions, the subsequent decay of the fundamental mode is in general due to two effects. First, the oscillation energy may be dissipated by artificial viscosity. The dissipation of energy due to artificial viscosity occurs wherever two neighbouring SPH particles approach one another. Second, the oscillation energy may be transferred to other modes. This occurs wherever local density or velocity fluctuations are created by the discrete nature of the SPH particles, or by the 'peculiar velocities' of individual SPH particles. Both effects occur more rapidly for larger values of $\Delta N_{\rm NEIB}$. (They also occur more rapidly for smaller values of $N_{\rm TOT}$ and smaller values of $N_{\rm NEIB}$, but these parameters are not varied here.)

When $\Delta N_{\rm NEIB} = 0$, the neighbour list of an SPH particle changes very seldom, and – when it does – very little. Therefore the acceleration experienced by the particle varies very slowly, and the velocity field is very smooth. The upshot is that neighbouring particles only approach one another very slowly, and the rate of dissipation due to artificial viscosity is low. Notwithstanding the slow rate of dissipation, there are small fluctuations in density and velocity, and these feed energy into other modes, so that the fundamental mode decays (see Figs. 3.7 & 3.8).

As $\Delta N_{\rm NEIB}$ is increased, the neighbour list of an SPH particle changes more frequently, and more abruptly. Therefore the acceleration experienced by the particle varies in a more idiosyncratic manner, and the velocity and density fields are more noisy. The upshot is that neighbouring particles often approach one another more rapidly, and the

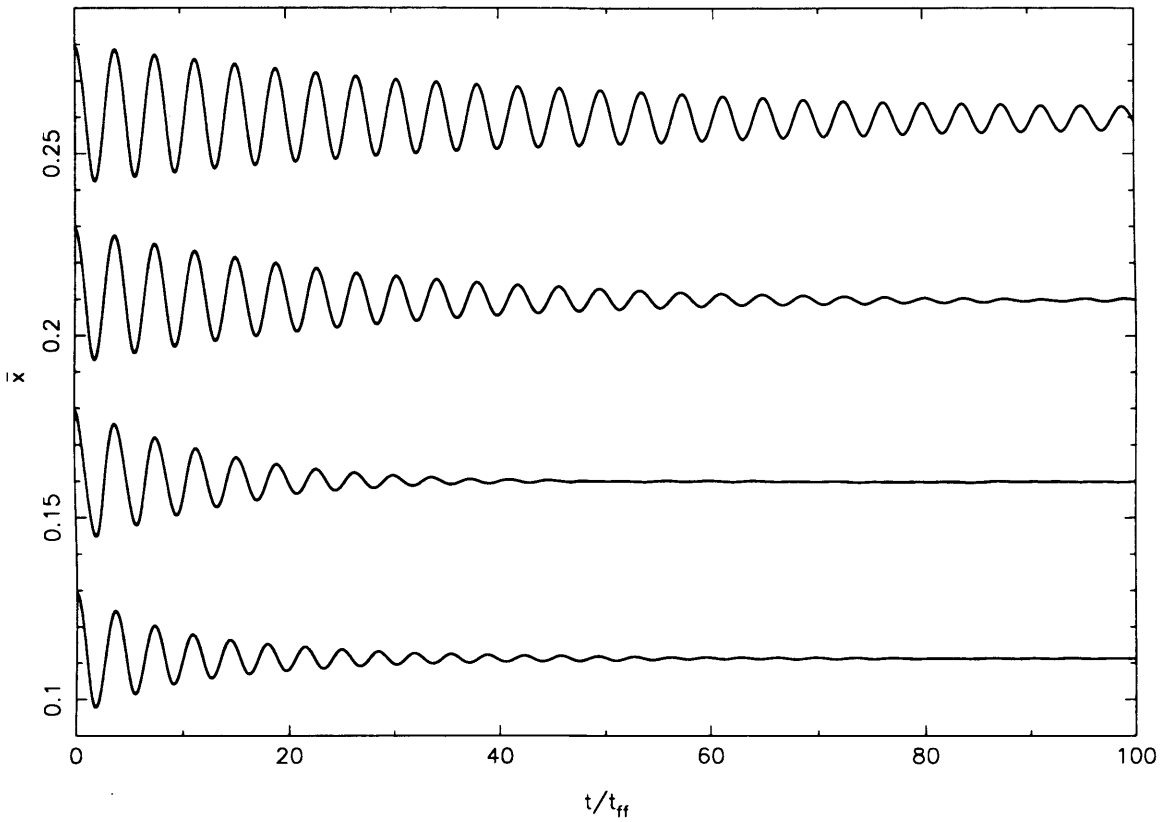

Figure 3.7: The mean x-displacement, $\bar{x}$ (where the mean is over all particles, with equal weighting), against time, t (in units of the freefall time in the equilibrium state, t_{FF}). The results are displaced vertically by Δx to fit them all on one plot. Reading from the top, (a) $\Delta N_{NEIB} = 0$, $\Delta x = 0$; (b) $\Delta N_{NEIB} = 2$, $\Delta x = -0.05$; (c) $\Delta N_{NEIB} = 5$, $\Delta x = -0.10$; (d) $\Delta N_{NEIB} = 10$, $\Delta x = -0.15$.

rate of dissipation due to artificial viscosity is therefore higher. In addition, the noisy velocity and density fields are very effective at feeding energy into other modes, so that the fundamental mode decays more rapidly (see Figs. 3.7 & 3.8).

In principle, the number of neighbours can change by $2\Delta N_{NEIB}$ at each timestep, from $N_{NEIB} - \Delta N_{NEIB}$ to $N_{NEIB} + \Delta N_{NEIB}$ or vice versa. Thus with $N_{NEIB} = 50$ and $\Delta N_{NEIB} = 10$, the number of neighbours can change from 40 to 60 or vice versa. In practice such large changes are unlikely, but it is still the case that increasing ΔN_{NEIB} results in increased fluctuations in the neighbour lists. In particular, particles in condensing regions tend to have N fluctuating between $\sim N_{NEIB}$ and $\sim (N_{NEIB} + \Delta N_{NEIB})$, whilst particles in expanding regions tend to have N fluctuating between $\sim N_{NEIB}$ and $\sim (N_{NEIB} - \Delta N_{NEIB})$.

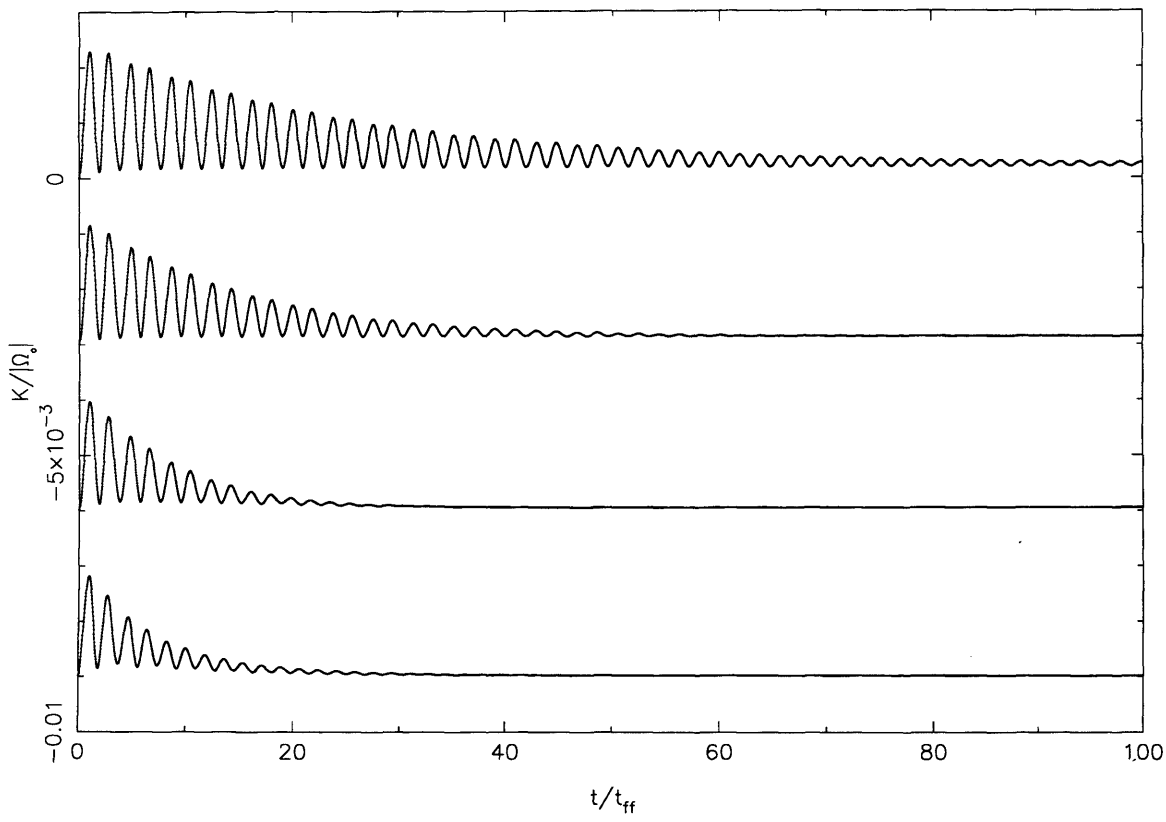

Figure 3.8: The total kinetic energy, $\mathcal{K}$ (normalised to the magitude of the self-gravitational potential energy in the equilibrium state, $|\Omega_0|$), against time, t (in units of the freefall time in the equilibrium state, t_{FF}). The results are displaced vertically by $\Delta\mathcal{K}$ to fit them all on one plot. Reading from the top, (a) $\Delta\mathcal{N}_{NEIB} = 0$, $\Delta\mathcal{K} = 0$; (b) $\Delta\mathcal{N}_{NEIB} = 2$, $\Delta\mathcal{K} = -0.003$; (c) $\Delta\mathcal{N}_{NEIB} = 5$, $\Delta\mathcal{K} = -0.006$; (d) $\Delta\mathcal{N}_{NEIB} = 10$, $\Delta\mathcal{K} = -0.009$.

3.3.2 Decay statistics

In Table 3.1, we record, for each value of $\Delta\mathcal{N}_{\rm NEIB}$ (column 1), the e-folding time of the amplitude of the fundamental mode, T_A, in terms of its period, $P_0 = 3.7t_{\rm FF}$ (column 2); the oscillation energy left after ten periods, $\mathcal{E}_{10}$, as a fraction of its initial value, $\mathcal{E}_0$ (column 3); and the simulation time to evolve the oscillating gas-sphere for 10 periods on eight 2.2Ghz Opteron CPUs each with 8GB memory (column 4). The oscillation energy is given by

$$\mathcal{E} = \mathcal{K} + (\mathcal{T} - \mathcal{T}_0) + (\Omega - \Omega_0), \tag{3.54}$$

where $\mathcal{K}$ is the kinetic energy, $\mathcal{T}$ is the thermal energy, and Ω is the gravitational potential energy. Again the subscript 0 indicates the unperturbed equilibrium state.

We note that the oscillation energy decays rather slowly due to dissipation, even with $\Delta\mathcal{N}_{\rm NEIB} = 10$. This is because the oscillations have low amplitude, and therefore the relative velocities between neighbouring particles are always very subsonic. Not only are the initial amplitudes low, but in the cases with high $\Delta\mathcal{N}_{\rm NEIB}$ the amplitudes decay rapidly due to numerical diffusion. In other words, when $\Delta\mathcal{N}_{\rm NEIB}$ is high, the rate of dissipation is reduced because diffusion rapidly spreads the oscillation energy amongst many different modes and thereby reduces even further the relative velocities between neighbouring particles. This is reflected in the results presented in Fig.3.8 and the third column of Table 3.1. Because the decay of the fundamental mode is largely due to numerical diffusion, the oscillation energy only falls by a few percent after ten periods (see the third column of Table 3.1), whereas the amplitude of the variation in kinetic energy falls much more rapidly. The variation in kinetic energy eventually disappears, not because the kinetic energy itself disappears, but because numerical diffusion transfers oscillation energy to other modes with different periods and different phases. Consequently the oscillation energy becomes thermalised, and $\mathcal{K}$ is finite but approximately constant.

Table 3.1: Decay of the fundamental mode. The first column gives $\Delta\mathcal{N}_{\rm NEIB}$. The second column gives the e-folding time for the amplitude of the fundamental mode, T_A, as a multiple of its period, P_0. The third column gives the net oscillation energy left after 10 periods, $\mathcal{E}_{10}$, as a fraction of the initial oscillation energy, $\mathcal{E}_0$. The fourth column gives the simulation time to evolve the oscillating gas-sphere for 10 periods on eight 2.2Ghz Opteron CPUs each with 8GB memory, t_{10}.

$\Delta\mathcal{N}_{\rm NEIB}$	T_A/P_0	$\mathcal{E}_{10}/\mathcal{E}_0$	t_{10}/s
0	13.6	0.955	9545
2	7.6	0.939	9403
5	3.8	0.927	8996
10	3.1	0.925	8164

The simulations presented here have been continued for 100 periods. In this limit, there are so many modes excited, with so many different phases, that the gas-spheres become virialised with

$$2\mathcal{K} + 2\mathcal{T} + \Omega \simeq 0; \tag{3.55}$$

$\mathcal{K}$ is still finite.

3.4 Summary

From the plots in Figs. 3.7 & 3.8, and the above discussion, we infer that the results obtained with $\Delta\mathcal{N}_{\rm NEIB} = 0$ are far more reliable than those obtained with $\Delta\mathcal{N}_{\rm NEIB} = 10$, and significantly more reliable even than those obtained with $\Delta\mathcal{N}_{\rm NEIB} = 2$, both in terms of having less dissipation and – more importantly – in terms of having less numerical diffusion.

Setting $\Delta\mathcal{N}_{\rm NEIB} = 0$ also requires little extra computation. For example, to follow 10 oscillation periods with $\Delta\mathcal{N}_{\rm NEIB} = 0$ takes only 17% longer than with $\Delta\mathcal{N}_{\rm NEIB} = 10$.

Moreover, 7% of this increase is due to the fact that with $\Delta N_{\rm NEIB} = 0$ the sphere continues to oscillate with a significant amplitude after 10 periods, and therefore the timestep remains short. When allowance is made for this, the real cost of reducing $\Delta N_{\rm NEIB}$ from 10 to 0 is only a 10% increase in computation.

Therefore our principal conclusions are (i) that $\Delta N_{\rm NEIB} = 0$ should be the default option for SPH codes which adapt smoothing lengths in this way; and (ii) that the Lucy test provides a very useful way of evaluating the fidelity of codes used in simulations of star formation.

We emphasise that we have not set out to reproduce as accurately or economically as possible acoustic oscillations of a self-gravitating isentropic sphere in the fundamental mode. We have simply demonstrated how the results produced using a standard SPH code, with a modest number of particles ($N_{\rm TOT} = 5,895$) depend on $\Delta N_{\rm NEIB}$. There are adjustments to SPH which will improve (extend) the timescales for numerical dissipation and numerical diffusion in the present simulation. For example, using standard artificial viscosity with $\alpha = 0$ and $\beta = 0.1$ increases the e-folding time for the fundamental mode to ~ 60 oscillation periods, but at the same time compromises the shock-capturing ability of the code so that it can not then be used for simulations in which shocks are likely. Similarly, the e-folding time for the fundamental mode can be extended by increasing $N_{\rm NEIB}$ or $N_{\rm TOT}/N_{\rm NEIB}$, but this must inevitably be at the expense of resources which are needed elsewhere, *viz.* to maximise the extent and/or duration of a simulation.

The useful duration of the present simulation can be identified with the e-folding time of the fundamental mode, which with $\Delta N_{\rm NEIB} = 0$ is 13.6 oscillation periods, but with $\Delta N_{\rm NEIB} = 10$ is only 3.1 oscillation periods.

We propose that Adaptive Mesh Refinement codes used for simulating star formation aim to reproduce or improve upon the results produced here, using comparable computational resources. In addition, they should do so for a gas-sphere which moves at constant velocity relative to the underlying Cartesian grid, in order to match the La-

grangian advantages of SPH.

Chapter 4

Simulating star formation in molecular cores

In this chapter we simulate the collapse and fragmentation of relatively isolated low-turbulence cores. We perform multiple realisations of a large ensemble of cores, all having the same mass, initial density profile and turbulent power spectrum, but with three different initial levels of turbulence. This problem was first investigated by Goodwin et al. (2004b), using a simple barotropic equation of state. However, a barotropic equation of state is not realistic, because it does not take into account the thermal history of protostellar gas, and it is unable to capture thermal inertia effects. We therefore revisit this problem, but now using a new treatment of the energy equation devised by Stamatellos et al. (2007b) which treats the energy equation and the associated radiative transport more realistically. We quantify the differences between simulations performed using a barotropic equation of state and simulations which use the new treatment of the energy equation and associated radiative transport. We also compute the statistical properties of the resulting stars, including their mass distribution, kinematics and binary statistics.

4.1 Introduction

Current observations suggest that a significant fraction of low-mass stars condense out of small, relatively isolated, low-turbulence prestellar cores, with each core spawning a small cluster of stars. The evidence for this mode of star formation is as follows.

Isolated cores

The evidence supporting the idea that the cores are relatively isolated comes from a number of studies. André et al. (2007) have carried out a study of the L1688 protocluster in the central Ophiuchus molecular cloud. They estimate the one-dimensional intercore velocity dispersion (i.e. the dispersion in the bulk velocities of the cores relative to their neighbours) to be $\Delta v_{\rm INTERCORE} \simeq 0.36\,{\rm km\,s^{-1}}$, the collision cross-section between cores to be $\sigma_{\rm COLL} \simeq 10^{-3}\,{\rm pc^2}$ (including the effect of gravitational focussing), and the number-density of cores to be $n_{\rm CORE} \simeq 80\,{\rm pc^{-3}}$. Hence the mean time between collisions between cores is

$$t_{\rm COLL} \simeq \frac{1}{n_{\rm CORE}\,\sigma_{\rm COL}\,\Delta v_{\rm INTERCORE}} \sim 30,000\,{\rm kyr}. \qquad (4.1)$$

In contrast, the condensation timescale for a typical core is $t_{\rm COND} \sim 100\,{\rm kyr}$. Therefore a typical core is likely to have collapsed and fragmented, internally, before it interacts with a neighbouring core.

Low turbulence

The observed turbulent motions in low-mass prestellar cores are estimated to be subsonic, or occasionally transsonic (e.g. Myers 1983; Myers et al. 1991; Myers 1998; André et al. 2007). Indeed, Myers (1998) concludes that the decay of turbulence to subsonic levels may well be a prerequisite for the formation of low-mass protostars. If the level of turbulence is characterised by the parameter

$$\alpha_{\rm TURB} \equiv \frac{E_{\rm TURB}}{|E_{\rm GRAV}|}, \qquad (4.2)$$

where $E_{\rm TURB}$ is the turbulent energy, and $E_{\rm GRAV}$ is the self-gravitational potential energy, then the typical values in low-mass prestellar cores are mainly in the range $0 < \alpha_{\rm TURB} \lesssim 0.3$ (see Jijina et al. 1999; and Fig. 2 in Goodwin et al. 2004a). We note that this is much lower than the values used by Bate et al. (2002a,b, 2003) to initiate the evolution of more massive cluster-forming cores.

Each core spawns only a few stars

The evidence that each core spawns only a few stars comes from the binary statistics of young low-mass stars, which show that a high fraction are in binary or higher-order multiple systems. The binary fraction decreases with decreasing primary mass, and with increasing age, but for a 1 $M_{\odot}$ primary it is still ~ 60% in the field (Duquennoy & Mayor 1991). Goodwin & Kroupa (2005) and Hubber & Whitworth (2005) have shown that this high multiplicity requires newly-born stars to complete their early dynamical evolution in small sub-clusters containing just a few stars (i.e. $N_{\rm SUBCLUSTER} \sim 4 \pm 1$ stars). This is because, in a small sub-cluster, N-body interactions tend rather quickly to deliver a tight binary, usually comprising the two most massive stars, and to eject most of the remaining stars as singles (McDonald & Clarke 1993; Goodwin & Kroupa 2005; Hubber & Whitworth 2005). Therefore, if $N_{\rm SUBCLUSTER}$ is increased, a higher proportion of stars are ejected as singles, and therefore the primordial binary fraction is reduced, in contradiction with the observations.

4.1.1 The influence of the level of turbulence

Goodwin et al. (2004a,b) were the first to explore how the level of turbulence affects the collapse and fragmentation of small, relatively isolated prestellar cores. In their study, they simulate the evolution of a large ensemble of cores. The cores are all of mass $M = 5.4 M_{\odot}$ and all have the same initial density profile and turbulent power spectrum. They vary the initial level of turbulence, as measured by the ratio of the turbulent kinetic

energy to gravitational potential energy, so that

$$\alpha_{\rm TURB} \equiv \frac{E_{\rm TURB}}{|E_{\rm GRAV}|} = 0.,\ 0.01,\ 0.025,\ 0.05,\ 0.10,\ 0.25. \qquad (4.3)$$

For each value of $\alpha_{\rm TURB}$, they perform many different simulations, each with a different realisation of the initial turbulent velocity field, in order to obtain good statistics.

They find that the minimum level of turbulence required to produce multiple systems is $\alpha_{\rm TURB} = 0.05$. Further to this, increasing the level of turbulence in the core increases both the total number of stars formed, and the proportion of brown dwarfs. The mass distribution produced appears to be bimodal. It consists of a low-mass peak occupied by brown dwarfs ejected from the core before they can accrete much mass, and a higher mass peak occupied by stars which have remained in the core and grown by accretion to become hydrogen-burning stars.

In a subsequent paper, Goodwin et al. (2006) investigate the effect of the turbulent power spectrum on the fragmentation of cores with low levels of turbulence. They consider different turbulent power spectra, of the form $P_k \propto k^{-x}$, with $x = 2$, 3, 4 and 5, and find that increasing x results in more fragments. This is because increasing x gives more turbulent power on long wavelengths, and hence more large-scale fragmentation resulting in separate protostars.

However, in their simulations Goodwin et al. (2004a,b, 2006) use a simple barotropic equation of state. In practice this is not realistic, because (a) a barotropic equation of state does not take into account the thermal history of a protostar, which depends on its environment, geometry and mass, and (b) a barotropic equation of state is unable to capture thermal inertia effects, which are critical at the stage when fragmentation occurs. By thermal inertia we mean the situation when the thermal timescale is longer than the dynamical timescale.

We have therefore revisited the study of Goodwin et al. (2004a,b), but now using

a new treatment of the energy equation due to Stamatellos et al. (2007b). This new treatment captures the critical thermal and radiative effects and is therefore much more realistic than a barotropic equation of state. We shall describe this technique in more detail later in the chapter.

4.2 Initial Conditions

We use the same initial conditions as Goodwin et al. (2004b). These initial conditions are designed to fit the observed properties of prestellar cores, such as L1544. The density profiles of prestellar cores are approximately flat in a central region of a few thousand AU, then fall as $r^{-\eta}$ with $2 \leq \eta \leq 5$ in the outer regions, until eventually merging with the background (e.g. Ward-Thompson et al. 1994; André et al. 1996; Ward-Thompson et al. 1999; André et al. 2000). A Plummer-like profile of the form

$$\rho(r) = \frac{\rho_{\rm KERNEL}}{(1 + (r/R_{\rm KERNEL})^2)^2} \tag{4.4}$$

gives a good fit to the observed density of these cores. $\rho_{\rm KERNEL}$ is the central density ($3 \times 10^{-18}\,{\rm g\,cm^{-3}}$) and $R_{\rm KERNEL}$ is the radius inside which the density is approximately uniform (5,000 AU). The core extends out to $R_{\rm CORE} = 50,000$ AU, so its total mass $M_{\rm TOT} = 5.4 M_{\odot}$. The mass inside $R_{\rm KERNEL}$ is only $M_{\rm KERNEL} = 1.1\,{\rm M}_{\odot}$.

We start with an isothermal core at $T = 10$ K, giving a ratio of thermal to gravitational energy of

$$\alpha_{\rm THERM} \equiv \frac{E_{\rm THERM}}{|E_{\rm GRAV}|} \simeq 0.3\,. \tag{4.5}$$

We impose a divergence-free Gaussian random velocity field on each core (Bate et al. 2002a,b, 2003; Bonnell et al. 2003). This approach of initialising the velocity field is normally referred to as turbulence, but we recognise that it is not self-consistent, fully developed turbulence (c.f. Offner et al. 2008). We set the power spectrum of the velocity field to $P(k) \propto k^{-4}$, which mimics that observed in giant molecular clouds

and cores (Burkert & Bodenheimer 2000). The level of turbulence is characterised by $\alpha_{\rm TURB} = 0.05, 0.10, 0.25$, where $\alpha_{\rm TURB}$ is defined in Equation (4.3). This is a fairly low level of turbulence in comparison to some simulations (e.g. Bate et al. 2002a,b, 2003) but we note these are typical values for the level of turbulence in observed low-mass cores (see catalogue of Jijina et al. 1999).

4.2.1 Using a barotropic equation of state

At low densities ($\rho < \rho_{\rm CRIT} \simeq 10^{-13}\,{\rm g\,cm^{-3}}$) the gas in a core is approximately isothermal at $T = 10$K. Once the density exceeds $\rho_{\rm CRIT}$, the cooling radiation becomes trapped by the high optical depth. This results in the gas switching from being approximately isothermal to being approximately adiabatic (Larson 1969; Tohline 1982; Masunaga & Inutsuka 2000). This can be modelled using a barotropic equation of state:

$$\frac{P(\rho)}{\rho} \equiv c_s^2(\rho) = c_0^2 \left[1 + \left(\frac{\rho}{\rho_{\rm CRIT}} \right)^{2/3} \right] \qquad (4.6)$$

where P is the pressure, ρ is the density, c_s is the isothermal sound speed and $c_0 = 0.19{\rm km\,s^{-1}}$ is the isothermal sound speed in molecular gas at $T = 10$K. Until the temperature rises above $\sim 100\,{\rm K}$, the rotational degrees of freedom of molecular hydrogen are not significantly excited, and so the effective adiabatic exponent is $\gamma \sim 5/3$. This in turn means that the Jeans mass increases rather rapidly once the density exceeds $\rho_{\rm CRIT}$, roughly as $M_{\rm JEANS} \propto \rho^{1/2}$. We note that the simulations of Bate et al. (2002a,b, 2003) and Bonnell et al. (2003) use a similar barotropic equation of state but with $\gamma = 7/5$ in the adiabatic regime; consequently their Jeans mass increases much more slowly, $M_{\rm JEANS} \propto \rho^{1/10}$, giving a greatly extended window of opportunity for fragmentation at low masses.

Equation (4.6) gives a good fit to the run of temperature with density at the centre of a collapsing non-rotating $1{\rm M}_\odot$ protostar, as obtained by the detailed computations of Masunaga & Inutsuka (2000). However, simulations producing condensations which

have masses below $1M_{\odot}$ and/or are non-spherical are compromised by this assumption. Such condensations will tend to become opaque and heat up at a significantly higher density. This is because the optical depths are lower, and because the rate of compressional heating is slower.

In addition to this, a barotropic equation of state does not capture properly thermal inertia effects, such as the complex system of interacting pressure waves which dominates the dynamics when the gas becomes adiabatic. At this stage, the thermal timescale suddenly becomes longer than the dynamical timescale. This is when fragmentation occurs, as evidenced by the simulations of Boss et al. (2000). Therefore, capturing the thermal inertia effects is crucial, and requires a more realistic treatment of the energy equation and associated radiation transport.

4.2.2 New energy treatment

Stamatellos et al. (2007a) have introduced a new alogorithm for treating the thermal and radiative effects influencing the energy equation. The algorithm allows the thermal behaviours of protostars of different mass, in different environments and having different metallicities to be distinguished, without having to treat in detail the associated 3-D, frequency-dependent radiative transfer. It also captures the trapping of cooling radiation, opacity changes, and internal energy changes due to the effect of rotational and vibrational degrees of freedom of H_2, H_2 dissociation and the ionization of H^o, He^o and He^+.

This algorithm uses an SPH particle's density, ρ_i, temperature, T_i, and gravitational potential, ψ_i, to estimate the mean optical depth, $\bar{\tau}_i$, between the SPH particle and the ambient medium. The mean optical depth then determines the extent to which the SPH particle is shielded from external radiation and the extent to which the SPH particle's cooling radiation is trapped. To determine this, a spherically-symmetric pseudo-cloud is defined around each particle, through which the particle heats and cools. The details

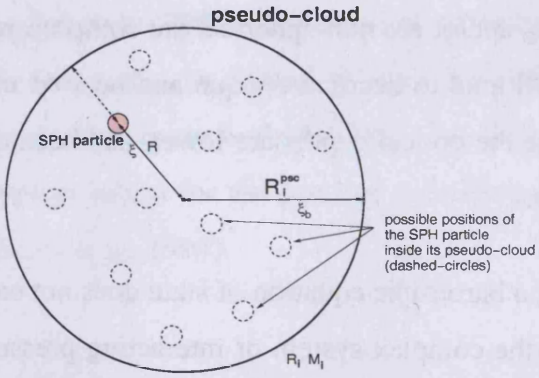

Figure 4.1: Schematic representation of the pseudo-cloud around an SPH particle.The location of the SPH particle inside its pseudo-cloud is not specified. Taken from Stamatellos et al. (2007a).

of the algorithm are explained here, but see Stamatellos et al. (2007a) for a detailed description and various tests.

The SPH particle i is embedded at radius $R = \xi R_0$, in the pseudo-cloud with central density ρ_C, scale-length R_0, and polytropic index n. Fig. 4.1 shows a schematic diagram of the pseudo-cloud around an SPH particle. ρ_C and R_0 are chosen such that they reproduce the actual density and gravitational potential of the SPH particle at the dimensionless radius ξ, i.e.

$$\rho_C \theta^n(\xi) = \rho_i , \tag{4.7}$$

$$-4\pi G \rho_C R_0^2 \phi(\xi) = \psi_i . \tag{4.8}$$

where $\theta(\xi)$ is the Lane-Emden Function for index n (Chandrasekhar 1939),

$$\phi(\xi) = -\xi_B \frac{d\theta}{d\xi}(\xi_B) + \theta(\xi) , \tag{4.9}$$

and ξ_B is the dimensionless boundary of the polytrope (see Section 3.2.1 for a derivation of this function).

By fixing n and giving ξ an arbitrary value – but not exceeding ξ_B – we obtain

$$\rho_C = \rho_i \theta^{-n}(\xi), \tag{4.10}$$

$$R_O = \left[\frac{-\psi_i \theta^n(\xi)}{4\pi G \rho_i \phi(\xi)}\right]^{1/2}. \tag{4.11}$$

The central temperature of the pseudo-cloud is also chosen in the same manner to give the actual temperature of the SPH particle, i.e.

$$T_C \theta(\xi) = T_i, \tag{4.12}$$

$$T_C = T_i \theta^{-1}(\xi). \tag{4.13}$$

The column density on a radial line from this radius to the boundary of the pseudo-cloud is then given by

$$\begin{aligned}\Sigma_i(\xi) &= \int_{\xi'=\xi}^{\xi'=\xi_B} \rho_C \theta^n(\xi') R_O d\xi' \\ &= \left[\frac{-\psi_i \rho_i}{4\pi G \phi(\xi) \theta^n(\xi)}\right]^{1/2} \int_{\xi'=\xi}^{\xi'=\xi_B} \theta^n(\xi')\, d\xi'.\end{aligned} \tag{4.14}$$

The pseudo-mean column density is obtained by taking a mass-weighted average of $\Sigma_i(\xi)$ over all possible values of ξ, i.e.

$$\begin{aligned}\bar{\Sigma}_i &= \left[-\xi_B^2 \frac{d\theta}{d\xi}(\xi_B)\right]^{-1} \int_{\xi=0}^{\xi=\xi_B} \Sigma_i(\xi)\ \theta^n(\xi)\xi^2 d\xi \\ &= \zeta_n \left[\frac{-\psi_i \rho_i}{4\pi G}\right]^{1/2}.\end{aligned} \tag{4.15}$$

$\left[-\xi_B^2 \frac{d\theta}{d\xi}(\xi_B)\right]$ is the total dimensionless mass of the polytrope, $\theta^n(\xi)\xi^2 d\xi$ is the dimensionless mass element between ξ and $\xi + d\xi$, and

$$\zeta_n = \left[-\xi_B^2 \frac{d\theta}{d\xi}(\xi_B)\right]^{-1} \int_{\xi=0}^{\xi=\xi_B} \int_{\xi'=\xi}^{\xi'=\xi_B} \theta^n(\xi') d\xi' \left[\frac{\theta^n(\xi)}{\phi(\xi)}\right]^{1/2} \xi^2 d\xi. \tag{4.16}$$

We adopt a value of $n = 2$ which corresponds to a polytropic exponent of 3/2.

To calculate the pseudo-mean optical depth, we take the same approach as with the pesudo-mean column density. If the Rosseland-mean opacity is a function of density and temperature only, $\kappa_R(\rho, T)$, the radial optical depth from radius $R = \xi R_0$ to the boundary of the pseudo-cloud is

$$\begin{aligned}\tau_i(\xi) &= \int_{\xi'=\xi}^{\xi'=\xi_B} \kappa_R\left(\rho_c\theta^n(\xi'), T_c\theta(\xi')\right)\rho_c\theta^n(\xi')R_0 d\xi' \\ &= \left[\frac{-\psi_i\rho_i\theta^n(\xi)}{4\pi G\phi(\xi)}\right]^{1/2} \times \\ &\quad \int_{\xi'=\xi}^{\xi'=\xi_B} \kappa\left(\rho_i\left[\frac{\theta(\xi')}{\theta(\xi)}\right]^n, T_i\left[\frac{\theta(\xi')}{\theta(\xi)}\right]\right)\left[\frac{\theta(\xi')}{\theta(\xi)}\right]^n d\xi', \end{aligned} \tag{4.17}$$

and the mass-weighted pseudo-mean optical depth is

$$\begin{aligned}\bar{\tau}_i &= \left[-\xi_B^2\frac{d\theta}{d\xi}(\xi_B)\right]^{-1}\left[\frac{-\psi_i\rho_i}{4\pi G}\right]^{1/2}\int_{\xi=0}^{\xi=\xi_B}\int_{\xi'=\xi}^{\xi'=\xi_B} \times \\ &\quad \kappa_R\left(\rho_i\left[\frac{\theta(\xi')}{\theta(\xi)}\right]^n, T_i\left[\frac{\theta(\xi')}{\theta(\xi)}\right]\right)\theta^n(\xi')d\xi'\left[\frac{\theta^n(\xi)}{\phi(\xi)}\right]^{1/2}\xi^2 d\xi. \end{aligned} \tag{4.18}$$

We define a pseudo-mean mass opacity

$$\bar{\kappa}_i = \frac{\bar{\tau}_i}{\bar{\Sigma}_i}, \tag{4.19}$$

which is a function of ρ_i and T_i (if n is fixed). This quantity needs only be calculated once, and so can be stored in a dense look-up table. For point (ρ, T), the pseudo-mean opacity is given by

$$\begin{aligned}\bar{\kappa}_R(\rho, T) &= \left[-\zeta_n\xi_B^2\frac{d\theta}{d\xi}(\xi_B)\right]^{-1}\int_{\xi=0}^{\xi=\xi_B}\int_{\xi'=\xi}^{\xi'=\xi_B} \times \\ &\quad \kappa_R\left(\rho\left[\frac{\theta(\xi')}{\theta(\xi)}\right]^n, T\left[\frac{\theta(\xi')}{\theta(\xi)}\right]\right)\left[\frac{\theta^{n+2}(\xi)}{\phi(\xi)}\right]^{1/2} d\xi'\,\xi^2 d\xi. \end{aligned} \tag{4.20}$$

From Equation 4.19 we can calculate the pseudo-mean optical depth $\bar{\tau}_i$. This takes into account the radiation absorbed or emitted by i when it passes through the surrounding material, which will have a different density and temperature, and hence different

opacity. The parameters are then used to calculate the net radiative heating rate

$$\left.\frac{du_i}{dt}\right|_{\rm RAD} = \frac{4\,\sigma_{\rm SB}\,(T_{\rm o}^4 - T_i^4)}{\bar{\Sigma}_i^2\,\bar{\kappa}_{\rm R}(\rho_i, T_i) + \kappa_{\rm P}^{-1}(\rho_i, T_i)}\,, \tag{4.21}$$

where $\sigma_{\rm SB}$ is the Stefan-Boltzmann constant, and $\kappa_{\rm P}(\rho_i, T_i)$ is the Plank-mean opacity. $\rm T_o$ is the background temperature and the term involving $\rm T_o^4(\mathbf{r}_i)$ in Equation (4.21) represents the radiative heating due to the background radiation field. The negative term involving $\rm T_i^4$ represents the radiative cooling of the SPH particle. If $T_i^4 \gg T_{\rm o}^4(\mathbf{r}_i)$, we can neglect the heating term and consider two limiting regimes:

(i) If $\bar{\Sigma}_i^2\,\bar{\kappa}_{\rm R}(\rho_i, T_i) \ll \kappa_{\rm P}^{-1}(\rho_i, T_i)$, we are in the optically thin cooling regime and Equation (4.21) approximates to

$$\left.\frac{du_i}{dt}\right|_{\rm RAD} \simeq -4\,\sigma_{\rm SB}\,T_i^4\,\kappa_{\rm P}(\rho_i, T_i)\,, \tag{4.22}$$

in exact agreement with the definition of the Planck-mean opacity.

(ii) If $\bar{\Sigma}_i^2\,\bar{\kappa}_{\rm R}(\rho_i, T_i) \gg \kappa_{\rm P}^{-1}(\rho_i, T_i)$, we are in the optically thick cooling regime and Equation (4.21) approximates to

$$\left.\frac{du_i}{dt}\right|_{\rm RAD} \simeq -\frac{4\,\sigma_{\rm SB}\,T_i^4}{\bar{\Sigma}_i^2\,\bar{\kappa}_{\rm R}(\rho_i, T_i)} = -\frac{c\,a_{\rm SB}\,T_i^4}{\bar{\Sigma}_i\,\bar{\tau}_i}\,, \tag{4.23}$$

where c is the speed of light, $a_{\rm SB}$ is the radiant energy density constant. The second expression is obtained by substituting $4\sigma_{\rm SB} = ca_{\rm SB}$ and $\bar{\Sigma}_i\,\bar{\kappa}_{\rm R}(\rho_i, T_i) = \bar{\tau}_i$.

Gas-phase chemistry

To treat the gas-phase chemistry we assume the gas is 70% hydrogen and 30% helium by mass, since metals make very little contribution to the equation of state. Hydrogen is molecular at low temperatures, but is dissociated as the temperature rises, and then ionised. Helium is neutral atomic at low temperatures, but as the temperature increases it

becomes ionised, first to He^+, and then to He^{++}. The Saha equations give the abundances of these constituents (e.g. Black & Bodenheimer 1975). These equations assume that the dissociation of H_2 is complete before ionization of H^o begins; and similarly, that the ionization of He^o is complete before the ionization of He^+ begins.

Equation of state

We define $y = n_{H^o}/2n_{H_2}$ to be the degree of dissociation of hydrogen, $x = n_{H^+}/n_{H^o}$ to be the degree of ionization of hydrogen, $z_1 = n_{He^+}/n_{He^o}$ to be the degree of single ionisation of helium, and $z_2 = n_{He^{++}}/n_{He^+}$ to be the degree of double ionisation of helium. The mean molecular weight is then given by

$$\mu_i = \mu(\rho_i, T_i) = \left[(1 + y + 2xy)\frac{X}{2} + (1 + z_1 + z_1 z_2)\frac{Y}{4}\right]^{-1}. \quad (4.24)$$

For densities up to $\sim 0.03\,\mathrm{g\,cm^{-3}}$ the ideal gas approximation holds, and hence the gas pressure is

$$P_i = \frac{\rho_i k_B T_i}{\mu_i m_H}. \quad (4.25)$$

Specific internal energy of the gas

The specific internal energy (energy per unit mass) of an SPH particle i is given by

$$u_i = u_{H_2} + u_H + u_{He} + u_{H_2 DISS} + u_{H\,ION} + u_{He\,ION} + u_{He^+ ION}, \quad (4.26)$$

where

$$u_{H_2} = X(1-y)\left[\frac{3}{2} + c_i(T_i)\right]\frac{k_B T_i}{2m_H}, \quad (4.27)$$

$$u_H = Xy(1+x)\frac{3k_B T_i}{2m_H}, \quad (4.28)$$

$$u_{He} = Y(1+z_1+z_1z_2)\frac{3k_B T_i}{8m_H}, \quad (4.29)$$

$$u_{H_2DISS} = Xy\frac{\mathcal{D}_{H_2DISS}}{2m_H}, \quad (4.30)$$

$$u_{H\,ION} = Xxy\frac{\mathcal{I}_{H\,ION}}{m_H}, \quad (4.31)$$

$$u_{He\,ION} = Yz_1(1-z_2)\frac{\mathcal{I}_{He\,ION}}{4m_H}, \quad (4.32)$$

$$u_{He^+ION} = Yz_1z_2\frac{\mathcal{I}_{He^+ION}}{4m_H}, \quad (4.33)$$

Here, $\mathcal{D}_{H_2DISS} = 4.5\,eV$ is the dissociation energy of H_2; $\mathcal{I}_{H\,ION} = 13.6\,eV$, $\mathcal{I}_{He\,ION} = 24.6\,eV$ and $\mathcal{I}_{He^+ION} = 54.4\,eV$ are the ionisation energies of H^o, He^o and He^+, respectively; and the function

$$c_i(T_i) = \left(\frac{T_{ROT}}{T_i}\right)^2 f(T_i) + \left(\frac{T_{VIB}}{T_i}\right)^2 \frac{\exp(T_{VIB}/T_i)}{[\exp(T_{VIB}/T_i)-1]^2}, \quad (4.34)$$

with $T_{ROT} = 85.4\,K$ and $T_{VIB} = 6100\,K$ accounts for the rotational and vibrational degrees of freedom of H_2.

Opacity

For the dust and gas opacity, Stamatellos et al (2007) use the parametrisation proposed by Bell & Lin (1994), i.e.

$$\kappa_R(\rho,T) = \kappa_P(\rho,T) = \kappa_0\rho^a T^b. \quad (4.35)$$

Here (κ_0, a, b) are constants which depend on the dominant physical process contributing to the opacity in different regimes of density and temperature. Fig. 4.2 shows how the

local Rosseland-mean opacity varies with density and temperature. At low temperatures the opacity is due to icy dust grains. As the temperature reaches $T \sim 150$ K, these icy dust grains evaporate and the opacity is dominated by metal grains up to $T \sim 1,000$ K. Between $T \sim 1,000$ K and $T \sim 2,000$ K the opacity drops considerably and is now mainly due to molecules. In this temperature range it is too hot for dust to exist and too cold for H^- to contribute. Above $T \sim 2,000$ K the opacity rises again due to H^- absorption, and then decreases above $T \sim 10^4$ K. At this stage free-free transitions dominate. At even higher temperatures, electron scattering dominates the opacity.

To calculate the pseudo-mean opacity used in Equation (4.21), the local Rosseland- and Plank-mean opacities in Equation (4.35) must be convolved with the polytropic density and temperature profiles according to Equation (4.20). The resultant pseudo-mean opacity is shown in Fig. 4.3.

This new method to treat the energy equation has been extensively tested by Stamatellos et al. (2007) and has shown to give a good fit to the computations of Masunaga & Inutsuka (2000), of a collapsing, non-rotating $1M_\odot$ protostar. It has also been tested against the analytic solutions of Spiegel (1957) and performs well in both the optically thin and optically thick regimes. The algorithm is very efficient, and computationally inexpensive since density, temperature and gravitational potential are already calculated using the standard SPH formalism. When compared with an otherwise identical simulation performed using our standard barotropic equation of state, a simulation performed with the new treatment of the energy equation requires at most 4% more CPU time.

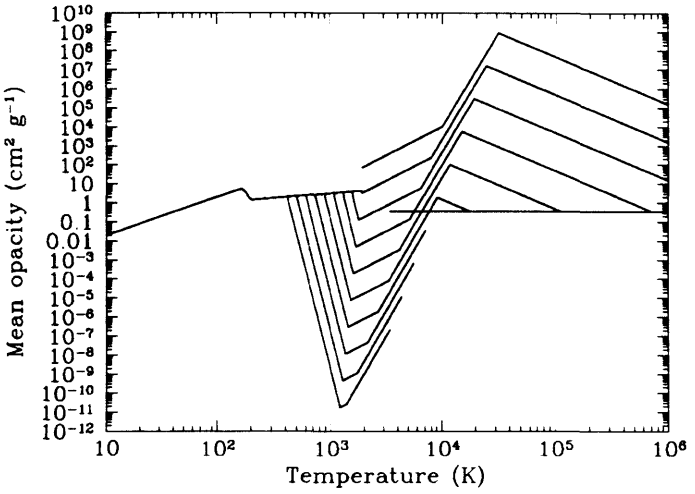

Figure 4.2: The variation of the *local Rosseland-mean opacity* with density and temperature. Isopycnic curves are plotted from $\rho = 10^{-18}$ g cm^{-3} to $\rho = 1$ g cm^{-3}, every two orders of magnitude (from bottom to top). The opacity gap is evident at temperatures $\sim$ 1,000 to 3,000 K, over a wide range of densities. Taken from Stamatellos et al. (2007).

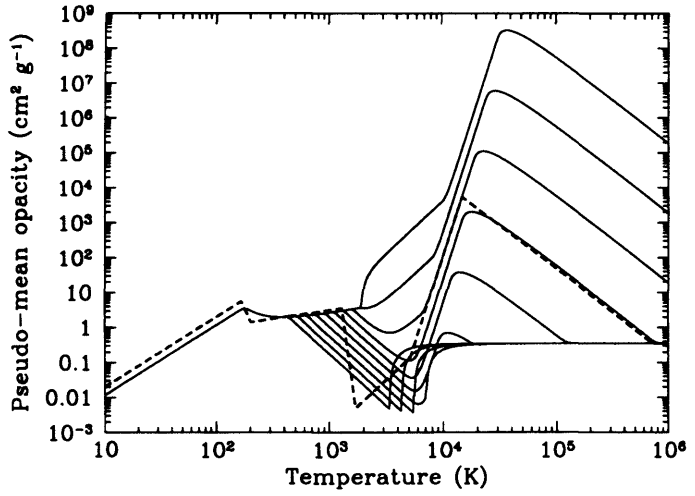

Figure 4.3: The variation with density and temperature of the *pseudo-mean opacity*. Isopycnic curves are plotted as in Fig. 4.2. For comparison the *local* opacity at density $\rho = 10^{-6}$ g cm^{-3} is also plotted (dashed line). Taken from Stamatellos et al. (2007).

4.3 Numerical Details

4.3.1 Setting up the cores

To produce the initial conditions described in Section 4.2 we start by placing a large number of particles randomly in a cube, which we then settle using DRAGON to give a relaxed uniform-density distribution. Next we cut out a sphere containing the number of particles that we require, in this case 25,000. Finally we stretch this uniform-density sphere radially to reproduce the Plummer-like density profile (Equation (4.4)).

4.3.2 Resolution

In computer simulations it is extremely important that there exists a suitable resolution, to ensure we properly resolve the physical processes that occur. The simulations in this study are performed with $N_{\rm TOT} = 25,000$ SPH particles. Hence the mass resolution is

$$M_{\rm MIN} \sim \frac{N_{\rm NEIB}\, M_{\rm TOT}}{N_{\rm TOT}} \sim 0.01\,{\rm M}_{\odot}. \tag{4.36}$$

Any structures with mass below this value are therefore not resolved. We use sink particles to identify the stars in our simulations (see Section 2.10 for a description of sinks). We adopt a sink density $\rho_{\rm SINK} = 10^{-11}\,{\rm g\,cm^{-3}}$ and a sink radius $R_{\rm SINK} = 5\,{\rm AU}$. Therefore, the minimum linear resolution is 5 AU. The discs which form in these simulations typically have radius $R_{\rm DISC} \sim 50\,{\rm AU}$ and half-thickness $Z_{\rm DISC} \sim 5\,{\rm AU}$, so they are only just resolved in the vertical direction. However, we do not believe that this compromises our results, since the fragmentation of a disc is essentially a two-dimensional process. The forces which drive the accumulation of matter into a protofragment are in the plane of the disc and so we do not need to resolve accurately the vertical direction. We note that this is a different view to some authors, in particular Nelson (2006), who argues that enhanced fragmentation is a direct consequence of failing to resolve a disc vertically.

Turbulent, self-gravitating gas dynamics is very chaotic in nature and so to make robust statistical inferences we require many realisations. Therefore, for each value of $\alpha_{\rm TURB}$ (= 0.05, 0.10, 0.25) we perform an ensemble of 20 simulations using the barotropic equation of state, and an ensemble of 20 simulations using the new treatment of the energy equation.

The 20 simulations in each set all have the same treatment of the thermodynamics (either the barotropic equation of state, or the new treatment of the energy equation) and the same initial level of turbulence; they are distinguished solely by having different realisations of the turbulent velocity field. We use a random-number seed to generate the initial turbulent velocity field. We evolve each simulation for 300 kyr.

4.4 Results and Discussion

Table 4.1 lists, for each simulation performed with the barotropic equation of state, the identifier (ID); the initial level of turbulence ($\alpha_{\rm TURB}$), the total mass which ends up in stars ($\sum\{M_\star\}/{\rm M}_\odot$), the total number of stars ($\mathcal{N}_\star$), and the total number of brown dwarfs ($\mathcal{N}_{\rm BD}$), at the end of the simulation; the types of multiple system that have formed; and the masses of the individual stars ($M_\star/{\rm M}_\odot$), with a superscript indicating which ones are components of multiple systems. Table 4.2 lists the same information for the simulations performed using the new treatment of the energy equation.

4.4.1 Efficiency and timing of star formation

Table 4.3 records – for each treatment of the thermodynamics and each initial level of turbulence – the number of different realisations ($\mathcal{N}_{\rm REAL}$), the efficiency (i.e. the mean fraction of the core mass converted into stars after 300 kyr, $\eta \equiv \sum\{M_\star\}/M_{\rm CORE}$), and the mean number of stars formed from one core ($\overline{\mathcal{N}_\star}$). With each treatment of the thermo-

Table 4.1: Results of the simulations performed using the barotropic equation of state with $\alpha_{\rm TURB}$ = 0.05, 0.10 and 0.25, at time t = 300 kyr. Column 1 gives the simulation identifier, column 2 gives $\alpha_{\rm TURB}$, column 3 gives the total mass of stars formed, $\sum\{M_\star\}/{\rm M}_\odot$, column 4 gives the total number of stars formed, $N_\star$, column 5 gives the total number of brown dwarfs formed, $N_{\rm BD}$, column 6 gives the order of any multiple systems formed, and column 7 gives the masses of individual stars, with a superscript to indicate those which are components of of binary systems ($M_\star^b$), triple systems ($M_\star^t$), or quadruple systems ($M_\star^q$).

ID	$\alpha_{\rm TURB}$	$\sum\{M_\star\}/{\rm M}_\odot$	$N_\star$	$N_{\rm BD}$	Mult	$M_\star/{\rm M}_\odot$
N071	0.05	3.731	4	0	T	1.297^t, 0.970, 0.749^t, 0.715^t
N072	0.05	3.867	5	0	T	1.638^t, 1.204^t, 0.472^t, 0.285, 0.268
N073	0.05	3.282	5	0	B	1.216^b, 1.111^b, 0.386, 0.186, 0.383
N074	0.05	4.001	7	3	Q	1.174^q, 1.106^q, 0.811^q, 0.806^q, 0.049, 0.031, 0.024
N075	0.05	3.307	4	0	T	0.956^t, 0.911^t, 0.728^t, 0.712
N076	0.05	3.915	7	2	Q	1.001^q, 0.914^q, 0.694, 0.593^q, 0.583^q, 0.088, 0.042
N077	0.05	3.646	1	0	S	3.646
N078	0.05	3.814	6	0	T	0.998^t, 0.892^t, 0.854^t, 0.763, 0.199, 0.108
N079	0.05	3.959	3	0	T	2.319^t, 0.823^t, 0.817^t
N080	0.05	3.700	1	0	S	3.700
N081	0.05	3.690	1	0	S	3.690
N082	0.05	3.928	5	2	T	1.322^t, 1.286^t, 1.214^t, 0.070, 0.036
N083	0.05	3.905	2	0	B	2.459^b, 1.446^b
N084	0.05	3.987	2	0	B	3.056^b, 0.931^b
N085	0.05	3.911	2	0	B	2.151^b, 1.760^b
N086	0.05	3.774	6	1	Q	1.037^q, 1.007^q, 0.741^q, 0.732^q, 0.219, 0.038
N087	0.05	3.404	1	0	S	3.404
N088	0.05	3.874	1	0	S	3.874
N089	0.05	3.491	5	0	B	1.005^b, 0.934^b, 0.695, 0.693, 0.164
N090	0.05	3.778	1	0	S	3.778
N001	0.10	3.570	5	0	Q	1.021^q, 0.946^q, 0.772^q, 0.715^q, 0.116
N002	0.10	3.529	10	2	Q	1.999^q, 0.366^q, 0.287^q, 0.285^q, 0.203, 0.122, 0.100, 0.083, 0.055, 0.029
N003	0.10	3.596	1	0	S	3.596
N004	0.10	3.455	1	0	S	3.455
N005	0.10	3.342	6	1	T	1.253^t, 0.813^t, 0.674^t, 0.400, 0.160, 0.042
N006	0.10	3.596	1	0	S	3.596
N007	0.10	3.519	6	1	Q	1.630^q, 0.675^q, 0.622^q, 0.479^q, 0.082, 0.031
N008	0.10	3.679	2	0	B	2.449^b, 1.230^b
N009	0.10	3.497	1	0	S	3.497
N010	0.10	3.479	4	0	Q	1.029^q, 1.014^q, 0.725^q, 0.711^q
N011	0.10	3.742	3	0	T	1.519^t, 1.142^t, 1.081^t
N012	0.10	3.785	4	0	Q	1.572^q, 0.881^q, 0.881^q, 0.451^q
N013	0.10	3.286	9	2	TT	0.597, 0.593^{t1}, 0.541^{t1}, 0.415^{t1}, 0.371, 0.368^{t2}, 0.365^{t2}, 0.029, 0.007^{t2}
N014	0.10	2.962	6	1	T	0.919^t, 0.885^t, 0.545^t, 0.361, 0.174, 0.078
N015	0.10	3.696	4	0	Q	2.815^q, 0.296^q, 0.295^q, 0.290^q
N016	0.10	3.533	1	0	S	3.553
N017	0.10	3.741	6	1	Q	1.385^q, 0.989^q, 0.599^q, 0.592^q, 0.103, 0.073
N018	0.10	3.726	2	0	B	2.199^b, 1.527^b
N019	0.10	3.692	5	0	T	1.108^t, 1.098^t, 1.003^t, 0.310, 0.173
N020	0.10	3.602	6	2	T	1.378^t, 0.952^t, 0.991^t, 0.226, 0.078, 0.057
N041	0.25	3.225	5	0	T	0.788^t, 0.787^t, 0.712^t, 0.623, 0.315
N042	0.25	3.209	6	1	Q	2.024^q, 0.329^q, 0.313^q, 0.302^q, 0.164, 0.077
N043	0.25	3.312	4	0	Q	1.103^q, 0.825^q, 0.694^q, 0.690^q
N044	0.25	3.402	5	0	T	1.560^t, 0.544^t, 0.502, 0.465^t, 0.331
N045	0.25	3.272	7	1	TT	0.583^{t1}, 0.578^{t1}, 0.571^{t1}, 0.539^{t2}, 0.531^{t2}, 0.409^{t2}, 0.061
N046	0.25	3.138	2	0	B	1.642^b, 1.496^b
N047	0.25	3.442	5	0	BT	0.927^b, 0.861^t, 0.590^t, 0.581^t, 0.483^b
N048	0.25	2.852	6	1	T	1.055, 0.594^t, 0.469^t, 0.377,0.323^t, 0.034
N049	0.25	3.271	5	0	Q	2.001^q, 0.398^q, 0.396^q, 0.381^q, 0.095
N050	0.25	3.291	5	0	Q	1.006^q, 0.948^q, 0.616^q, 0.609^q, 0.112
N051	0.25	3.716	4	0	Q	1.094^q, 1.046^q, 0.796^q. 0.780^q
N052	0.25	3.843	3	0	T	2.184^t, 0.834^t, 0.825^t
N053	0.25	3.943	5	0	Q	1.254^q, 1.048^q, 0.752^q, 0.748^q, 0.141
N054	0.25	3.772	6	2	Q	1.126^q, 1.010^q, 0.784^q, 0.783^q, 0.040, 0.029
N055	0.25	3.762	5	0	T	1.074^t, 0.957, 0.819^t, 0.800^t, 0.112
N056	0.25	3.857	5	1	T	1.426^t, 1.231^t, 1.059^t, 0.105, 0.036
N057	0.25	3.007	5	0	Q	0.903^q, 0.838^q, 0.543^q, 0.541^q, 0.182
N058	0.25	3.769	6	0	T	1.155^t, 1.031^t, 0.757^t, 0.374, 0.360, 0.092
N059	0.25	3.723	6	1	Q	1.249^q, 1.057^q, 0.642^q, 0.638^q, 0.109, 0.028
N060	0.25	3.866	6	2	Q	1.169^q, 0.956^q, 0.907^q, 0.782^q, 0.046, 0.006

Table 4.2: Results of the simulations using the new treatment of the energy equation. Columns follow the same labelling as Table 4.1.

ID	α_{TURB}	$\Sigma\{M_*\}/M_\odot$	N_*	N_{BD}	Mult	$M_*/M_\odot$
T071	0.05	3.161	8	3	B	0.825^b, 0.810^b, 0.622, 0.494, 0.346, 0.029, 0.020, 0.015
T072	0.05	2.212	6	1	BT	0.750^b, 0.603^b, 0.281^t, 0.279^t, 0.275^t, 0.024
T073	0.05	3.200	5	1	B	0.877^b, 0.870^b, 0.696, 0.678, 0.079
T074	0.05	3.561	13	6	BT	0.830^b, 0.828^b, 0.439^t, 0.432^t, 0.427^t, 0.328, 0.154, 0.039, 0.034, 0.023, 0.013, 0.007 0.007
T075	0.05	3.252	7	2	BB	0.753^{b1}, 0.748^{b1}, 0.599^{b2}, 0.553, 0.546^{b2}, 0.032, 0.021
T076	0.05	3.918	9	5	Q	1.118^q, 1.104^q, 0.722^q, 0.715^q, 0.079, 0.070, 0.056, 0.029, 0.025
T077	0.05	3.884	7	3	B	1.338^b, 1.149^b, 0.702, 0.635, 0.032, 0.017, 0.011
T078	0.05	3.559	12	3	T	0.679, 0.678^t, 0.505^t, 0.478^t, 0.435, 0.261, 0.191, 0.168, 0.087, 0.040, 0.023, 0.014
T079	0.05	3.410	10	1	T	0.733^t, 0.722, 0.487^t, 0.481^t, 0.461, 0.186, 0.139, 0.095, 0.088, 0.018
T080	0.05	3.894	4	1	B	1.480^b, 1.237, 1.159^b, 0.018
T081	0.05	3.613	5	1	B	1.158^b, 1.059^b, 0.686, 0.645, 0.065
T082	0.05	3.741	7	2	T	0.907, 0.884^t, 0.758^t, 0.754^t, 0.399, 0.026, 0.013
T083	0.05	3.739	5	1	B	0.999, 0.983^b, 0.912^b, 0.815, 0.030
T084	0.05	3.868	8	3	B	1.219^b, 1.191^b, 1.123, 0.139, 0.092, 0.051, 0.031, 0.022
T085	0.05	3.749	7	2	B	0.882^b, 0.850, 0.832, 0.804^b, 0.332, 0.026, 0.023
T086	0.05	3.898	6	1	Q	0.863^q, 0.850^q, 0.849^q, 0.840^q, 0.460, 0.036
T087	0.05	3.434	1	0	S	3.434
T088	0.05	3.381	8	3	BB	1.435^{b1}, 1.073^{b1}, 0.332^{b2}, 0.320^{b2}, 0.164, 0.021, 0.019, 0.017
T089	0.05	3.259	9	2	B	0.645^b, 0.617^b, 0.612, 0.542, 0.342, 0.314, 0.146, 0.022, 0.019
T090	0.05	3.811	7	2	T	2.100^t, 1.032^t, 0.248^t, 0.187, 0.122, 0.058, 0.034
T001	0.10	3.434	6	0	T	0.642^t, 0.622^t, 0.607, 0.572^t, 0.528, 0.463
T002	0.10	3.245	10	4	Q	1.064^q, 0.891^q, 0.340^q, 0.339^q, 0.336, 0.156, 0.078, 0.019, 0.012, 0.010
T003	0.10	3.698	1	0	S	3.698
T004	0.10	3.481	1	0	S	3.481
T005	0.10	3.551	4	0	T	1.482^t, 0.845^t, 0.824^t, 0.400
T006	0.10	3.456	4	0	B	0.958, 0.919^b, 0.819^b, 0.760
T007	0.10	2.790	11	5	BT	0.719^b, 0.659^b, 0.421, 0.375, 0.248^t, 0.247^t, 0.060, 0.035, 0.011, 0.009^t, 0.006
T008	0.10	3.549	3	0	T	1.392^t, 1.108^t, 1.049^t
T009	0.10	3.509	1	0	S	3.509
T010	0.10	3.270	8	2	Q	0.748^q, 0.620^q, 0.494^q, 0.485^q, 0.445, 0.408, 0.052, 0.018
T011	0.10	3.287	6	0	B	0.770^b, 0.757^b, 0.616, 0.526, 0.512, 0.106
T012	0.10	3.771	7	1	BT	0.702^t, 0.686, 0.669^t, 0.664^t, 0.532^b, 0.501^b, 0.017
T013	0.10	3.761	12	6	Q	0.791^q, 0.785^q, 0.602^q, 0.553^q, 0.460, 0.353, 0.055, 0.041, 0.039, 0.033, 0.029, 0.020
T014	0.10	3.422	7	3	B	0.966^b, 0.966^b, 0.681, 0.666, 0.055, 0.051, 0.037
T015	0.10	3.552	5	2	T	1.286^t, 1.205^t, 0.918^t, 0.075, 0.068
T016	0.10	3.115	6	1	B	0.989, 0.959^b, 0.411^b, 0.391, 0.387, 0.018
T017	0.10	3.779	5	0	T	1.190^t, 0.837^t, 0.826^t, 0.467, 0.459
T018	0.10	3.524	12	6	T	0.914^t, 0.869^t, 0.488, 0.466^t, 0.464, 0.194, 0.050, 0.032, 0.024, 0.009, 0.008, 0.006
T019	0.10	3.802	4	0	Q	0.974^q, 0.968^q, 0.933^q, 0.927^q
T020	0.10	3.054	11	4	BT	0.666^t, 0.664^t, 0.654^b, 0.324^t, 0.239, 0.225, 0.136, 0.074, 0.044, 0.016, 0.012^b
T041	0.25	3.369	7	2	BT	0.821^t, 0.809^t, 0.782^b, 0.778^b, 0.138^t, 0.025, 0.016
T042	0.25	3.055	4	0	T	1.083^t, 0.932^t, 0.913^t, 0.127
T043	0.25	3.306	9	3	BT	0.798^t, 0.586^b, 0.585^b, 0.494^t, 0.488^t, 0.271, 0.039, 0.033, 0.012
T044	0.25	3.260	14	8	BB	0.763^{b1}, 0.762^{b1}, 0.462^{b2}, 0.450^{b2}, 0.426, 0.235, 0.054, 0.032, 0.025, 0.016, 0.010, 0.009, 0.008, 0.008
T045	0.25	3.193	13	4	QT	0.444^q, 0.438^q, 0.379^t, 0.378^t, 0.368^t, 0.342^q, 0.340^q, 0.332, 0.081, 0.034, 0.031, 0.018, 0.008
T046	0.25	3.362	5	0	T	0.853, 0.768^t, 0.768^t, 0.573^t, 0.400
T047	0.25	3.024	12	5	BT	0.591^b, 0.591^b, 0.411^t, 0.404^t, 0.403^t, 0.327, 0.110, 0.067, 0.057, 0.033, 0.019, 0.011
T048	0.25	3.509	11	4	TT	0.653^{t1}, 0.614^{t2}, 0.606^{t2}, 0.509^{t1},0.506^{t1}, 0.372^{t2}, 0.155, 0.040, 0.023, 0.023, 0.008
T049	0.25	2.466	6	1	T	0.679^t, 0.678^t, 0.455^t, 0.316, 0.312, 0.026
T050	0.25	3.010	8	1	BT	0.729^b, 0.697^b, 0.325^t, 0.319^t, 0.317^t, 0.307, 0.282, 0.034
T051	0.25	2.669	10	2	BB	0.654^{b1}, 0.526^{b1}, 0.440^{b2}, 0.323, 0.274^{b2}, 0.160, 0.129, 0.092, 0.048, 0.023
T052	0.25	3.717	13	6	Q	0.859^q, 0.856^q, 0.442^q, 0.439^q, 0.321, 0.318, 0.271, 0.057, 0.046, 0.037, 0.029, 0.024, 0.018
T053	0.25	3.343	12	5	T	0.762^t, 0.687^t, 0.660, 0.385, 0.285, 0.267, 0.161, 0.044, 0.036, 0.026, 0.016, 0.014^t
T054	0.25	3.506	12	5	B	0.779^b, 0.592^b, 0.504, 0.466, 0.350, 0.334, 0.315, 0.073, 0.027, 0.026, 0.022, 0.018
T055	0.25	3.791	6	1	Q	0.935^q, 0.924^q, 0.850^q, 0.847^q, 0.182, 0.053
T056	0.25	3.841	6	1	Q	1.111^q, 1.051^q, 0.563^q, 0.552^q, 0.531, 0.033
T057	0.25	3.712	4	0	Q	1.183^q, 0.913^q, 0.813^q, 0.803^q
T058	0.25	3.758	11	4	B	0.985, 0.966^b, 0.547^b, 0.457, 0.452, 0.105, 0.084, 0.059, 0.052, 0.032, 0.019
T059	0.25	3.510	10	2	BBT	0.847^{b1}, 0.786^{b1}, 0.663, 0.298^t, 0.296^t, 0.289^t, 0.127^{b2}, 0.122,^{b2} 0.078, 0.014
T060	0.25	3.882	8	3	T	1.155, 0.930^t, 0.885^t, 0.426^t, 0.418, 0.031, 0.023, 0.014

Table 4.3: For each treatment of the thermodynamics (barotropic equation of state or new treatment of the energy equation) and each value of the initial level of turbulence ($\alpha_{\rm TURB}$), we record the number of different realisations simulated ($\mathcal{N}_{\rm REAL}$), the efficiency (i.e. mean fraction of the core mass converted into protostars, $\eta \equiv \sum\{M_\star\}/M_{\rm CORE}$), the mean number of stars formed from a single core ($\overline{\mathcal{N}_\star}$), the numbers of singles (S), binaries (B), triples (T) and quadruples (Q), the multiplicity frequence (**mf**), the companion probability (**cp**), and the companion frequency (**cf**).

THERMODYNAMICS	$\alpha_{\rm TURB}$	$\mathcal{N}_{\rm REAL}$	η	$\overline{\mathcal{N}_\star}$	S	B	T	Q	**mf**	**cp**	**cf**
BAROTROPIC	0.05	20	0.694	3.45	29	5	6	3	0.33	0.58	1.19
	0.10	20	0.658	4.15	30	2	7	7	0.35	0.64	1.57
	0.25	20	0.600	5.05	27	2	10	10	0.46	0.73	1.82
NEW TREATMENT	0.05	20	0.605	7.20	88	15	6	2	0.21	0.39	0.63
	0.10	20	0.629	6.20	67	7	9	4	0.23	0.46	0.94
	0.25	20	0.623	9.05	98	12	13	5	0.23	0.46	0.90

dynamics, increasing the initial level of turbulence has the following effects.

Using a barotropic equation of state

Using a barotropic equation of state, increasing the level of turbulence (a) decreases the efficiency of star formation, η, and (b) increases the mean number of stars formed from a single core, $\overline{\mathcal{N}_\star}$.

- *Efficiency of star formation is reduced*

  Increasing the initial level of turbulence reduces the efficiency because the outer, more diffuse parts of the core become more vigorously dispersed. At the end of the simulation (300 kyr) these diffuse regions have not yet had time to fall back into the core and be incorporated into stars, and so the fraction of the core mass incorporated into stars is lowered.

- *Mean number of stars formed from a single core increases*

  An increased initial level of turbulence increases the total number of stars formed from a single core, because it drives more vigorous local compression in the core. This results in regions becoming dense enough to be gravitationally unstable i.e. the creation of more protostellar seeds.

Using the new treatment of the energy equation

If the initial level of turbulence is increased, the monotonic trend seen when using a barotropic equation of state disappears with the implementation of the new treatment of the energy equation. The efficiency, and the mean number of stars formed from a single core, are only weakly dependent on the initial level of turbulence.

Differences between using the two treatments of the thermodynamics

Switching from the barotropic equation of state to the new treatment of the energy equation reduces the efficiency, η, somewhat, and significantly increases the mean number of stars formed from a single core, $\overline{N}_\star$. There are two physical effects at work here.

First, the new treatment of the energy equation promotes the condensation of very low-mass stars, by taking proper account of the thermal history and environment of the gas. With the new treatment of the energy equation, a small proto-fragment tends to be cooler, and thereby more inclined to condense out. This is because the new treatment takes account of the fact that, being of lower mass (and probably also non-spherical), the column-density inhibiting the cooling of a low-mass proto-fragment is lower; and because it contracts more slowly, its heating rate is lower. Consequently its temperature is lower – at a given density – than the one prescribed by the barotropic equation of state, since the latter is based on the behaviour at the centre of a collapsing, spherical, non-rotating $1\,M_\odot$ protostar. This is illustrated in Fig. 4.4, which shows exactly the same initial conditions, evolved first with the barotropic equation of state (top frames), and then with the new treatment of the energy equation (bottom frames). It is evident that disc fragmentation is far more advanced in the simulation using the new treatment of the energy equation.

Secondly, because the stars formed are of lower mass, they are less effective at mopping up the residual gas in the core, which in turn would increase their mass. This

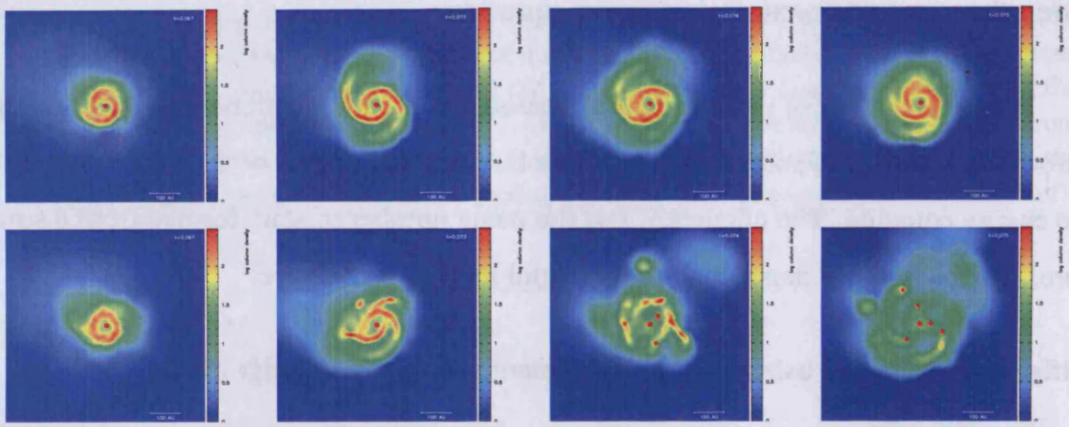

Figure 4.4: Simulation of the collapse and fragmentation of a 5.4 $M_{\odot}$ core, first evolved with the barotropic equation of state (top row) and then with the new treatment of the energy equation (bottom row), using identical initial conditions. Each snapshot shows the logarithm of the column density.

means they remain small, and so are more likely to be ejected by dynamical interactions with other stars. Hence the amount of mass converted into stars is somewhat reduced, and the efficiency is lower.

4.4.2 Fragmentation

There is a common pattern of star formation in many of these simulations, irrespective of the treatment of thermodynamics. The low angular momentum material in the core collapses quickly to form the first star – hereafter the *primary* – on a timescale of 50 to 70 kyr, i.e. a bit longer than the initial freefall time at the centre of the core, which is $\sim$ 40 kyr. Then material with higher angular momentum forms a circumstellar disc around the primary. This circumprimary disc grows in mass – the rate of infall onto the disc is greater than the rate at which mass accretes from the inner disc onto the primary – until the disc becomes Toomre unstable and fragments to form multiple secondaries. The delay between the formation of the primary and fragmentation of the circumprimary disc is typically between 10 and 100 kyr. During this time the disc is accumulating mass. Once the disc becomes Toomre unstable it normally fragments to produce between 3 and

Table 4.4: For each treatment of the thermodynamics (barotropic equation of state or new treatment of the energy equation) we record the mean, μ, and the standard deviation, σ, of the delay times t_1, $(t_2 - t_1)$ and $(t_3 - t_2)$.

THERMODYNAMICS	DELAY TIME	μ	σ
BAROTROPIC	t_1	62.3	6.3
	$(t_2 - t_1)$	29.8	24.3
	$(t_3 - t_2)$	2.0	1.7
NEW TREATMENT	t_1	60.6	6.0
	$(t_2 - t_1)$	11.4	9.3
	$(t_3 - t_2)$	1.3	1.0

5 stars, in the space of a few kyr.

This pattern of fragmentation is illustrated on Figs. 4.5 and 4.6, where, for a selection of simulations, we plot stellar masses as a function of time. On most of these plots, we see the primary forming, then a delay whilst the circumprimary disc builds up, and finally – when the circumprimary disc becomes Toomre unstable – the formation of a clutch of secondaries. Some of these secondaries are quickly ejected, and therefore end up as brown dwarfs, but others remain in the disc and accrete sufficient mass to become hydrogen-burning stars. Occasionally some even grow bigger than the primary.

In Fig. 4.7, for each treatment of the thermodynamics, we show the distributions of t_1 (the time of formation of the first star); $t_2 - t_1$ (the delay between the formation of the first and second stars); and $t_3 - t_2$ (the delay between the formation of the second and third stars). The mean and standard deviation of these values are shown in Table 4.4.

t_1 is the time it takes the low angular momentum material to assemble into the first stars and should be compared with the freefall time at the centre of the core ($\sim$ 40 kyr). It takes slightly longer for the first stars to form when using a barotropic equation of state compared to when using the new treatment of the energy equation.

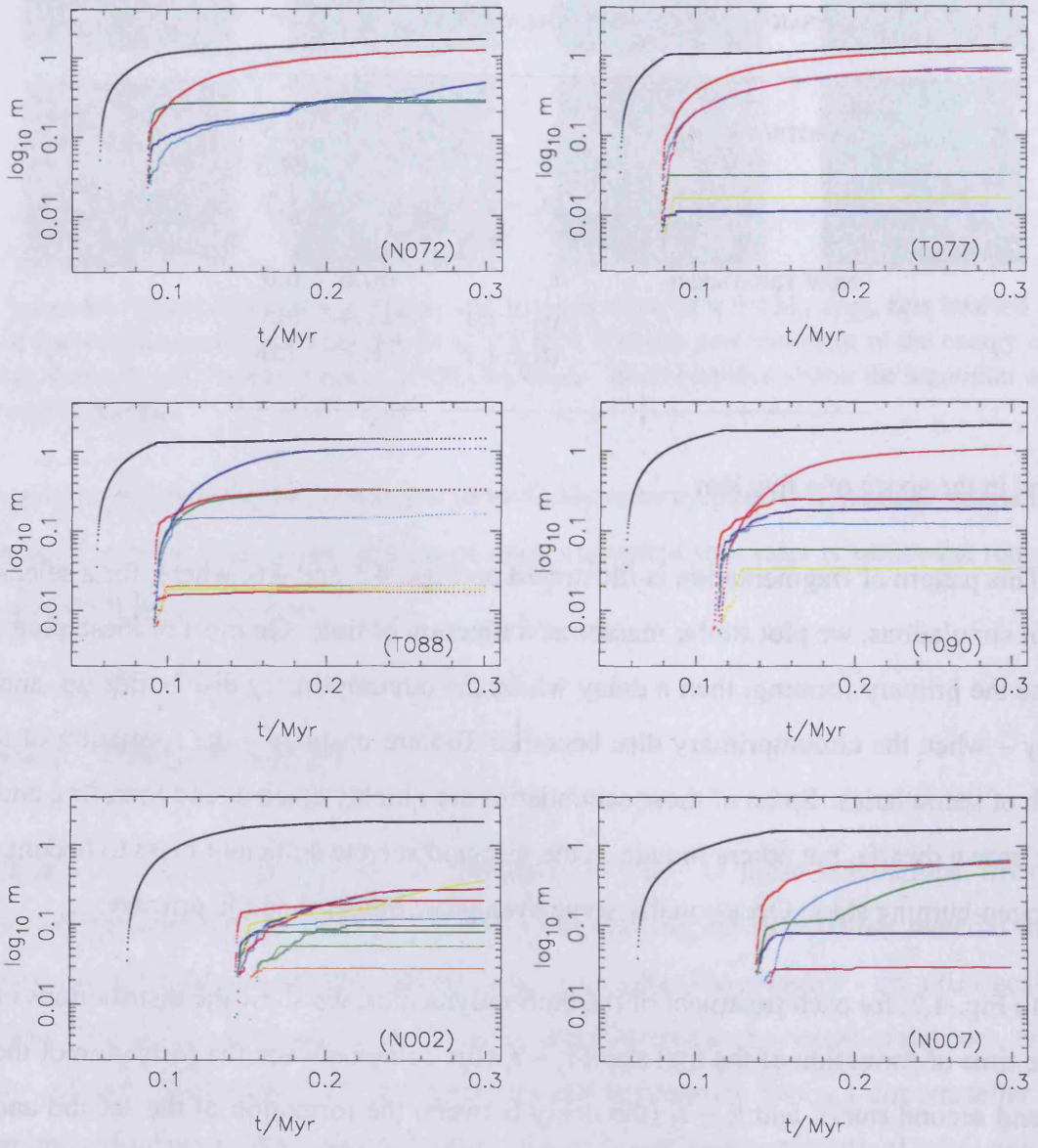

Figure 4.5: Stellar masses as a function of time, for a selection of simulations. Note (i) the delay between the formation of the primary and the formation of a clutch of secondaries (this is the time during which the circumprimary disc accumulates, until it becomes Toomre unstable); and (ii) the rapid decline in the accretion rate onto the primary once the secondaries start to condense out.

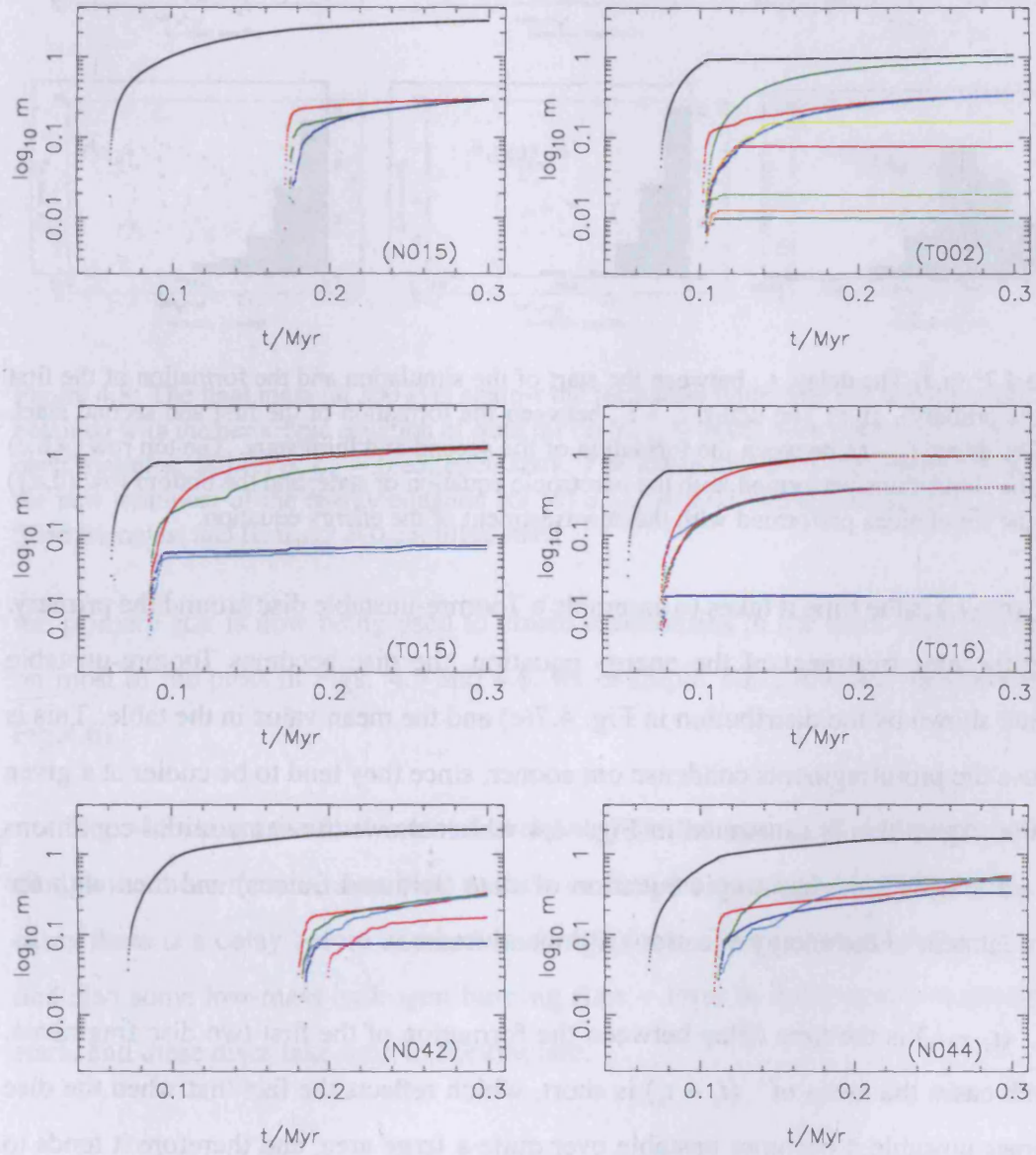

Figure 4.6: Stellar masses as a function of time, for a selection of simulations.

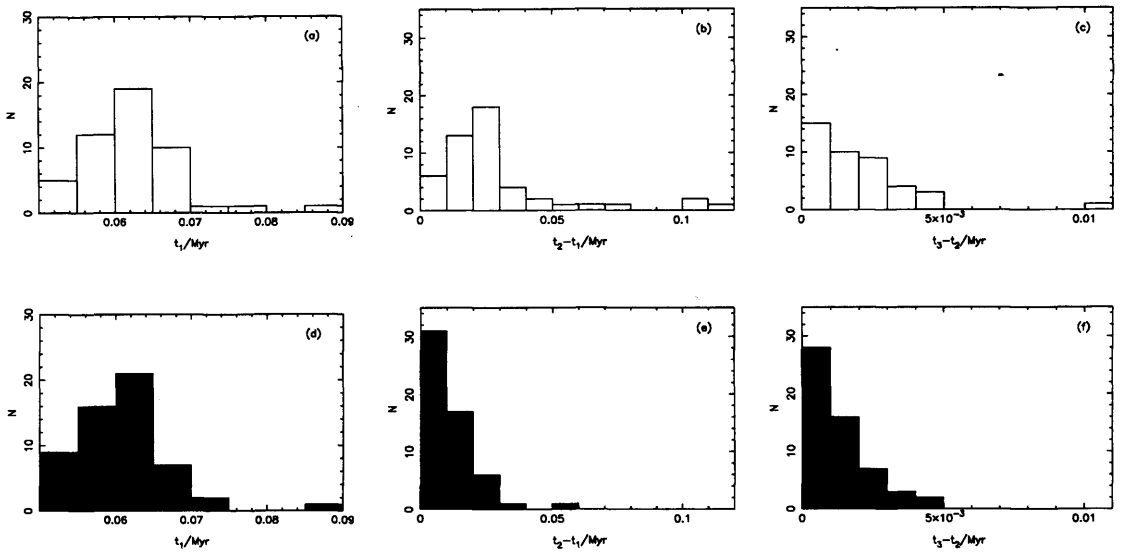

Figure 4.7: (a,d) The delay, t_1, between the start of the simulation and the formation of the first star (the primary). (b,e) The delay, $t_2 - t_1$, between the formation of the first and second stars. (c,f) The delay, $t_3 - t_2$, between the formation of the second and third stars. The top row (a,b,c) is for the simulations performed with the barotropic equation of state, and the bottom row (d,e,f) is for the simulations performed with the new treatment of the energy equation.

$(t_2 - t_1)$ is the time it takes to assemble a Toomre-unstable disc around the primary. Using the new treatment of the energy equation, the disc becomes Toomre-unstable quicker, shown by the distribution in Fig. 4.7(e) and the mean value in the table. This is because the protofragments condense out sooner, since they tend to be cooler at a given density. Again this is illustrated in Fig. 4.4 which shows the same initial conditions evolved first with the barotropic equation of state (lefthand frames) and then with the new treatment of the energy equation (righthand frames).

$(t_3 - t_2)$ is the time delay between the formation of the first two disc fragments. In both cases the mean of $(t_3 - t_2)$ is short, which reflects the fact that when the disc becomes unstable it becomes unstable over quite a large area, and therefore it tends to spawn several stars in quick succession.

Another common feature of the accretion histories is that when the circumprimary disc becomes Toomre unstable and fragments, the accretion rate onto the primary declines rapidly. Material which up until this juncture had been spiraling inwards and onto

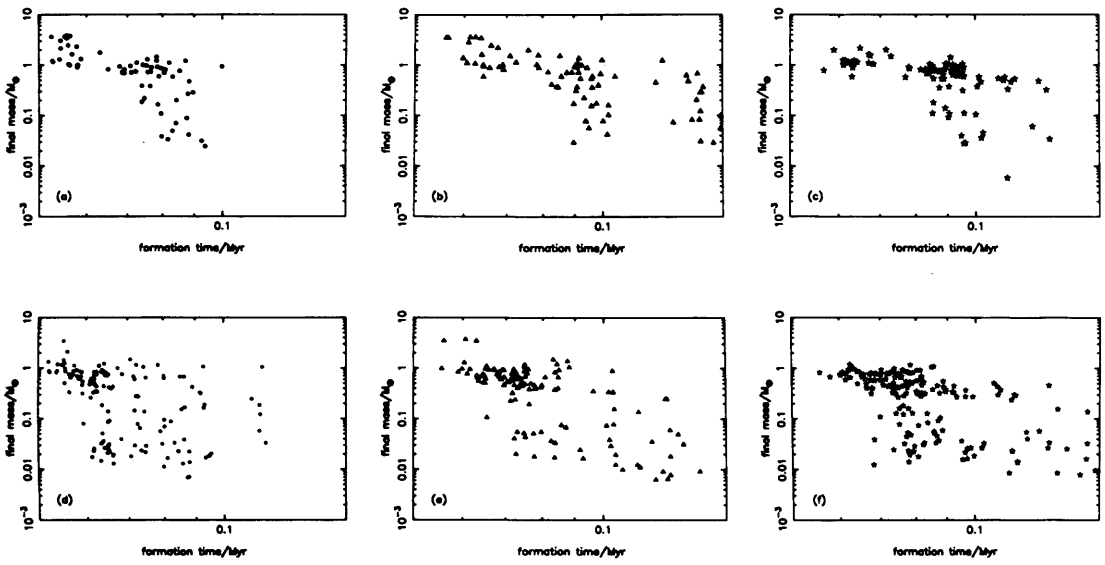

Figure 4.8: The final mass (at 300 kyr) against the formation time. The top row gives the results obtained with the barotropic equation of state for (a) $\alpha_{\rm TURB}$ = 0.05, open circles; (b) $\alpha_{\rm TURB}$ = 0.10, open triangles; and (c) $\alpha_{\rm TURB}$ = 0.25, open stars. The lower row gives the results obtained with the new treatment of the energy equation for (d) $\alpha_{\rm TURB}$ = 0.05, filled circles; (e) $\alpha_{\rm TURB}$ = 0.10, filled triangles; and (f) $\alpha_{\rm TURB}$ = 0.25, filled stars.

the primary star is now being used to create secondaries in the disc. This can be seen on most of the plots in Figs. 4.5 and 4.6, for example T002 (the top righthand plot in Fig.4.6).

Fig. 4.8 shows the final mass of every star plotted against its formation time. Although the more massive stars tend to form earlier, the correlation is fairly weak. In all cases there is a delay before any brown dwarfs form. This is because brown dwarfs – and also some low-mass hydrogen-burning stars – form in discs around more massive stars, and these discs take time to accumulate.

4.4.3 The mass distribution of protostars

Material which is parked in a circumprimary disc has time to lose entropy – to an extent that material which is compressed impulsively by turbulence does not. Consequently the masses of disc fragments are low, as predicted by Whitworth & Stamatellos (2006),

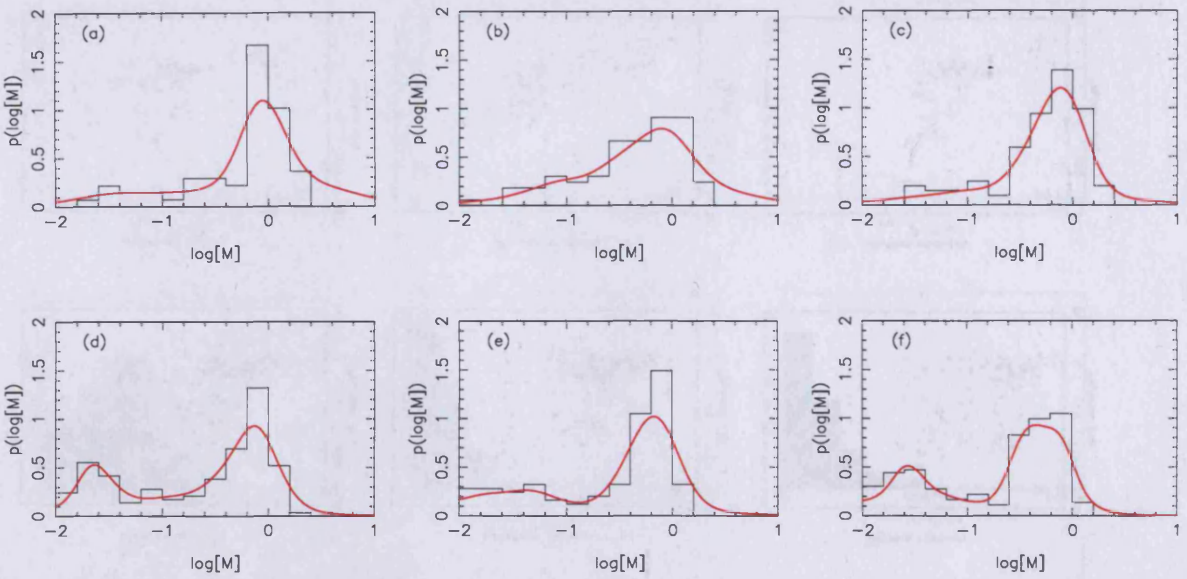

Figure 4.9: Normalised stellar mass distributions. The top row gives the mass distributions obtained with the barotropic equation of state for (a) $\alpha_{\rm TURB} = 0.05$, (b) $\alpha_{\rm TURB} = 0.10$, and (c) $\alpha_{\rm TURB} = 0.25$. The lower row gives the mass distributions obtained with the new treatment of the energy equation for (d) $\alpha_{\rm TURB} = 0.05$, (e) $\alpha_{\rm TURB} = 0.10$, and (f) $\alpha_{\rm TURB} = 0.25$. The black lines are histograms of the raw data, obtained using 15 equal logarithmic bins in the interval $-2 \leq \log_{10}(M_\star/{\rm M}_\odot) \leq +1$, and the red lines are obtained by smoothing each protostellar mass with a Gaussian whose width is proportional to the separation between neighbouring masses.

and demonstrated by detailed numerical simulations in Stamatellos et al. (2007b) and Stamatellos & Whitworth (2008a,b). However, this effect can only be captured with the new treatment of the energy equation, since this treatment takes account of the slow rate of compressional heating for matter parked in the disc, and the relatively low local column-densities through which its cooling radiation has to diffuse. In contrast, the barotropic equation of state presumes that the matter is part of a spherical 1 $M_\odot$ protostar, which by virtue of collapsing more rapidly is heated more vigorously, and has to cool through a larger column-density; therefore, at a given density, it is hotter and fragments less readily (i.e. into more massive fragments, if at all).

The lower masses and greater numbers of stars formed with the new treatment of the energy equation predisposes the stars to mutual dynamical interactions which eject many of them before they have time to grow much by accretion. Fig. 4.9 shows the mass

distributions obtained with the different combinations of thermodynamic treatment and initial level of turbulence. The black line shows the histogram obtained by distributing the final stellar masses into 15 logarithmic bins which are equally spaced in the interval

$$-2 \leq \log_{10}\left(\frac{M_\star}{\mathrm{M}_\odot}\right) \leq 1 .$$

The red line shows the mass distribution obtained when each stellar mass is smoothed using a Gaussian smoothing kernel with adaptive smoothing lengths dictated by the separation between masses [1] . Both the histogram, and the smoothed distribution, are normalised, in the sense that

$$\int_{M=0}^{M=\infty} p_{\log_{10}(M)}\, d\log_{10}(M) \;=\; 1 . \tag{4.39}$$

From Fig. 4.9 we see that the initial level of turbulence has little influence on the form of the mass distribution.

However, switching from the barotropic equation of state to the new treatment of the energy equation not only increases the proportion of brown-dwarf stars formed, but actually produces a bimodal mass distribution. The larger mode comprises hydrogen-burning stars with masses concentrated in the range 0.3 to $1.0\,\mathrm{M}_\odot$, whilst the smaller mode comprises brown dwarf stars with masses concentrated in the range 0.02 to $0.06\,\mathrm{M}_\odot$. This smaller mode represents very low-mass stars formed by disc fragmentation (due to the enhanced cooling which low-mass fragments enjoy with the new treatment of the

[1] The smoothed mass distributions are given by a sum of Gaussians,

$$p_\mu\, d\mu \;=\; \sum_{i=1}^{i=I} \left\{ \frac{1}{(2\pi)^{1/2}\,\sigma_i} \exp\left[\frac{-(\mu-\mu_i)^2}{2\,\sigma_i^2} \right] \right\} \frac{d\mu}{I} , \tag{4.37}$$

$$\sigma_i^2 \;=\; \left(\frac{\mu_I - \mu_1}{I-1}\right)^2 + \left(\frac{\mu_{i+2} - \mu_{i-2}}{4}\right)^2 , \tag{4.38}$$

where $\mu \equiv \log_{10}(M)$ and $\mu_i \equiv \log_{10}(M_i)$. The standard deviation σ_i is evaluated by adding – in quadrature – the mean separation between all masses across the entire mass spectrum (this is the first term on the righthand side of Equation 4.38), and the mean separation between the five nearest masses (this is the second term on the righthand side of Equation 4.38). Thus σ_i combines a global and a local contribution to the smoothing. This smoothing is essentially *ad hoc*, and is designed purely to enable us to extract the large-scale features of the mass distribution, which are otherwise lost in the rather noisy histograms.

energy equation) and then ejected by mutual interactions (before they can grow much by accretion).

However, we should not necessarily expect this bimodality to be reflected in the overall Stellar Initial Mass Function. We have only modelled a single core mass and a single density profile. For different core masses and/or different density profiles, the trough between the two peaks is likely to move to different masses, and may even disappear altogether. The overall Stellar Initial Mass Function will have contributions from an ensemble of cores with a range of masses and density profiles, and the bimodality is likely to be washed out.

4.4.4 Multiplicity statistics

There appears to be some confusion in the literature over the correct terminology when discussing the statistics of stellar multiplicity. To eliminate this confusion, Reipurth & Zinnecker (1993) introduced various definitions. Their nomenclature is adopted by Goodwin et al. (2004b) and we follow the same nomenclature here.

Firstly we define a "system" to include single stars, and a "multiple system" to only include systems containing more than one star. If S is the number of single stars, B the number of binaries, T the number of triples, and Q the number of quadruples, etc., then the total number of stars is $(S+2B+3T+4Q+...)$. Similarly, the total number of systems is $(S+B+T+Q+...)$ and the total number of multiple systems is $(B+T+Q+...)$.

The multiplicity frequency measures the fraction of systems which are multiple, i.e.

$$\mathbf{mf} = \frac{B+T+Q+...}{S+B+T+Q+...}. \tag{4.40}$$

The companion probability, **cp**, measures the fraction of stars which are in multiple

systems, i.e.

$$\mathbf{cp} = \frac{2B + 3T + 4Q + ...}{S + 2B + 3T + 4Q + ...}. \tag{4.41}$$

The companion frequency, from Goodwin et al. (2004b), measures the mean number of companions which a star has (irrespective of whether it is a primary), i.e.

$$\mathbf{cf} = \frac{2B + 6T + 12Q + ...}{S + 2B + 3T + 4Q + ...}. \tag{4.42}$$

In Table 4.3 we record — for each ensemble of 20 simulations, representing a particular combination of thermodynamic treatment and initial level of turbulence — the total numbers of singles (S), binaries (B), triples (T) and quadruples (Q) formed in all simulations; and the mean multiplicity frequency (**mf**), the mean companion probability (**cp**), and the mean companion frequency (**cf**).

4.4.5 Periods

Fig. 4.10 shows the number of stars formed in a simulation plotted against the periods of the multiple systems identified at the end of the simulation. These periods are derived on the assumption that all multiple systems are hierarchical, which is not always true. Thus the two periods for a triple system are extracted by finding the period for the pair with the greatest specific binding energy, then treating this pair as a single star and finding the period of its orbit relative to the third star. This is appropriate for stable hierarchical systems, but of limited value for unstable non-hierarchical systems.

We should therefore expect some subsequent evolution in these distributions, with mutual interactions tending to lead to close systems becoming more tightly bound (occasionally with exchange of components) and wide systems being disolved. Eventually there will also be interactions with stars formed in neighbouring cores. These interactions will further disrupt the wider systems but have little effect on the closer systems. However, our simulations are not continued long enough for interactions with

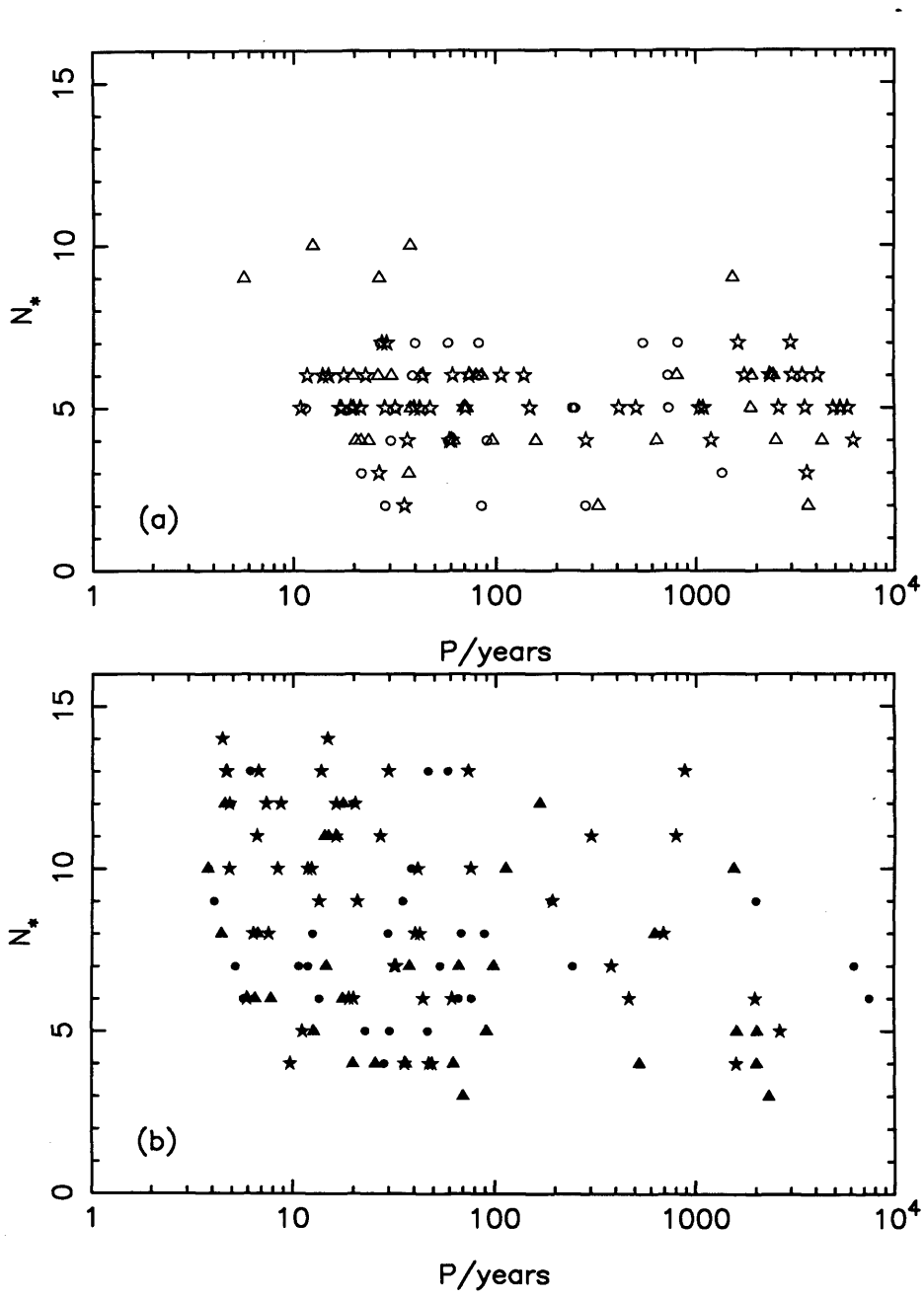

Figure 4.10: For each multiple system we plot the number of stars formed in that simulation, $N_\star$, against the period, P. (a) Results obtained using the barotropic equation of state; here open circles represent $\alpha_{\rm turb} = 0.05$, open triangles $\alpha_{\rm turb} = 0.10$, and open stars $\alpha_{\rm turb} = 0.25$. (b) Results obtained using the new treatment of the energy equation; here filled circles represent $\alpha_{\rm turb} = 0.05$, filled triangles $\alpha_{\rm turb} = 0.10$, and filled stars $\alpha_{\rm turb} = 0.25$.

Table 4.5: For each treatment of the energy equation, we record the mean, $\mu_{\log_{10}(P)}$, the standard deviation, $\sigma_{\log_{10}(P)}$, and the range of the period distribution.

THERMODYNAMICS	$\mu_{\log_{10}(P)}$	$\sigma_{\log_{10}(P)}$	RANGE (yr)
BAROTROPIC EQUATION OF STATE	2.2	1.0	$\sim 10 - 10^4$
NEW TREATMENT OF THE ENERGY EQUATION	1.7	1.0	$\sim 3 - 10^4$

stars formed in neighbouring cores to be important.

Fig. 4.11 shows the period distributions obtained using each treatment of the thermodynamics, and Table 4.5 lists the statistics of the period distribution obtained using each treatment of the thermodynamics. With the new treatment of the energy equation, the periods are on average shorter (by about a factor of 3). This is because the new treatment allows the gas – in particular, the gas in smaller proto-fragments – to stay cooler to higher densities. Consequently the Jeans length, and hence the separations between neighbouring stars, tend to be smaller.

There is no obvious dependence of the period distribution on the level of turbulence, although this must be set against the poor statistics (between 26 and 53 periods for each combination of thermodynamics and initial level of turbulence).

We should also caution that the low-period systems are poorly resolved, in the sense that at periastron the stars are closer together than $R_{\rm SINK}$, and therefore their gravitational interaction is softened. This means that they should probably be somewhat more tightly bound. We have checked the formation of the individual stars in some of these close systems, and established that in each case the two constituent stars (i.e. sinks) were initially created from well-defined and separate Jeans-unstable density peaks.

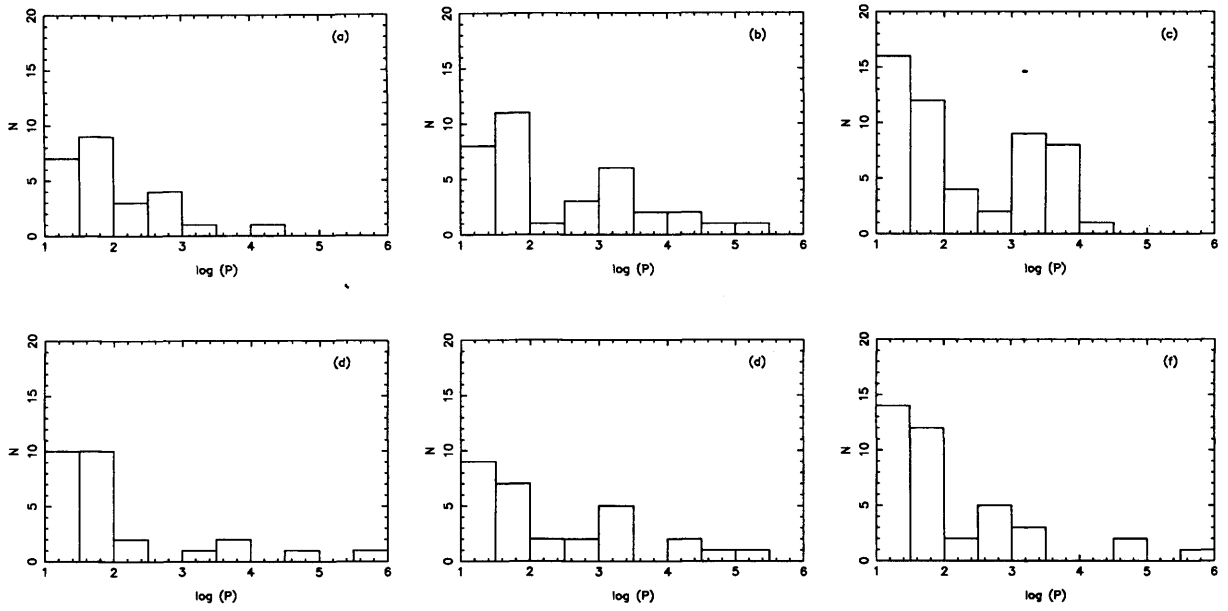

Figure 4.11: Period distributions. The top row gives the period distributions obtained with the barotropic equation of state for (a) $\alpha_{\rm TURB} = 0.05$, (b) $\alpha_{\rm TURB} = 0.10$, and (c) $\alpha_{\rm TURB} = 0.25$. The lower row gives the period distributions obtained with the new treatment of the energy equation for (d) $\alpha_{\rm TURB} = 0.05$, (e) $\alpha_{\rm TURB} = 0.10$, and (f) $\alpha_{\rm TURB} = 0.25$.

4.4.6 Eccentricities

Fig. 4.12 shows orbital eccentricities (e) plotted against periods (P), at the end of the simulations. The eccentricities are not strongly correlated with period, nor – *modulo* the poor statistics (see above) – do they appear to be correlated with the initial level of turbulence. However, there is a noticeable difference between the distributions obtained with the two different treatments of the thermodynamics. Using the barotropic equation of state, the distribution is concentrated towards high eccentricities, but there is still a substantial fraction, $\sim$ 25%, of systems having approximately circular orbits, $e \leq 0.2$. Using the new treatment of the energy equation, the distribution of eccentricities is more strongly skewed towards high values, and less than 6% have $e \leq 0.2$. This is also illustrated in Fig. 4.14, which shows the distribution of the orbital eccentricities for each treatment of thermodynamics.

The barotropic equation of state facilitates the formation of low-eccentricity bina-

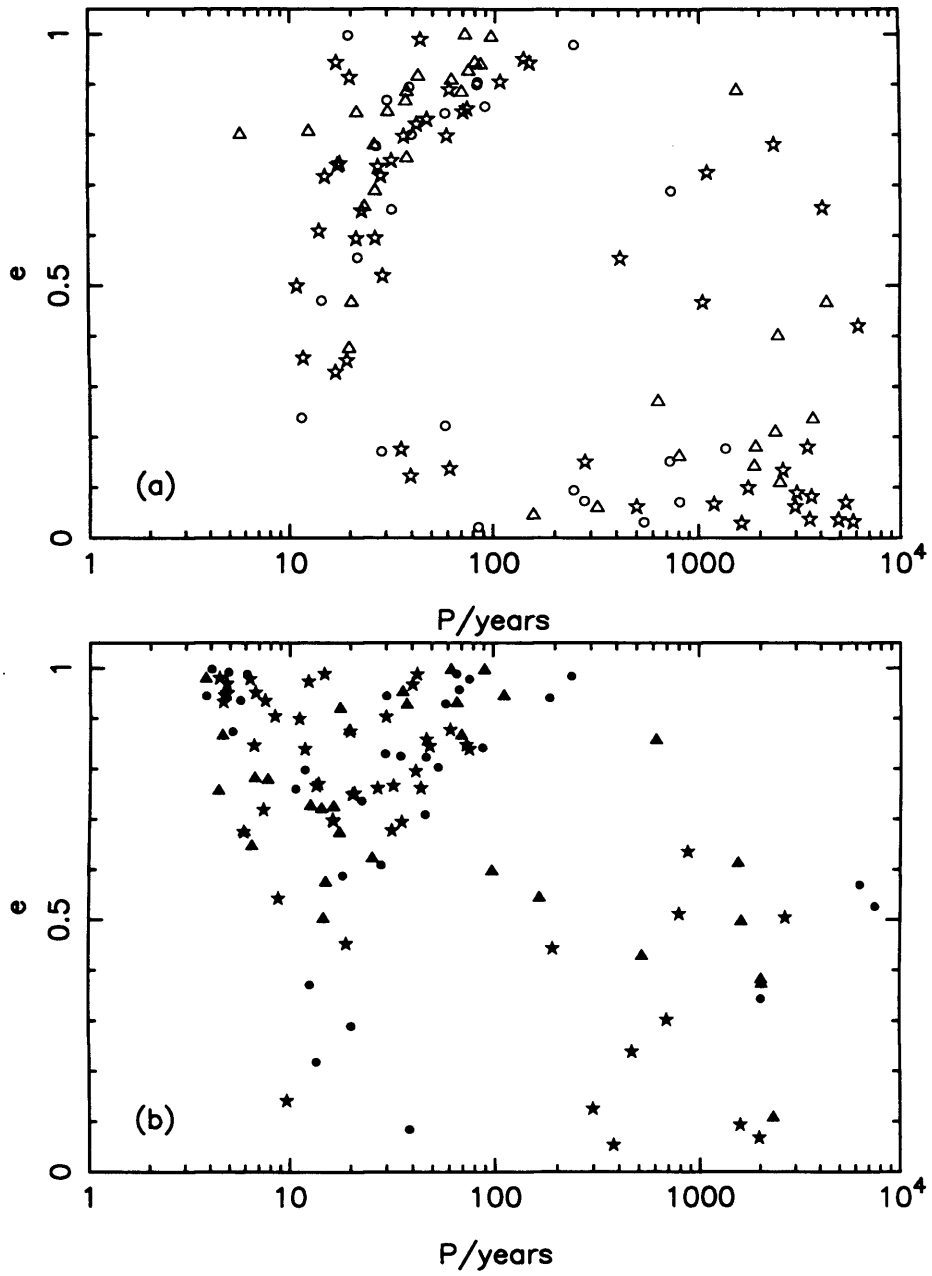

Figure 4.12: Orbital eccentricities, e, plotted against periods, P, for multiple protostars: (a) Results obtained using the barotropic equation of state; here open circles represent $\alpha_{\rm turb} = 0.05$, open triangles $\alpha_{\rm turb} = 0.10$, and open stars $\alpha_{\rm turb} = 0.25$. (b) Results obtained using the new treatment of the energy equation; here filled circles represent $\alpha_{\rm turb} = 0.05$, filled triangles $\alpha_{\rm turb} = 0.10$, and filled stars $\alpha_{\rm turb} = 0.25$.

ries by making it harder for circumbinary discs to fragment. At a given density the gas is hotter. Consequently, quite massive but relatively warm circumbinary discs resist further fragmentation and instead act to dampen orbital eccentricities by accreting slowly onto the existing binary components. In contrast, when the new treatment of the energy equation is used, massive circumbinary discs are relatively cool, so they fragment, and interactions between these additional fragments and the original components of the binary act to amplify the orbital eccentricities.

4.4.7 Mass ratios

Fig. 4.14 shows the distributions of mass ratio, $q \equiv M_2/M_1$, at the end of the simulations. The distributions are strongly skewed towards $q \sim 1$, i.e. nearly equal component masses. The mass ratios do not appear to be correlated with the initial level of turbulence, $\alpha_{\rm TURB}$, but again the statistics are poor. Mass ratios are correlated with orbital periods, in the sense that shorter-period systems tend to have higher mass-ratios, which is comparable with observations (e.g. Mazeh et al. 1992). Since simulations conducted with the new treatment of the energy equation tend to produce multiples with shorter periods, they also tend to produce multiples with higher mass ratios.

A mechanism which drives mass ratios towards unity in simulations of star formation was first described by Chapman et al. (1992), and has subsequently been noted by Burkert & Bodenheimer (1993) and by Bate & Bonnell (1998) (but see Ochi et al. 2005 for a different view and Clarke 2007 for a rebuttal of this different view). If a binary system continues to grow by accretion, the specific angular momentum of the infalling material (relative to the centre of mass of the binary system) tends to increase with time. Consequently the component with lower mass (the secondary, M_2), which necessarily is on a more extended orbit, is better disposed to assimilate this material with high angular momentum, and therefore it grows in mass until it is comparable with the primary (M_1). This is the mechanism that appears to be operating here. It is less effective in wide bi-

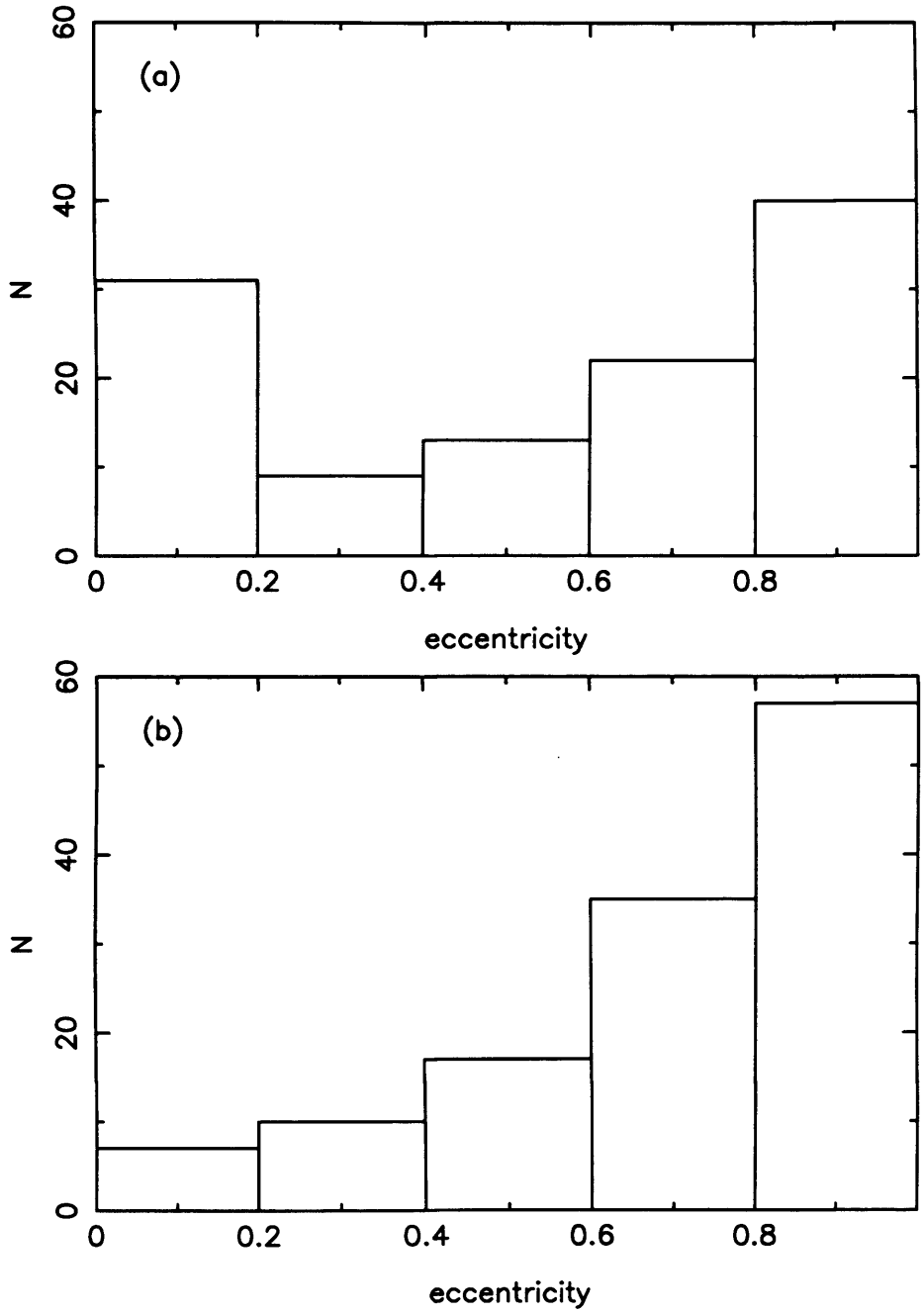

Figure 4.13: The distribution of eccentricities, e, for multiple protostars: (a) using the barotropic equation of state; (b) using the new treatment of the energy equation.

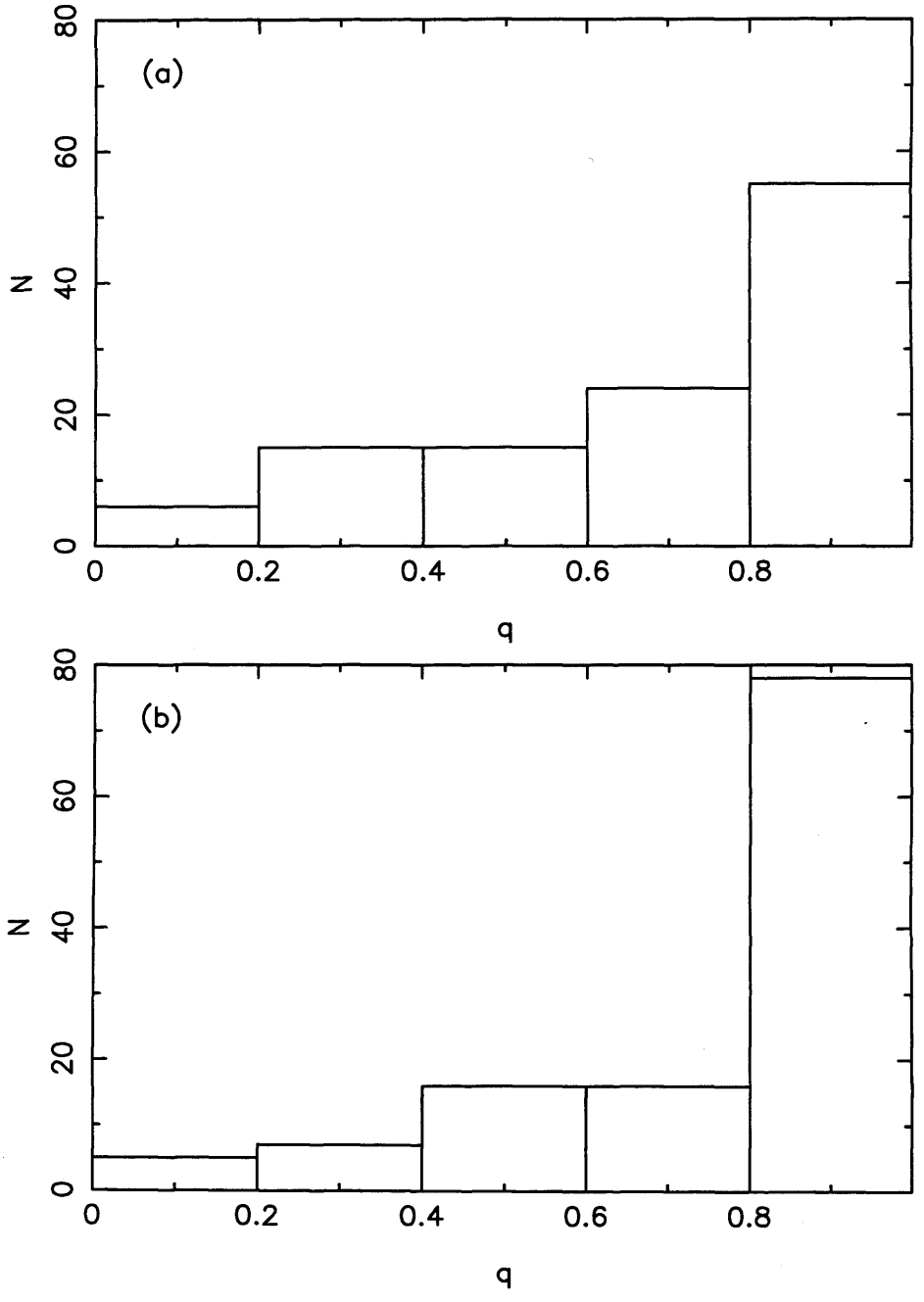

Figure 4.14: The distribution of mass ratios, q, for multiple protostars: (a) using the barotropic equation of state; (b) using the new treatment of the energy equation.

nary systems, because the components of a wide system tend to accrete from separate reservoirs.

4.4.8 Competitive accretion

We note that there is little evidence for competitive accretion in our simulations in the sense that it is rare to have a situation in which several protostars are competing to accrete from the same reservoir of material. The first star to form (the *primary*) is often, but not always, the most massive at the end. Stars forming later in the simulation frequently grow to masses comparable with, and occasionally even greater than, the primary. The material which ends up in these stars is normally rather coherently located. For example, once the circumprimary disc has formed, the material destined to form a particular secondary star accumulates in a particular range of radii, and sits there until it is mopped up by the growing secondary star. Ejection does play a role in separating some stars from the reservoir of material they might otherwise have accreted, and thereby creating very low-mass stars. However, the material which accretes onto a star was in general present at the star's inception; its self-gravity contributed to the condensation which triggered the formation of a sink by pushing the density above $\rho_{\rm SINK}$.

4.4.9 Missing physics

The switch from the standard barotropic equation of state to our new realistic treatment of the energy equation produces significant changes in the statistical properties of the stars resulting from the collapse and fragmentation of an isolated, low-turbulence, 5.4 $M_\odot$ core. However, there are several important physical effects missing from our simulations. In particular, there is no feedback from the stars, there are no (non-ideal) MHD effects, and the use of sink particles raises some concerns.

Feedback. Feedback from stars can take several forms.

(i) The radiation from the stars will heat the surrounding dust and gas. Krumholz, Klein & McKee (2007) have recently simulated the collapse and fragmentation of more massive cores (100 and 200 $M_{\odot}$) with much higher initial levels of turbulence than those invoked in our simulations. Their treatment of the thermodynamics takes account not only of the energy equation and the transport of cooling radiation, but also of radiative feedback from the forming stars in the core. They find that their cores only spawn a small number of stars. This is because the primary protostar, which forms early on from material with relatively low angular momentum, has a high luminosity, and therefore stabilises the inner parts of its circumstellar accretion disc, by heating them up. Fragmentation is only possible in the outer more diffuse parts of the disc. We expect a similar – but more modest – effect in low-mass, low-turbulence cores, more modest because the primary luminosity will be much smaller. Nonetheless, it is likely that, even in the low-mass regime, the luminosity of the primary star is sufficient to inhibit fragmentation of the inner disc. The analytic work of Whitworth & Stamatellos (2006) predicts that a disc around a Sun-like primary is unlikely to fragment inside ~ 100 AU, and this is confirmed by the simulations of Stamatellos et al. (2007b) and Stamatellos & Whitworth (2008a,b). Consequently, the primary will end up more massive (by accreting the matter which is unable to fragment); the circumprimary disc will take longer to grow to Toomre instability; and the secondaries which then condense out of it will be smaller in number, and at larger radii.

(ii) Mechanical feedback, in the form of bipolar outflows will punch holes in the core. Preliminary exploration of this phenomenon (Stamatellos et al. 2005) suggests that it does not greatly change the efficiency of star formation, but it does slow it down (i.e. the delay between the formation of the primary and the formation of the secondaries is longer). This needs to be explored further.

(iii) Ionising radiation and winds from massive stars produce more violent feedback. We have recently developed the numerical machinery to explore this (Bisbas et al., in preparation), but it is not part of the star-formation mode we are concerned with

here, which involves cores which have too little mass to form ionising stars.

MHD. Non-ideal MHD effects are likely to play an important role, and we have introduced divergence cleaning into the code of Hosking & Whitworth (2004). However, it is still a rather crude and inefficient code, and further work is ongoing to improve it to the stage where it can be used to perform a large ensemble of simulations. Price & Bate (2008) have simulated the collapse and fragmentation of a massive magnetised turbulent core, using an ideal MHD code, with a barotropic equation of state. They find that the magnetic field reduces both the efficiency of star formation (i.e. the fraction of the core mass which ends up in stars) and the production of brown dwarfs. In an earlier paper (Price & Bate 2007), using more idealised initial conditions (a spherical uniform-density cloud with an imposed $m = 2$ perturbation), they have shown that a magnetic field can also inhibit disc fragmentation, by slowing the rate of disc growth and accelerating the rate at which angular momentum is redistributed.

Sinks. Finally, we note that the use of sinks may compromise our results, in ways which are hard to quantify. First, it means that all processes on scales below $\sim 2R_{\rm SINK} = 10$ AU are at best not properly resolved (e.g. orbits), and at worst excised completely (e.g. the second collapse when molecular hydrogen dissociates). Second, the creation of sinks favours N-body interactions, and hence ejections of stars, whilst suppressing dissipative interactions between, and mergers of, stars. One can postpone the creation of sinks until very high densities are reached. For example, Stamatellos et al. (2007b) use $\rho_{\rm SINK} = 10^{-2}\,{\rm g\,cm^{-3}}$. However, this is very expensive computationally.

4.4.10 Comparison with observation

Since we only treat a single core mass, with a single initial radius and a single initial density profile, and since – as discussed in the preceding section – there are several potentially critical physical effects which are not included in our simulations, we do not expect to reproduce all the observed statistical properties of real stars. Nonetheless, it is

appropriate to rehearse the various counts on which the properties of stars formed in our simulations conform to, or diverge from, reality; and to speculate on the reasons.

Mean number of stars per core, $\overline{N}_\star$. Our simulations form too many stars per core, and furthermore this over-production of stars is significantly exacerbated by the switch from the barotropic equation of state to the new, more realistic treatment of the energy equation. This is because the new treatment allows circumstellar discs, and low-mass fragments thereof, to stay cool to higher densities than the barotropic equation of state (which treats all gas as if it were at the centre of a collapsing, non-rotating $1\,\mathrm{M}_\odot$ protostar). The analytic results of Rafikov (2005), Matzner & Levin (2005), Kratter & Matzner (2006) and Whitworth & Stamatellos (2006), and the numerical simulations of Krumholz, Klein and McKee (2007), Stamatellos et al. (2007b) and Stamatellos & Whitworth (2008a,b) all suggest that the inclusion of radiative feedback reduces the number of stars formed, essentially by heating the inner disc, and thus suppressing Toomre instability by increasing the cooling time (Toomre 1964; Gammie 2001). Whitworth & Stamatellos (2006) show that, given a solar-mass primary star at the centre of the disc, it can only fragment at large radii, $R \geq 100\,\mathrm{AU}$. The inclusion of mechanical feedback (Stamatellos et al. 2005) and/or a magnetic field (Price & Bate 2008) is also likely to reduce the number of stars formed, and in particular the number of brown dwarfs, by reducing the rate of accretion onto the primary and its circumprimary disc. Indeed, these effects are probably essential to reduce the efficiency of star formation in low-mass cores to the levels infered from observation. These levels are typically $\sim 30\,\%$ (e.g. Nutter & Ward-Thompson 2007; Simpson et al. 2008).

Mass distribution. The overall mass distribution produced by a single core, as a fraction of the core's total mass, is not constrained by observation; if it were, we would know how to map the observed core mass function into the stellar initial mass function. One interesting feature of our results is the suggestion that, amongst the stars spawned by a single core, there might be a bimodal distribution of masses, comprising primary stars formed relatively early on, and secondary stars of much lower mass formed somewhat

later by disc fragmentation. We also note that the mass of core that we are simulating ($\sim 5.4 M_{\odot}$) is rather larger than the average isolated core (e.g. Alvés et al. 2007; Nutter & Ward-Thompson 2007). This further complicates any attempts to map the results of these simulations onto the observed distributions which are the sum of a variety of core masses, mostly somewhat smaller than our core.

Multiplicity. The multiplicity frequency of the stars formed in our simulations, **mf** ~ 0.2, is too low, especially for the higher-mass stars; for the brown dwarfs and very low-mass hydrogen-burning stars (those with $M_{\star} < 0.1\,\mathrm{M}_{\odot}$) **mf** ~ 0.2 is actually in the middle of the range inferred from the limited observations available (Burgasser et al. 2007; Luhman et al. 2007; Joergens (2008). The multiplicity frequency is expected to rise if the inclusion of extra physics reduces the number of stars formed from a single core. If this reduction is attributable to the suppression of fragmentation in the inner parts of circumprimary discs, then the simulations of Stamatellos et al. (2008b) suggest that it will increase the multiplicity frequency of the higher mass stars ($M_{\star} \sim \mathrm{M}_{\odot}$), and have little effect on the multiplicity frequency of the very low-mass stars ($M_{\star} < 0.1\,\mathrm{M}_{\odot}$); the simulations would then accord better with the observed distribution of multiplicity frequency, which appears to be a monotonically decreasing function of primary mass (e.g. Joergens 2008).

Binary periods. The periods, P, of the binary systems formed in our simulations fall in the range $3 \leq [P/\mathrm{yr}] \leq 10^4$. Systems with shorter periods cannot be resolved, because the gravitational fields of sink particles are softened at distances closer than $R = 5$ AU. Systems with longer periods must either form in more extended cores than the one we have modelled here, or they must result from interactions between stars formed in separate cores. An encouraging feature of the multiple systems formed in our simulations is the fact that most of the very low-mass systems ($M_1 < 0.1\,\mathrm{M}_{\odot}$) have periods in the range 10 to 100 yr, in good agreement with the separations of observed very low-mass systems (e.g. Joergens 2008).

Mass ratios and eccentricities. The mass ratios of the multiple systems formed in our simulations are concentrated towards high values. This again accords with what is observed for very low-mass systems (e.g. Burgasser et al. 2007; their Fig. 5a), but contrasts with the flatter distribution observed in higher-mass systems. The multiple systems formed in our simulations are also skewed towards much more eccentric orbits than observed systems. However, the eccentricity distribution at birth is almost impossible to compare to the distribution in older systems. Firstly, close systems will be circularised by tidal and other dissipative forces. Secondly, wider systems will be subject to encounters which will rapidly change the birth eccentricity distribution beyond recognition (Parker et al., in preparation). Our simulations do not address these possibilities.

4.4.11 Convergence

We have repeated one of our simulations with 50,000 and 80,000 SPH particles, to check whether our simulations are converged, in a statistical sense (i.e. whether the statistical distributions of stellar parameters does not depend on the number of SPH particles used). For this purpose we have chosen simulation T011, which has an initial level of turbulence $\alpha_{\rm TURB} = 0.10$, and uses the new treatment of the energy equation; the mean number of stars formed with this combination is $\overline{N}_\star = 6.2$ (see Table 4.3). In the original T011 simulation, with just 25,000 SPH particles, 6 stars are formed. With 50,000 SPH particles 6 stars are again formed. With 80,000 SPH particles 8 stars are formed. We stress that in this context convergence can only be discussed in a statistical sense. This is because, with the low initial levels of turbulence we are using, the gravitational fragmentation that ensues is seeded from two sources. There are the small density enhancements created by subsonic converging flows due to the initial imposed turbulent velocity field; these are reproducable when using different particle numbers. However, there is also particle noise; this is not reproducable when using different particle numbers. Therefore convergence can only be tested fully by repeating the whole ensemble of simulations

with higher particle numbers, and this is not feasible with the computational resources at our disposal. We are currently preparing a paper which demonstrates convergence in a simulation of gravitational fragmentation by using very carefully relaxed initial conditions; the imposed perturbation (which is reproducable) is then able to dominate particle noise in seeding gravitational fragmentation. These simulations exhibit excellent convergence, as do the simulations of Jeans instability presented by Hubber et al. (2006). We are therefore confident that our code is capturing gravitational fragmentation faithfully.

4.5 Summary

We have performed a large ensemble of SPH simulations of the collapse and fragmentation of an isolated, turbulent 5.4 $M_{\odot}$ core, with a view to establishing how the statistical properties of the resulting stars are influenced by (i) different initial level of turbulence, and (ii) different treatments of the thermodynamics. We consider three initial levels of turbulence, characterised by $\alpha_{\rm TURB}$ = 0.05, 0.10 and 0.25. We treat the thermodynamics firstly with a standard barotropic equation of state, and secondly with a new treatment of the energy equation which captures all the important energy modes of the gas and takes account of radiation transport and variations in the opacity. The main results are summarised as follows.

1. Increasing the initial level of turbulence tends to reduce the efficiency of star formation, η (i.e. the fraction of the core mass which is converted into stars after 300 kyr), and to increase the number of stars formed by a single core, $N_{\star}$, but the effect is very small, and all the other statistical properties of the stars formed are essentially independent of $\alpha_{\rm TURB}$.

2. We observe a common pattern in which the low–angular-momentum material in the core collapses to form the primary after 50 to 70 kyr, and then a massive disc builds

up around the primary. As soon as this circumprimary disc becomes Toomre unstable (which may take from 10 to 100 kyr), it rapidly breaks up into a bunch of secondary stars. Those secondaries that are quickly ejected from the disc normally end up as brown dwarf stars, whereas those secondaries that stay in the disc tend to grow by accretion, and sometimes they even grow larger than the primary.

3. Switching from the standard barotropic equation of state to our new more realistic treatment of the energy equation has several systematic effects:

- the efficiency of star formation ($\eta \equiv \sum \{M_\star\} / M_{\rm CORE}$) is reduced significantly (by $\sim 15\%$);
- the number of protostars formed ($N_\star$) is greatly increased (by $\sim 40\%$);
- a higher proportion of brown dwarf stars is formed;
- the mean period of multiple systems is reduced (by a factor ~ 3);
- the orbital eccentricities of multiple systems tend to be higher;
- the mass ratios of multiple systems tend to be higher (i.e. more nearly equal components).

All these trends can be attributed to the fact that the barotropic equation of state assumes that all gas is at the centre of a collapsing spherical 1 $M_\odot$ protostar, and therefore it becomes adiabatic at relatively low densities. In contrast, our new more realistic treatment of the energy equation allows the gas in low-mass proto-fragments to remain approximately isothermal to relatively high densities, because in a lower-mass proto-fragment the column-density trapping cooling radiation tends to be smaller, and the rate of contraction (and hence the rate of compressional heating) tends to be slower – as compared with the rates at the centre of a collapsing spherically-symmetric 1 $M_\odot$ protostar.

4.6 Future work

We have extended this work to modelling prestellar cores in Ophiuchus, using the new, more realistic treatment of the energy equation and the observations of Motte et al. (1998) and André et al. (2007). The results are shown in Chapter 5.

Future plans involve taking into account more of the deterministic effects that occur in star formation. In particular, we would like to explore the effect of radiative feedback from stars. We predict that by modelling feedback we can reduce the efficiency of star formation from the very high levels produced here ($\sim 60\%$) to values more compatible with observation ($\lesssim 30\%$; Alves et al. 2007; Nutter & Ward-Thompson 2007; Goodwin et al. 2008).

Chapter 5

The evolution of prestellar cores in the Ophiuchus Main Cloud

In this chapter we extend our study of the collapse and fragmentation of low mass cores using initial conditions constrained by observations. Specifically, we model the evolution of an ensemble of prestellar cores with properties matching those detected in the Ophiuchus Main Cloud by André et al (2007). In contrast to the simulations in Chapter 4, we are here considering cores with a range of masses, sizes and levels of turbulence, with a view to predicting the statistical properties of the stars they spawn. Previous analyses of the Ophiuchus Main Cloud have assumed that these cores have dust temperatures in the range of 12K – 20K. *Using a 3D radiative transfer model of this region, Stamatellos et al. (2007c) find that the dust temperatures should be lower, which results in the core masses being larger than previous estimates, by a factor of* $\sim 2 - 3$. *For a sample of cores we set initial conditions using the sizes and levels of turbulence from Motte et al. (1998) and André et al. (2007) and the adjusted core masses according to Stamatellos et al. (2007c), and we then simulate their evolution.*

5.1 Introduction

The Ophiuchus molecular cloud complex is one of the closest star-forming regions, located at a distance of (139 ± 6) pc (Mamajek 2008). The complex consists of two main clouds, L1688 and L1689. In addition there are filaments extending from these clouds towards the north-east (see Fig. 5.1). These are usually referred to as the 'streamers' or 'cobwebs' of Ophiuchus, and extend over tens of parsecs (Loren 1989). Fig 5.1 also shows the star ρ Ophiuchus 1° to the north of L1688.

Ophiuchus is an active site of star formation, with star formation efficiency in the range 14–40% (Vrba 1977). It is thought that the star formation may have been triggered by the Upper Scorpious OB association, located to the west of L1688 and L1689. In this scenario, cloud collapse is triggered by shocks associated with expanding HII regions, stellar wind shells, and supernova remnants. The resulting star formation may trigger further star formation, which propagates through the cloud.

L1688 is the more massive of the two clouds, with a mass of 1447 $M_\odot$, and spans 1pc × 2pc on the sky. It is for this reason L1688 is generally known as the Ophiuchus Main Cloud.

Numerous studies show that the Main Cloud is populated with a large number of prestellar cores and also protostars at different stages in their evolution (e.g Wilking et al. 1989, Motte et al. 1998, Johnstone et al. 2000, Stanke et al. 2006, Simpson et al. 2008). There are six major clumps observed in the Ophiuchus Main Cloud (Oph-A, Oph-B, Oph-C, Oph-D, Oph-E and Oph-F). These clumps, shown in Fig. 5.2, are approximately 0.3 pc in size, each with a mass of a few tens of solar masses.

The region containing the clumps has been mapped in a 1.2 mm continuum survey by Motte et al (1998). They sample an area of order 1 pc^2, using the molecular cloud tracer DCO^+ to identify dense clumps. They detect 58 prestellar cores and, by adopting dust temperatures of T_D = 12K – 20K, calculate masses in the range 0.1 – 3 $M_\odot$ for

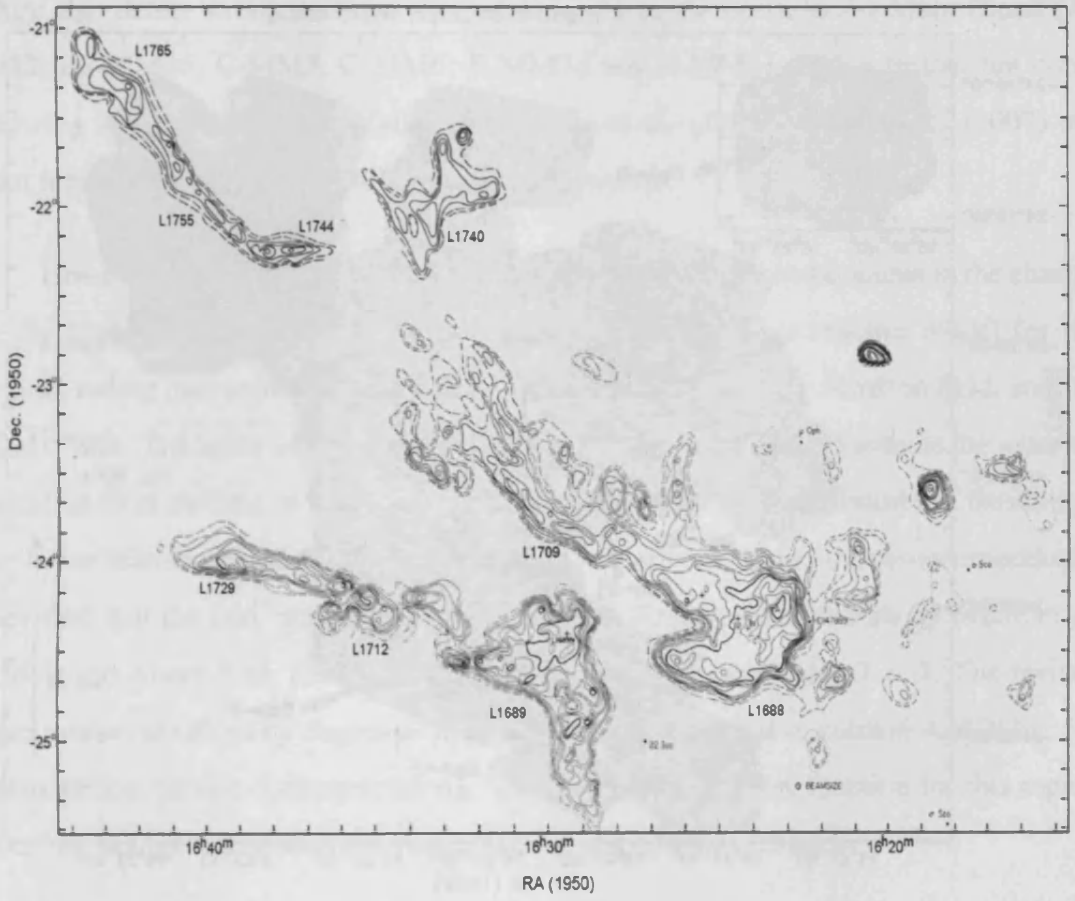

Figure 5.1: ^{13}CO map of Ophiuchus, taken from Loren (1989) and modified by Nutter et al. (2006). The contour levels give antenna temperatures of 4, 5, 6, 7, 8, 10, 12, 14, 18, 20K.

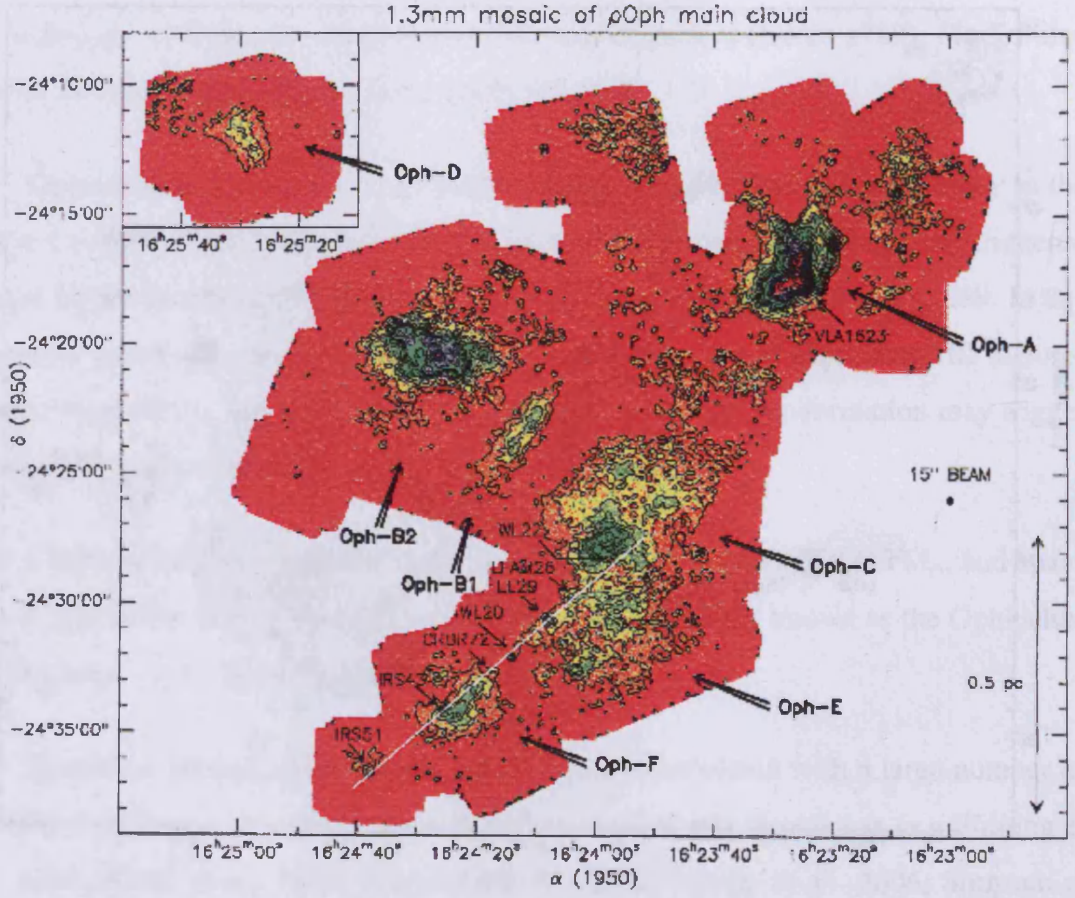

Figure 5.2: Millimeter continuum mosaic of the 6 major clumps in the Ophiuchus main cloud, from Motte et al. (1998).

these cores.

More recently, André et al. (2007) have re-observed the cores detected by Motte et al., using the molecular lines $N_2H^+(1 \rightarrow 0)$, $CS(2 \rightarrow 1)$, $CS(3 \rightarrow 2)$, $H_2CO(2_{12} \rightarrow 1_{11})$, and $HCO^+(3 \rightarrow 2)$. They find that the cores appear to be gravitationally bound and prestellar in nature. They detect subsonic levels of internal turbulence within the cores. They also detect strong evidence for infall in six of the cores in the Main Cloud (A-SM2, B2-MM16, C-MM5, C-MM6, E-MM2d and E-MM4), with a further ten cores showing weak evidence for infall. As in Motte et al. (1998), André at al. (2007) use dust temperatures of 12K – 20K to estimate masses.

However, Stamatellos et al. (2007c) have estimated dust temperatures in the clumps in the Ophiuchus Main Cloud by constructing a 3D radiative transfer model for the region, taking into account external heating by (i) the interstellar radiation field, and (ii) HD147889. The latter is a nearby luminous B2V star, thought to dominate the external radiation field incident on the clumps. They conclude that the temperatures of the clumps are lower than those which previous studies have assumed. Using the new temperatures, they find that the core masses calculated from millimetre observations by Motte et al. (1998) and André et al. (2007) are underestimated by a factor of $\sim 2 - 3$. The revised core masses obtained by Stamatellos et al. (2007c) are listed in column 4 of Table 5.2 (Stamatellos, private communication). The resultant core mass function for this region does not change significantly in shape, but moves to higher masses.

To continue this study of the Main Cloud, we use the temperatures and adjusted masses calculated by Stamatellos et al. (2007c) to simulate the evolution of an ensemble of cores. Each core is modelled using the dimensions determined by Motte et al. (1998) and the appropriate level of turbulence observed by André et al. (2007). This is a different approach to that taken in Chapter 4, where we modelled a single core of fixed mass and size, for many different realisations of the turbulent velocity field. Here we simulate cores with a range of masses, sizes and levels of turbulence and determine their evolution.

5.2 Initial conditions

5.2.1 Density profile and mass

The density structure of a low-mass prestellar core is approximately flat in the centre of the core, then falls off radially with exponent $2 \leq -d\ell og(\rho)/d\ell og(r) \leq 5$ in the envelope. To represent this, we use a spherically symmetric Plummer-like density profile,

$$\rho(r) = \rho_{\rm o} \left\{ 1 + \frac{Cr^2}{ab} \right\}^{-1} . \tag{5.1}$$

$\rho_{\rm o}$ is the density at the centre of the core, and a and b are the projected dimensions of the core. The dimensions are taken from Table 2 in Motte et al. (1998), which lists the full width half maximum (FWHM) of each core. We assume the core boundary to be $r_{_B} = (ab)^{1/2}$. C is defined so that the density contrast between the centre of the core and its boundary is $C + 1$. Observations indicate that this contrast is typically comparable with the value for a critical Bonnor-Ebert sphere, i.e. $C + 1 \sim 14$, so we put $C \sim 13$. $\rho_{\rm o}$ can then be adjusted to give the required total mass, i.e.

$$M_{\rm TOT} = \int_{r=0}^{r=(ab)^{1/2}} \rho(r)\, 4\pi r^2\, dr \tag{5.2}$$

$$= \int_{r=0}^{r=(ab)^{1/2}} \rho_{\rm o} \left\{ 1 + \frac{Cr^2}{ab} \right\}^{-1} 4\pi r^2\, dr . \tag{5.3}$$

Using the substitution

$$\frac{Cr^2}{ab} = \tan^2(\theta) \tag{5.4}$$

and the differential of Equation (5.4)

$$dr = \left(\frac{ab}{C} \right)^{1/2} \sec^2(\theta)\, d\theta , \tag{5.5}$$

Table 5.1: Estimated temperatures for each clump.

Clump	Oph-A	Oph-B1	Oph-B2	Oph-C	Oph-D	Oph-E	Oph-F
Temperature (K)	6	7	7	7	7	7	8

we have

$$M_{\rm TOT} = 4\pi\rho_{\rm o}\left(\frac{ab}{C}\right)^{3/2}\int_{\theta=0}^{\theta=\tan^{-1}(C^{1/2})}\tan^2(\theta)\,d\theta \quad (5.6)$$

$$= 4\pi\rho_{\rm o}\left(\frac{ab}{C}\right)^{3/2}\left[\tan(\theta)-\theta\right]_{\theta=0}^{\theta=\tan^{-1}(C^{1/2})} \quad (5.7)$$

$$= 4\pi\rho_{\rm o}\left(\frac{ab}{C}\right)^{3/2}\left[C^{1/2}-\tan^{-1}(C^{1/2})\right]. \quad (5.8)$$

Hence, we must set

$$\rho_{\rm o} = \frac{\mathcal{D}M_{\rm TOT}}{(ab)^{3/2}}, \quad (5.9)$$

$$\mathcal{D} = \frac{C^{3/2}}{4\pi[C^{1/2}-\tan^{-1}(C^{1/2})]}. \quad (5.10)$$

Since we set $C = 13$, this gives $\mathcal{D} = 1.62$.

5.2.2 Temperature

We set the temperature of each core according to which clump it is located in. The temperatures estimated by Stamatellos et al. (2007c) are shown in Table 5.1. The Oph-B1 clump is excluded from their study because it is flattened in shape, therefore a spherical geometry cannot be assumed as with the other clumps. We assume that it has the same temperature as the nearby clumps Oph-B2 and Oph-C, i.e. ~ 7K The Oph-E clump is also excluded from their study, as it appears to be part of Oph-C and we therefore

give it the same temperature as Oph-C, i.e. ~ 7K. The temperature values estimated by association in this way are shown in bold in Table 5.1.

5.2.3 Turbulence

We use the levels of turbulence observed by André et al. (2007; Table 4), i.e.

$$\frac{\alpha_{\rm TURB}}{\alpha_{\rm THERM}} = \left(\frac{\sigma_{\rm NT}}{\sigma_{\rm T}}\right)^2 \tag{5.11}$$

where $\alpha_{\rm TURB}$ is the ratio of turbulent to gravitational energy, and $\alpha_{\rm THERM}$ is the ratio of thermal to gravitational energy. To obtain $\alpha_{\rm TURB}$ we calculate $\alpha_{\rm THERM}$ for each core and multiply by $(\sigma_{\rm NT}/\sigma_{\rm T})^2$ from column 11 of Table 4 in André et al. (2007). To create the initial turbulent velocity field in a core, we use the same prescription as in Section (4.2) and impose an initial divergence-free Gaussian random velocity field on that core. The power spectrum of this velocity field is set to be $P(k) \propto k^{-4}$.

5.2.4 Equation of state

The energy equation and the associated radiation transport are treated using the technique described in detail in Section (4.2). The method takes into account the thermal history of protostellar gas, and also captures thermal inertia effects. This is a much more realistic approach than invoking a barotropic equation of state.

5.2.5 Numerical details

For these simulations, we use the DRAGON SPH code, described in Chapter 2. We adopt a sink density threshold $\rho_{\rm SINK} = 10^{-10}\,{\rm g\,cm^{-3}}$ and a sink radius $R_{\rm SINK} = 1.92\,{\rm AU}$. Note that the cores modelled here typically have an initial central density an order of

magnitude higher than those in Chapter 4. Hence we must increase the sink density threshold to mitigate the risk of spurious creation of protostars. The minimum resolvable mass is given by

$$M_{\rm MIN} \sim \frac{N_{\rm NEIB}\, M_{\rm TOT}}{N_{\rm TOT}} \rightarrow \frac{M_{\rm TOT}}{400} \tag{5.12}$$

and therefore depends on $M_{\rm TOT}$; for the most massive cloud simulated here, $M_{\rm MIN} \equiv 25 M_{\rm JUPITER}$. It would be better to fix $M_{\rm MIN}$ and vary $N_{\rm TOT}$ and this is the strategy we will adopt in the future. However, with the computational resources available to us that was not feasible. See Section 2.10 for further discussion of the resolution requirements imposed by the Jeans condition (Bate & Burkert 1997).

To set up the initial conditions we firstly place a large number of particles ($N > 60,000$) randomly in a cube and settle them using DRAGON to produce a relaxed uniform-density distribution. We then cut out a sphere containing the required number of particles, which in this case is $N = 20,000$. Finally, we stretch the particle distribution radially to produce the density profile in Equation (5.1).

We perform simulations for the observed prestellar cores in Oph-A, Oph-B1, Oph-B2, Oph-C, Oph-E and Oph-F. We exclude the Oph-D clump because André et al. (2007) do not calculate the levels of turbulence for the cores in this clump and we do not have any information on which to base an estimate. There are also some cores within the remaining clumps that do not have a calculated $\alpha_{\rm TURB}$. We estimate their levels of turbulence based on the levels of the other cores within the clump. These figures are shown in bold in column 6 of Table 5.2.

Stamatellos et al. (2007c) exclude the Oph-B1 clump from their simulations due to the difficulty in modelling its flattened structure. The clump is located in the neighbourhood of Oph-B2 and Oph-C, which are both estimated to be at 7K, so we assume Oph-B1 is at the same temperature. We also assume a temperature of 7K for Oph-E, because it appears to be part of Oph-C.

5.3 Results

5.3.1 Basic parameters of the cores and the stars they spawn

For each core, Table 5.2 records the initial linear size (as projected on the sky, column 2); the initial temperature (column 3); the total mass (column 4); the central density (column 5): the initial level of turbulence (column 6); the total number of stars at the end of the simulation (including brown dwarfs, column 7); the total number of brown dwarfs at the end of the simulation (column 8); the types of multiple systems formed (column 9); and the masses of the individual stars (column 10). The bold values – in columns 3 and 6 respectively – indicate values of the initial temperature and level of turbulence adopted in cases where there is no reliable observational or theoretical estimate.

5.3.2 Overview

In the remainder of this chapter we analyse the results of these simulations of Ophiuchus cores, and attempt to relate the distributions of stellar properties (stellar masses, multiplicities, etc.) to the input parameters (core masses, $M_{\rm TOT}$, central densities, $\rho_{\rm O}$, and levels of turbulence, $\alpha_{\rm TURB}$).

However, at the outset we should stress that the statistics are inevitably poor, since we only have observed properties for 48 cores. We could improve the statistics by performing multiple realisations of each core in the ensemble, invoking a different seed for the turbulent velocity field each time. We have indeed performed a few additional simulations in this spirit, and these simulations confirm that the results are credible in the following sense. If we perform additional simulations of a core which collapses and fragments to form many protostars, then it usually does so in most of the additional simulations (typically 3 of the 4 additional simulations) – even though the realisation of the turbulent velocity field is completely different in each simulation. Conversely, if

Table 5.2: Results of the simulations of an ensemble of cores in the Ophiuchus Main Cloud, evolved for 300 kyr. Column 1 gives the name of the core, column 2 gives its size, FWHM, column 3 gives its temperature, T, column 4 gives its total mass, $M_{\rm TOT}$, column 6 gives $\alpha_{\rm TURB}$, column 7 gives the total number of stars formed, $N_\star$, column 8 gives the number of brown dwarfs formed, $N_{\rm BD}$, column 9 gives the order of any multiple systems formed, and column 10 gives the masses of individual stars, with a superscript to indicate those which are components of binary systems ($M_\star^b$), triple systems ($M_\star^t$), or quadruple systems ($M_\star^q$).

Source	FWHM (AU × AU)	T (K)	$M_{\rm TOT}$ ($M_\odot$)	ρ_o (g cm^{-3})	$\alpha_{\rm TURB}$	$N_\star$	$N_{\rm BD}$	Mult	$M_\star$ ($M_\odot$)
A-MM4	4000 × 1400	6	0.450	3.256×10^{-17}	0.129	8	6	T	0.113^t, 0.092, 0.073, 0.061, 0.045, 0.008, 0.007^t, 0.002^t
A-MM5	3700 × 2900	6	0.739	2.016×10^{-17}	0.009	1	0		0.705
SM1N	3000 × 1800	6	4.179	3.193×10^{-16}	0.010	5	1		1.182, 1.059, 1.003, 0.782, 0.021
SM1	6100 × 2100	6	10.287	2.151×10^{-16}	0.017	14	6	T	1.776^t, 1.177^t, 1.660^t, 1.639, 1.337, 1.143, 0.538, 0.378, 0.076, 0.059, 0.056, 0.035, 0.027, 0.015
SM2	6200 × 3400	6	4.179	4.140×10^{-17}	0.014	2	0	B	2.091^b, 1.960^b
A-MM8	2900 × 2100	6	0.418	2.667×10^{-17}	0.048	1	0		0.384
B1-MM1	400 × 400	7	0.226	3.386×10^{-15}	**0.009**	1	0		0.224
B1-MM2	3000 × 2100	7	0.384	2.328×10^{-17}	0.035	1	0		0.342
B1-MM3	1800 × 1300	7	0.361	9.670×10^{-17}	0.022	1	0		0.345
B1-MM4	4600 × 3200	7	0.474	8.047×10^{-18}	0.043	1	0		0.403
B1B2-MM1	2700 × 1800	7	0.226	2.023×10^{-17}	0.052	1	0		0.186
B1B2-MM2	4800 × 4100	7	0.745	8.182×10^{-18}	**0.032**	1	0		0.664
B2-MM1	400 × 400	7	0.316	4.734×10^{-18}	0.007	1	0		0.313
B2-MM2	4500 × 2400	7	1.061	2.866×10^{-17}	**0.017**	1	0		1.030
B2-MM3	400 × 400	7	0.271	4.060×10^{-15}	**0.032**	1	0		0.268
B2-MM4	2100 × 960	7	0.609	2.040×10^{-16}	0.035	1	0		0.601
B2-MM5	2200 × 960	7	0.587	1.834×10^{-16}	0.054	1	0		0.545
B2-MM6	4300 × 2700	7	1.761	4.268×10^{-17}	0.075	4	0	B	0.763^b, 0.472^b, 0.275, 0.209
B2-MM7	400 × 400	7	0.519	7.775×10^{-15}	**0.037**	1	0		0.515
B2-MM8	4000 × 4000	7	3.386	5.073×10^{-17}	0.045	13	0	Q	0.737^q, 0.687^q, 0.336, 0.297^q, 0.291, 0.288, 0.233, 0.218, 0.058, 0.057^q 0.023, 0.009, 0.007
B2-MM9	1600 × 960	7	0.700	3.256×10^{-16}	**0.068**	3	0	T	0.492^t, 0.107^t, 0.088^t
B2-MM10	3400 × 2200	7	1.354	6.346×10^{-17}	**0.044**	1	0		1.318
B2-MM11	400 × 400	7	0.339	5.079×10^{-16}	0.122	1	0		0.335
B2-MM12	2100 × 1300	7	0.880	1.871×10^{-16}	0.018	1	0		0.857
B2-MM13	400 × 400	7	0.429	6.427×10^{-15}	**0.099**	1	0		0.424
B2-MM14	2100 × 1800	7	0.971	1.267×10^{-16}	**0.095**	4	1	B	0.420^b, 0.253, 0.247^b, 0.022
B2-MM15	400 × 400	7	0.384	5.753×10^{-15}	0.092	1	0		0.379
B2-MM16	2700 × 1300	7	0.790	1.152×10^{-16}	0.089	3	2	T	0.662^t, 0.056^t, 0.049^t
B2-MM17	400 × 400	7	0.519	7.775×10^{-15}	0.017	1	0		0.513
C-W	17000 × 8000	7	3.160	1.910×10^{-18}	**0.035**	5	1	B	1.652^b, 0.680^b, 0.357, 0.253, 0.067
C-MM1	5900 × 3000	7	0.790	1.017×10^{-17}	**0.050**	1	1		0.735
C-N	10000 × 8800	7	3.837	4.457×10^{-18}	**0.023**	16	8	B	1.419, 0.752, 0.222, 0.193^b, 0.160, 0.160, 0.121, 0.093^b, 0.063, 0.039, 0.021 0.019, 0.018, 0.014, 0.009, 0.008
C-MM2	400 × 400	7	0.271	4.060×10^{-15}	0.014	1	0		0.268
C-MM3	5400 × 640	7	0.519	7.745×10^{-17}	0.034	1	0		0.496
C-MM4	2400 × 1400	7	0.361	5.620×10^{-17}	0.048	1	0		0.335
C-MM5	400 × 400	7	0.226	3.386×10^{-15}	0.017	1	0		0.223
C-MM6	4000 × 3700	7	0.745	1.255×10^{-17}	0.049	3	2	T	0.555^t, 0.078^t, 0.066^t
C-MM7	400 × 400	7	0.293	4.390×10^{-15}	**0.013**	1	0		0.290
E-MM1	23000 × 19000	7	6.207	6.515×10^{-19}	**0.033**	10	4	T	4.319^t, 0.165, 0.130^t, 0.130, 0.093, 0.085^t, 0.073, 0.043, 0.031, 0.031
E-MM2a	400 × 400	7	0.198	2.967×10^{-15}	**0.020**	1	0		0.196
E-MM2b	400 × 400	7	0.226	3.386×10^{-15}	**0.017**	1	0		0.224
E-MM2c	400 × 400	7	0.226	3.386×10^{-15}	**0.017**	1	0		0.224
E-MM2d	4200 × 2700	7	1.270	3.189×10^{-17}	0.026	1	0		1.224
E-MM3	400 × 400	7	0.226	3.386×10^{-15}	**0.017**	1	0		0.223
E-MM4	6900 × 5300	7	1.241	5.380×10^{-18}	0.047	1	0		1.127
E-MM5	7700 × 4600	7	1.185	5.645×10^{-18}	**0.048**	1	0		1.082
F-MM1	4800 × 2600	8	0.705	1.533×10^{-17}	0.121	5	3	B	0.396^b, 0.115, 0.074^b, 0.052, 0.018
F-MM2	2700 × 1600	8	0.339	3.620×10^{-17}	0.149	1	0		0.287

we perform additional simulations of a core which collapses to form a single star, then again it usually does so in most of the additional simulations (again typically 3 of the 4 additional simulations).

The reasons why we have not extended this procedure, by performing (say) five realisations of each Ophiuchus core, are twofold. First, this would take quite a long time and use quite a lot of computational resource. Second, there are other critical issues with the analysis which we have used to extract initial conditions from the quantities tabulated by André et al. (2007) (basically the formalism we have used for estimating the initial level of turbulence is incorrect, and – as we explain in Section 5.3.9 – tends to underestimate $\alpha_{\rm TURB}$ somewhat), and there are important additional aspects of the physics which we need to include in our model before we can expect the results to mimic reality (in particular radiative and mechanical feedback). We return to these issues at the end of the chapter.

In the meantime, we should simply be aware that the results presented here are probably less representative of what we can expect to happen in Ophiuchus during the next 300 kyr than we had originally intended. The results do nonetheless have a value, in that they indicate the sense in which the properties of a star might be expected to vary according to what sort of core that star is born in.

5.3.3 Star formation efficiency

Star formation in the Ophiuchus cores is predicted to be extremely efficient. Nearly all ($\sim$ 90%) of the core mass ends up incorporated into newly-formed stars. This high efficiency may be attributable to the fact that many of the cores are quite dense at the start of the simulations. The central densities range from $10^{-18}\,{\rm cm}^{-3}$ up to $10^{-15}\,{\rm cm}^{-3}$, and most of the cores start off significantly denser than the cores simulated in Chapter 4. Consequently, when a simulation is terminated after 300 kyr, even the outer parts of the core have had time to fall into the centre and accrete onto a star.

The core observations are necessarily biased towards regions of high volume- and column-density, and may therefore be failing to detect the lower-density regions which make up the outer parts of a core. Consequently the derived parameters of our core ensemble may reflect only the inner parts of cores, which inevitably collapse quickly and form protostars with high efficiency.

5.3.4 Cores producing single stars

73% of the cores spawn just a single star. Again this is partly because the cores start off at quite high density, $10^{-18}\,\mathrm{cm}^{-3}$ up to $10^{-15}\,\mathrm{cm}^{-3}$. Since the gas becomes optically thick and heats up adiabatically once the density rises above $10^{-14}\,\mathrm{cm}^{-3}$ to $10^{-12}\,\mathrm{cm}^{-3}$ (depending on the mass of the condensation involved), the approximately isothermal collapse phase has a rather short dynamic range. Hence, by the time the core becomes adiabatic, its linear size has only decreased by a small factor, and consequently there has not been much opportunity for initial density structures to be amplified by self-gravity.

The preponderance of single stars can also be attributed to the fact that initial levels of turbulence are generally low, and therefore there is not much density structure for self-gravity to amplify. Values of α_{TURB} range from 0.009 up to 0.149, with an average value of $\bar{\alpha}_{\mathrm{TURB}} = 0.03$; in contrast, in Chapter 4 we performed simulations with $\alpha_{\mathrm{TURB}} =$ 0.05, 0.10, and 0.25.

Finally, many of the cores have extremely low masses, and therefore it is hard for them to find sufficient mass to form more than one star.

5.3.5 Cores producing more than one star

27 % of the cores in the Ophiuchus ensemble form more than one star. These appear to be the cores which have high total mass (M_{TOT}), and/or high initial turbulence (α_{TURB}),

and/or low initial density (ρ_0). This is presumably because high-mass cores have the material to form many stars. If they have a high initial level of turbulence they develop a lot of substructure which can then be amplified by self-gravity to form separate protostars. And if they start off at low initial density, then there is a large dynamic range of approximately isothermal collapse during which self-gravity can amplify these substructures.

There are three parameters, and there are small numbers, so looking for correlation is not straightforward. We start by considering each parameter in turn, and then try to combine them.

Fig. 5.3 shows a plot of the total number of stars formed in a core, $N_\star$, against the total core mass, $M_{\rm TOT}$. From this plot we see that less than 23 % of cores with $M_{\rm TOT} < 1.4\,{\rm M}_\odot$ form more than one star, whereas 100 % of cores with $M_{\rm TOT} > 1.4\,{\rm M}_\odot$ form more than one star. This corroborates the conclusion of Hubber (2006) who showed that if the initial level of turbulence is held fixed at $\alpha_{\rm TURB} = 0.2$, a core with mass $M_{\rm TOT} = 4.34\,{\rm M}_\odot$ produces more stars than a core with mass $M_{\rm TOT} = 2.17\,{\rm M}_\odot$. It is appropriate to pre-empt our overall conclusion by pointing out that the cores with relatively low masses which nonetheless form more than one star tend to have quite high initial levels of turbulence and/or low initial density.

Fig. 5.4 shows a plot of the total number of stars formed in a core, $N_\star$, against the initial level of turbulence, $\alpha_{\rm TURB}$. From this plot we see that a core with high $\alpha_{\rm TURB}$ is more likely to form more than one star than a core with low $\alpha_{\rm TURB}$. For example, less than 29 % of cores with $\alpha_{\rm TURB} < 0.06$ form more than one star, whereas nearly 67 % of cores with $\alpha_{\rm TURB} > 0.06$ form more than one star. Again we pre-empt our overall conclusion by pointing out that the cores with relatively low turbulence which nonetheless form more than one star have quite high masses and/or low initial densities. It is important to mention here that only a small fraction of cores have initial levels of turbulence greater than $\alpha_{\rm TURB} < 0.06$, and so we must be careful not to place to much weighting on this conclusion.

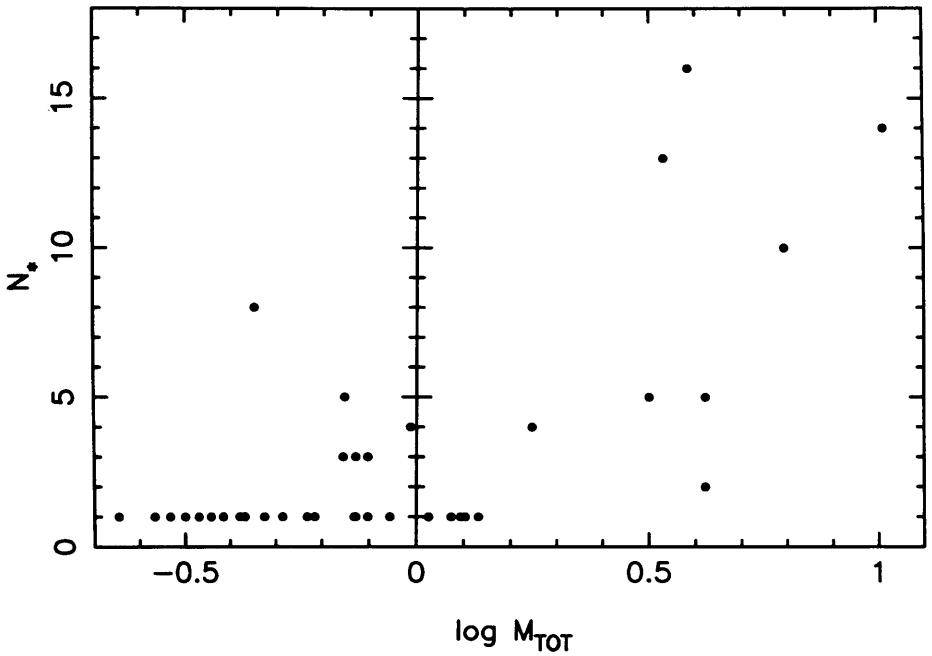

Figure 5.3: Logarithm of the total mass of a core ($M_{\rm TOT}$) plotted against the number of stars formed, $N_\star$.

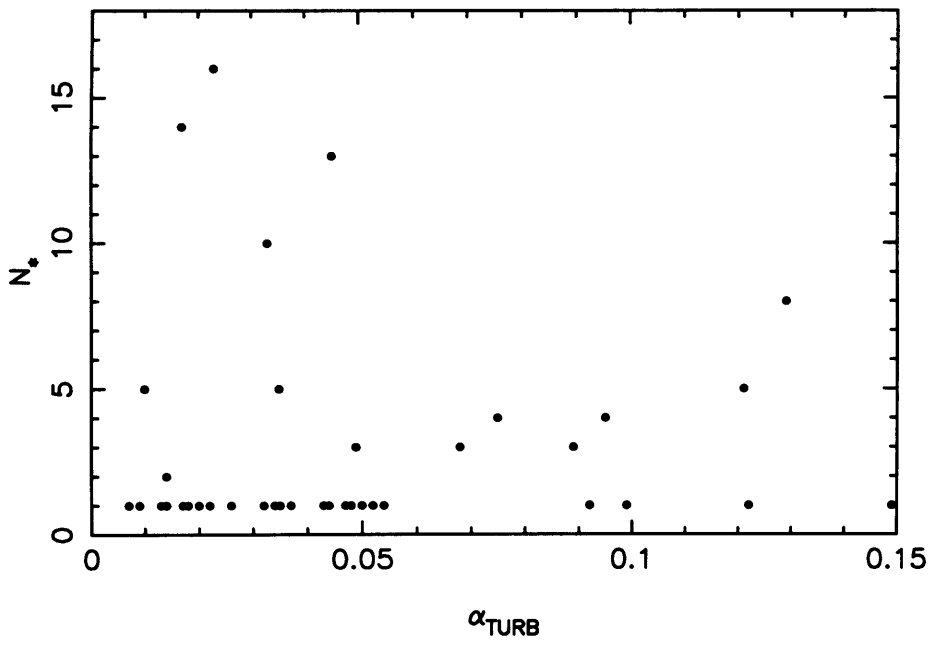

Figure 5.4: For each simulation, we plot the logarithm of the initial level of turbulence in the core ($\alpha_{\rm TURB}$) against the number of stars formed ($N_\star$.)

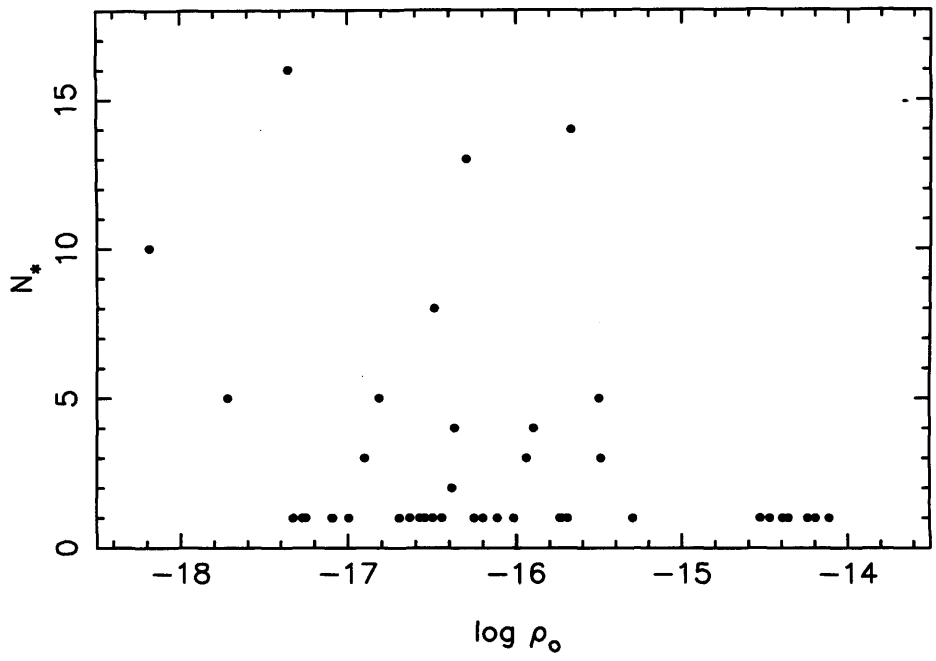

Figure 5.5: We plot the logarithm of the central core density, $\bar{\rho}_o$ for the number of stars formed, $N_\star$

Finally Fig. 5.5 shows a plot of the total number of stars formed in a core, $N_\star$, against the initial central density, ρ_0. From this plot we see that firstly there is a very weak correlation, in that a core with low ρ_0 may be more likely to form more than one star than a core with high ρ_0. For example, nearly 44 % of cores with $\rho_0 < 4 \times 10^{-16}$ g cm^{-3} form more than one star, whereas no core with $\rho_0 > 4 \times 10^{-16}$ g cm^{-3} forms more than one star. However, this is a very weak correlation, and many more simulations are required to see if this conclusion is still valid.

It would be very useful to formulate these trends more precisely, using Principal Component Analysis, and it is our intention to do this when we have assembled better statistics. For the time being we have experimented with combining the different factors to create a single parameter thus:

$$\mathcal{M} = \left(\frac{\alpha_{\rm TURB}}{0.06}\right)^2 + \left(\frac{M_{\rm TOT}}{1.2}\right)^1 + \left(\frac{14 + \log_{10}(\rho_{\rm O})}{3}\right)^2 . \qquad (5.13)$$

Fig. 5.6 shows a plot of the total number of stars formed in a core, $N_\star$, against

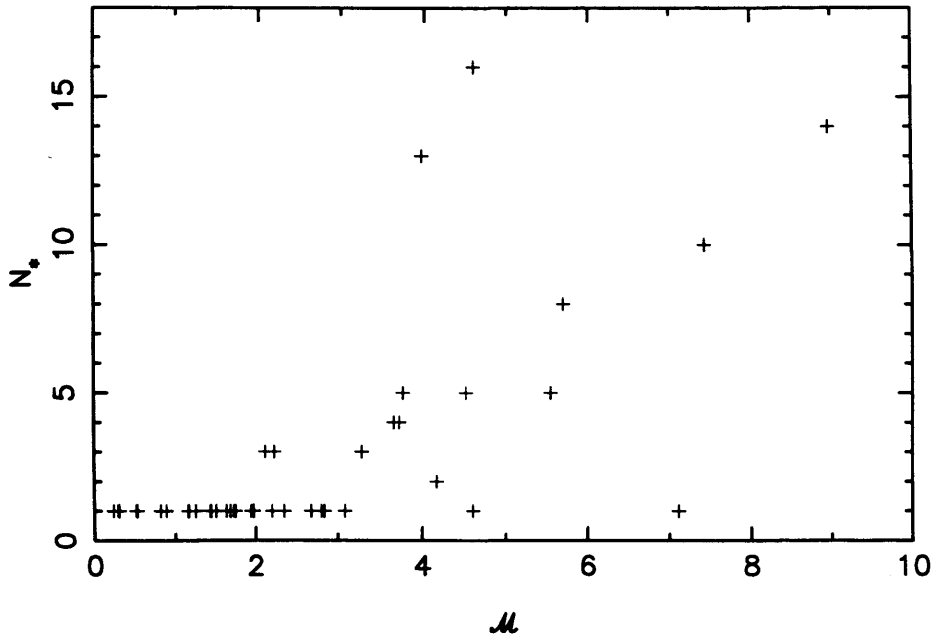

Figure 5.6: Total number of stars formed in a core, $N_\star$, against the parameter $\mathcal{M}$.

$\mathcal{M}$. We see that there is a correlation, in the sense that cores with small $\mathcal{M}$ tend to spawn a single star, and cores with large $\mathcal{M}$ tend to spawn more than one star. There is potentially an interesting theorem here, which we will try to establish in the future. In the meantime, there does not seem to be a link between the positions of the cores in Fig. 5.6 and the clump that they belong to. Repeated simulations will hopefully confirm if this is indeed the case.

5.3.6 The role of disc fragmentation

In the cores that form more than one star, we frequently observe the same pattern as was noted in Chapter 4, viz. a primary star forms from the material with lower angular momentum, and then the material with higher angular momentum accumulates into a circumprimary disc. The disc grows in mass until it becomes Toomre unstable, and then fragments to produce one – or usually several – secondaries; the time taken for the disc to accumulate and then fragment is typically $\sim$ 20 kyr. Some of the secondaries that form in a disc are unable to accrete much mass before they are ejected, and so they end

up as brown dwarfs or very low-mass hydrogen-burning stars. Other secondaries remain in the disc and accrete sufficient mass to become comparable in mass with the primary; sometimes they even grow more massive than the primary.

Fig. 5.7 shows the collapse and fragmentation of the core A-MM4 in Oph-A. This core collapses to form a primary star, and then a circumprimary disc accumulates and fragments to produce seven companions, of which six are brown dwarfs.

Fig. 5.8 illustrates the accretion histories for a sample of simulations. The trends seen here are very similar to those discussed in Chapter 4. We see that there is sometimes – although not always – a significant delay between the formation of the primary star and the formation of the second star. During this delay, the circumprimary disc grows in mass until it is Toomre unstable. Secondary stars then condense out of this disc in quick succession.

5.3.7 The stellar mass distribution

Fig. 5.9 shows the mass distribution for the stars formed in our ensemble of cores in the Ophiuchus Main Cloud. As in Section 4.4.3, the black line shows the histogram obtained by distributing the final stellar masses into 15 logarithmic bins which are equally spaced in the interval

$$-2 \leq \log_{10}\left(\frac{M_\star}{\mathrm{M}_\odot}\right) \leq 1,$$

so that $\Delta \log_{10}(M_\star) = 0.2$. The red line shows the mass distribution obtained when each stellar mass is smoothed using a Gaussian smoothing kernel with adaptive smoothing lengths dictated by the separation between neighbouring masses. Both the histogram, and the smoothed distribution, are normalised, in the sense that

$$\int_{M=0}^{M=\infty} p_{\log_{10}(M)}\, d\log_{10}(M) = 1. \qquad (5.14)$$

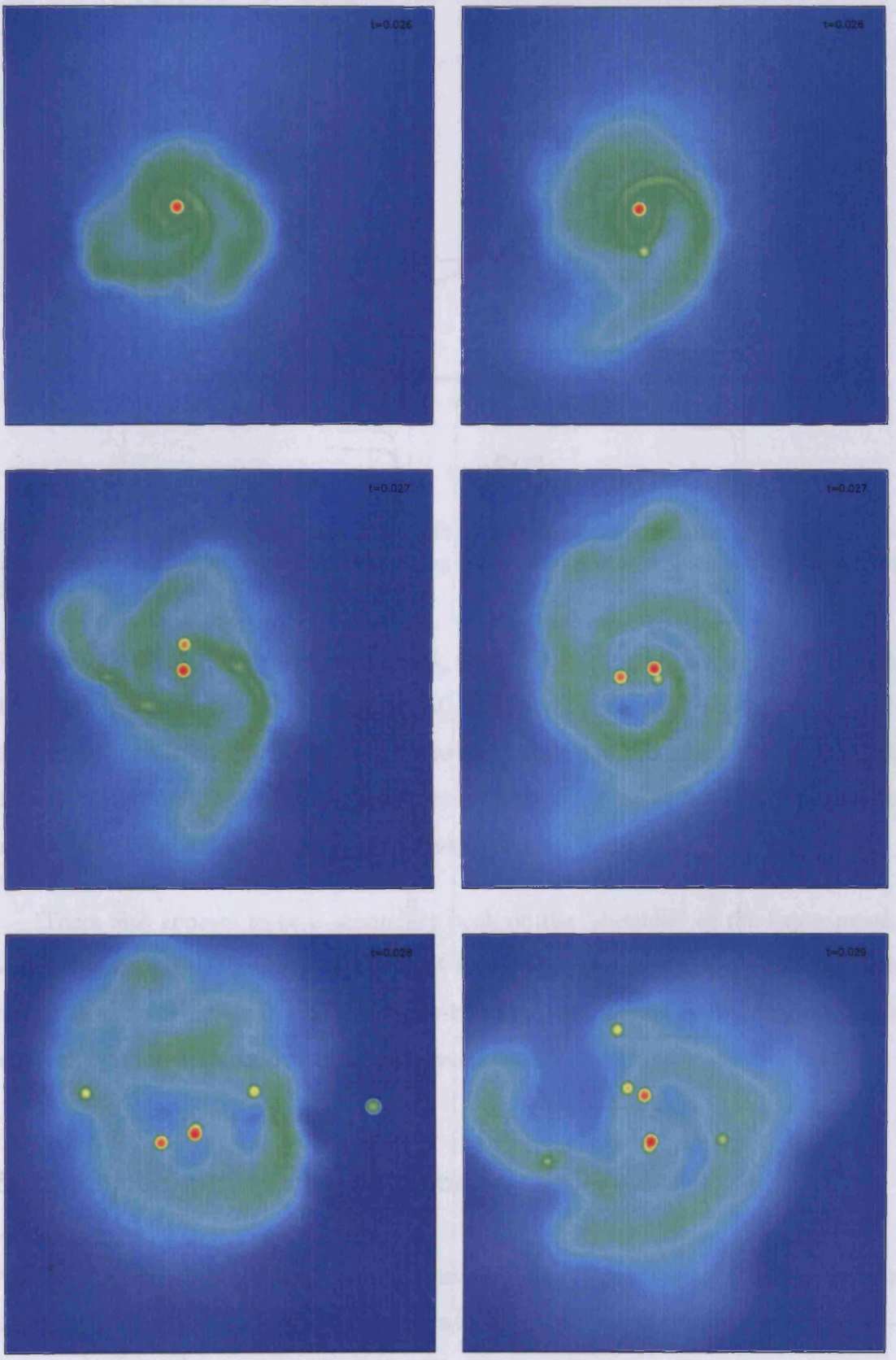

Figure 5.7: Simulation of the collapse and fragmentation of a the A-MM4 core in Oph-A. Each snapshot shows the logarithm of the column density.

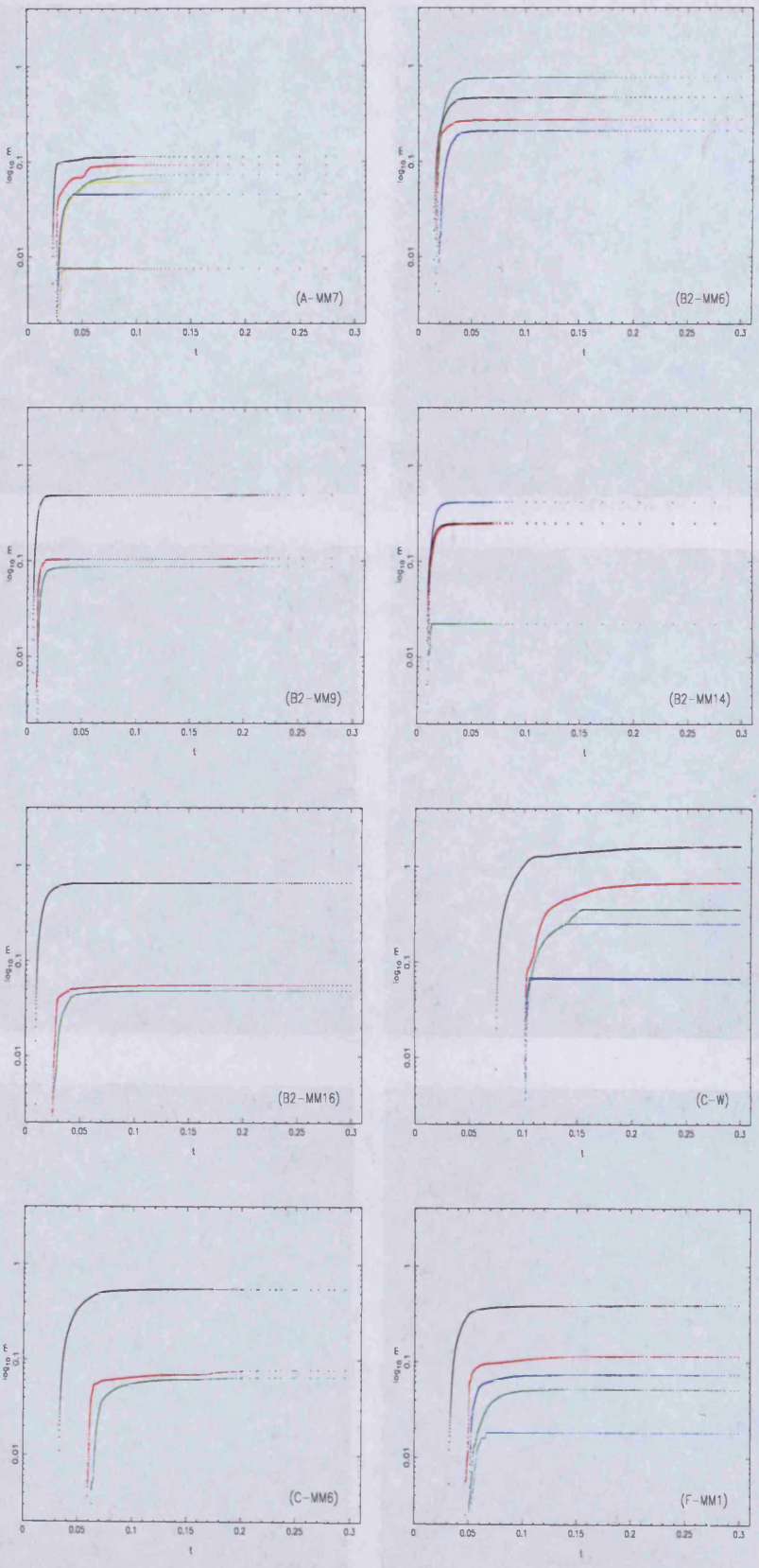

Figure 5.8: Stellar masses as a function of time (Myr), for a selection of simulations.

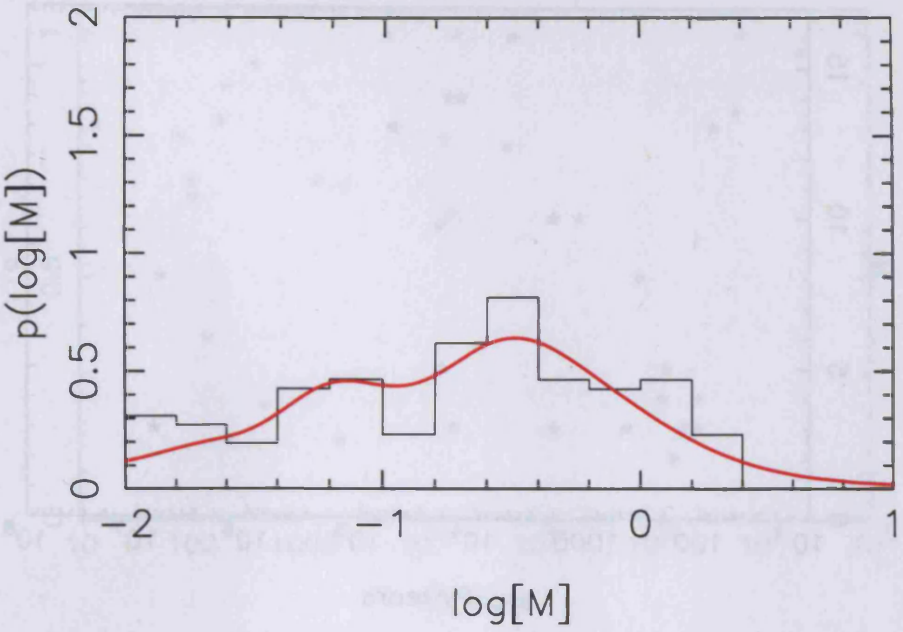

Figure 5.9: Normalised stellar mass distribution. The black lines are histograms of the raw data and the red lines are obtained by smoothing with a Gaussian smoothing kernel (see text for details).

The mass distribution shows one major peak, comprising masses in the range 0.1 to 0.6 $M_{\odot}$. This peak is made up of the the majority of single stars produced from the cores. With the exception of a few cores, the typical mass of a core is in this range. Due to the high density of the cores, nearly all the mass, even in the outer parts, has sufficient time to accrete onto the central star before the simulation is terminated.

There also appears to be a secondary peak on the 'shoulder' of the larger mode, with masses concentrated in the range 0.04 to 0.1 $M_{\odot}$. This secondary peak comprises brown dwarfs and very low-mass hydrogen-burning stars, formed by disc fragmentation and then ejection before they can accrete much mass.

5.3.8 Stellar multiplicity statistics

A small number of cores in each clump form multiple systems, mainly binary and triple systems. To calculate their multiplicity statistics, we take the same approach as in Sec-

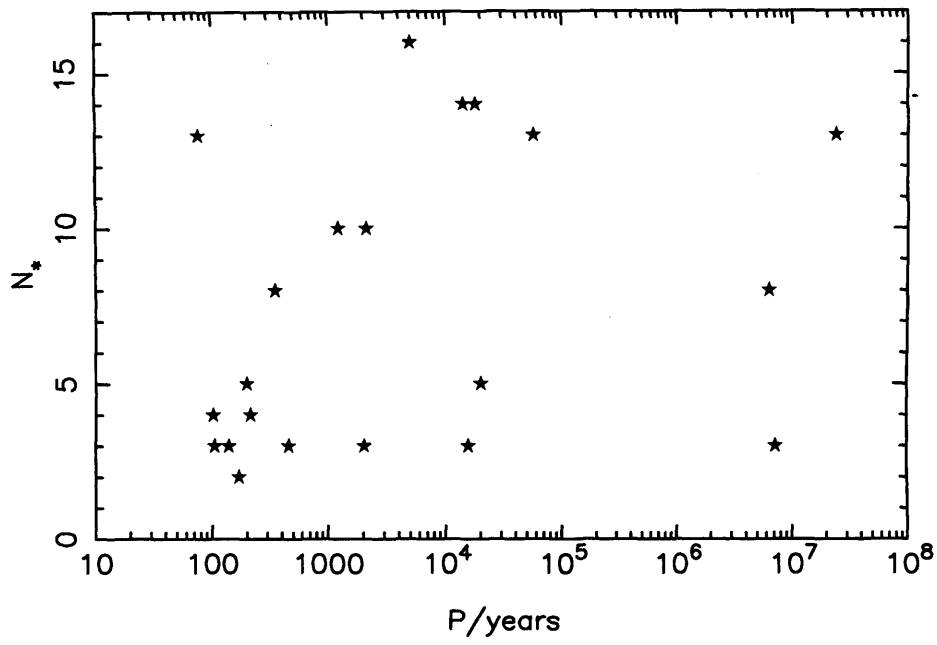

Figure 5.10: For each multiple system, we plot the number of stars formed in that simulation, $N_\star$, against the period, P.

tion 4.4.5, where we have assumed that all multiple systems are hierarchical. In this situation, we compute the two periods for a triple system by finding the period for the pair with the greatest specific binding energy. We then treat this pair as a single star and find the period of its orbit relative to the third star.

Fig.5.10 shows the number of stars formed in a simulation plotted against the periods of the multiple systems identified at the end of the simulations. The period distribution has a mean $\mu_{\log_{10}(P)} \simeq 3.2$, with periods ranging from 10^2 yrs to 10^8 yrs. There appears to be no obvious dependence of the period distribution on the number of stars formed.

Fig.5.11 shows the distribution of orbital eccentricity (e) plotted against period (P) at the end of the simulations. It is clear that the eccentricities of the multiple systems are not strongly correlated with their periods. However, the distribution of eccentricities is similar to the distribution obtained using the new treatment of the energy equation in Chapter 4 (see Fig. 4.12). The protostars in a majority of systems tend to be on highly elliptical orbits ($e > 0.5$). Only 4 of the 21 multiple systems have eccentricities

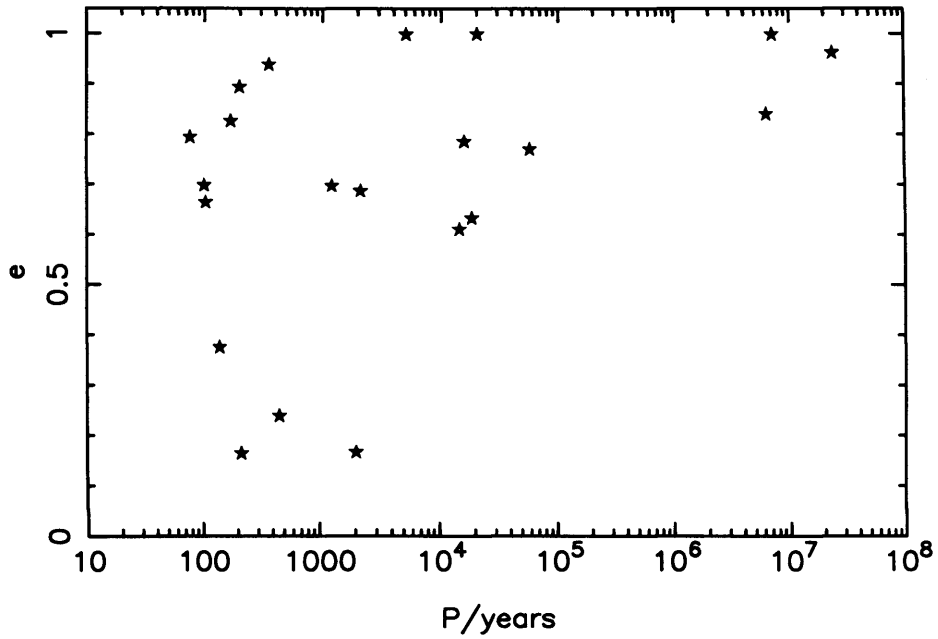

Figure 5.11: For each multiple system we plot the orbital eccentricity, e against the period, P.

of $e < 0.4$. In section 4.4.5, less than 6% of the distribution have $e \lesssim 0.2$.

Unlike the binary systems discussed in Chapter 4, we do not see any substantial evidence for the equalisation of mass. This is illustrated in Fig. 5.12, which shows the distribution of mass ratios, $q \equiv M_2/M_1$, for each of the multiple systems detected at the end of the simulations. The distribution is skewed towards systems in which the components differ in mass by almost a factor of ten. One thought is that this could be due to the difference in the power law of the density profile used here (Equation 5.1) and that in Chapter 4 (Equation 4.4). However, future work on the effect of the initial conditions on q is required to clarify this.

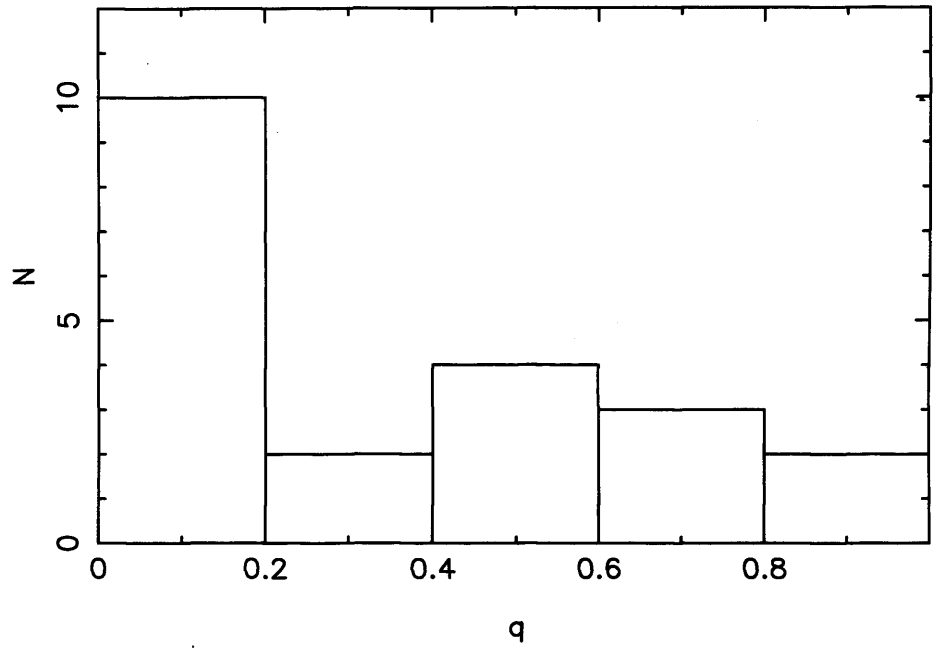

Figure 5.12: The distribution of mass ratios, q, for multiple protostars at the end of the simulations.

5.3.9 Revised initial conditions

Initial level of turbulence

Equation (5.11) is only valid, if we adopt the temperatures (and hence the thermal energies) used by André et al. (2007). Since we have actually used the significantly lower temperatures estimated by Stamatellos et al. (2007c), it is necessary to allow for the fact that now a much larger fraction of the FWHM of the observed N_2H^+ lines has to be attributed to non-thermal motions.

The turbulent energy is

$$E_{\rm TURB} = \frac{3\,M\,\sigma_{\rm NT}^2}{2}, \tag{5.15}$$

and the thermal energy is

$$E_{\rm THERM} = \frac{3\,M\,\sigma_{\rm T}^2}{2}, \tag{5.16}$$

where σ_{NT} and σ_T are – respectively – the non-thermal and thermal velocity dispersions, as defined by André et al (2007). In particular, σ_T is the thermal velocity dispersion for a particle with the mean gas-particle mass, i.e.

$$\sigma_T = \left(\frac{k_B T}{\bar{m}}\right)^{1/2} . \tag{5.17}$$

The non-thermal velocity dispersion is obtained from the *FWHM* of the fitted N_2H^+ lines, which is given by

$$FWHM^2 = 8 \ln(2) \left(\sigma_{NT}^2 + \sigma_{TM}^2\right) . \tag{5.18}$$

Here σ_{TM} is the thermal velocity dispersion for an N_2H^+ molecule, i.e.

$$\sigma_{TM} = \left(\frac{k_B T}{m_M}\right)^{1/2} , \tag{5.19}$$

where $m_M = 29 m_p$ is the mass of an N_2H^+ molecule.

It follows that the turbulent energy is given by

$$E_{TURB} = 3 \times 10^{43} \text{ erg} \left(\frac{M}{M_\odot}\right) \left\{\left(\frac{FWHM}{2.355 \text{ km s}^{-1}}\right)^2 - \left(\frac{T}{3488 \text{ K}}\right)\right\} . \tag{5.20}$$

Similarly the thermal energy is given by

$$E_{THERM} = \frac{3 M k_B T}{2 \bar{m}} \simeq 36 \times 10^{43} \text{ erg} \left(\frac{M}{M_\odot}\right) \left(\frac{T}{3488 \text{ K}}\right) , \tag{5.21}$$

and hence

$$\frac{\alpha_{TURB}}{\alpha_{THERM}} = \frac{E_{TURB}}{E_{THERM}} \simeq \left\{\left(\frac{FWHM}{2.355 \text{ km s}^{-1}}\right)^2 - \left(\frac{T}{3488 \text{ K}}\right)\right\} \left\{12 \left(\frac{T}{3488 \text{ K}}\right)\right\}^{-1} . \tag{5.22}$$

As examples of how this revised analysis affects the estimated levels of turbulence, we recalculate $\alpha_{TURB}/\alpha_{THERM}$ for three of the Ophiuchus cores. These three are chosen to

Table 5.3: Sample of recalculated values of $\alpha_{\rm TURB}/\alpha_{\rm THERM}$.

CORE	$\left(\frac{\alpha_{\rm TURB}}{\alpha_{\rm THERM}}\right)_{\rm USED}$	$\left(\frac{\alpha_{\rm TURB}}{\alpha_{\rm THERM}}\right)_{\rm CORRECTED}$
B2-MM1	0.09	1.0
A-MM4	0.49	1.65
B2-MM11	1.69	7.68

be representative of the range of values spanned by Ophiuchus cores.

Since the corrected levels of turbulence are always significantly higher than those we have used, we should expect that simulations using these corrected levels of turbulence will result in many fewer cores producing just a single star. We have repeated a small number of simulations with the correct levels of turbulence and can confirm that this is the case, in the sense that each core produced more than one star in the sample of 3 test cases that we used. However, more simulations are required before we can can confirm that this result is statistically sound.

Initial aspect ratio

Our simulations may also be compromised by the assumption of spherical symmetry. Some cores have rather low aspect ratios, $\mathcal{R} = a/b$. For example, SM-1 has projected FWHM dimensions $a = 6200$ AU and $b = 2100$ AU, hence $\mathcal{R} = 0.34$. Similarly, C-W has $a = 17000$ AU and $b = 8000$ AU, hence $\mathcal{R} = 0.47$.

The main difficulty here is that the intrinsic shape of a core is three dimensional, but we only see them in projection; the intrinsic aspect ratios are in general more extreme than the projected ones. We are looking into ways of de-projecting the observed core shapes to obtain – in a statistical sense – estimates of the intrinsic ellipsoidal axes, $(a_{\rm o}, b_{\rm o}, c_{\rm o})$, so that we can explore the effect of starting simulations with a density profile

of the form

$$\rho(x,y,z) = \rho_0 \left\{ 1 + C \left(\frac{x^2}{a_0^2} + \frac{b_0^2}{b_0^2} + \frac{c_0^2}{c_0^2} \frac{z^2}{c_0^2} \right) \right\}^{-1} . \quad (5.23)$$

Goodwin et al. (2002) have analysed the three dimensional shapes of cores in nearby star forming regions, and find that starless cores appear to be more flattened than protostellar cores. It will be interesting to see whether this finding is reproduced by our simulations, and whether elongated cores produce multiple systems, as has been suggested by the classical work of Bonnell et al. (1991) and Nelson & Papaloizou (1993).

5.3.10 Additional constitutive physics

A number of potentially important physical effects have not been included in our models. In particular, no account has been taken of feedback from the stars that form. Such feedback might be either radiative, or mechanical, or both. Nor do we include magnetic fields. We briefly discuss how these effects might be included in future work.

Radiative feedback

It is relative straightforward to include radiative feedback from the stars that form in the simulation, provided an expression can be formulated for the intrinsic luminosity of a newly-formed star. This must include the intrinsic luminosity, due to internal contraction, plus the luminosity generated by accretion. Both these can be computed using simple phenomenological models, provided the code is able to estimate the accretion rate (i.e. by smoothing over the arrival of individual SPH particles).

Radiative feedback will heat the surrounding gas and dust, and this is expected to

suppress fragmentation of the inner circumprimary disc (see Whitworth & Stamatellos 2006). Thus the circumprimary disc will probably have to accumulate for longer before it becomes Toomre unstable. As a result, the primary will become more massive by accreting the material in the inner accretion disc (the material which cannot fragment). Once the circumprimary discs does become sufficiently massive and extended to be Toomre unstable and fragment, it will spawn fewer stars and they will tend to be somewhat more massive.

Mechanical feedback

Mechanical feedback can also be modelled using a simple phenomenological prescription, as has been shown by Stamatellos et al. (2005). Each time two additional SPH particles have been assimilated by a sink, they are re-injected into the surrounding gas with one tenth the mass that they came in with, and with equal and opposite velocities of magnitude $100\,\mathrm{km\,s^{-1}}$, directed along the spin axis of the sink. This prescription exploits the observational and theoretical rule-of-thumb that the mass-loss rate is roughly one tenth of the accretion rate (e.g. Pudritz 2003). (This prescription has the added advantage that it obviates the need to de-allocate the memory used for SPH particles assimilated by a sink.)

Our expectation is that mechanical feedback will both delay star formation, and reduce the efficiency of star formation.

Magnetic fields

The existing Cardiff SPH code for handling non-ideal MHD effects is of limited use, because it does not include divergence cleaning (therefore it cannot handle problems with large dynamic range), and it is not parallelised (therefore it can only operate with small numbers of particles). We have been rewriting and testing this code, but the new

version is not yet in a state to use for this project.

The consequences of introducing magnetic fields are hard to predict. Our suspicion is that it will reduce the efficiency of fragmentation, resulting in fewer stars, and in particular fewer brown dwarfs. However, there is an even more fundamental problem, and that is that the initial and boundary conditions for the magnetic field are even less tightly constrained than those for the density and temperature field. Furthermore, if non-ideal effects are to be captured, then the treatment of the energy equation must be extended to include the ionisation balance. This is being done by Whitworth (private communication), but the module is not yet available.

5.4 Summary

We have modelled the evolution of the ensemble of prestellar cores observed in the Ophiuchus Main Cloud. The initial conditions for each core have been set up using the revised temperatures and adjusted masses of Stamatellos et al. (2007c), and the sizes and levels of turbulence measured by Motte et al. (1998) and André et al. (2007) (but see below). The main results are summarised as follows.

- The cores in the Main Cloud are likely to collapse and form typically a single star, on a timescale of 10 to 100 kyr. We find that star formation in these cores is extremely efficient. This is probably due to the fact that the initial central densities of the simulated cores are so high that, by the time the simulation is completed after 300 kyr, even the gas in the outer parts has accreted onto the central star.

- Some cores (15 out of 48) form multiple systems, with as many as 16 stars forming in one particularly prolific core. In these cores, once a primary star has formed from the material with low angular momentum, the material with higher angular momentum forms a circumstellar disc around the primary. This disc normally

grows in mass until it becomes Toomre unstable and fragments to form multiple secondaries.

- The number of stars formed by a core is highest if the core has high mass. There is also a much weaker dependence on the initial level of turbulence and the initial density, in that there tends to be more stars formed by a core if it has a high initial level of turbulence, and/or if it starts from a low initial density. We explain why, and derive a parameter $\mathcal{M}$ (see Equation 5.14) which combines all these dependencies. It is important to stress that these conclusions are based on small statistics, and so require further investigation.

- There are 21 multiple systems formed in this ensemble of simulations. Most of these multiple systems have highly eccentric orbits ($e > 0.5$). This is in agreement with our findings in Chapter 4.

- Our simulations do not take account of radiative or mechanical feedback from the stars that form (in particular, from the primary star in simulations that form more than one star). We predict that the inclusion of feedback would reduce the high efficiency of star formation we have reported here. We have also assumed spherical symmetry in the initial cloud, which may be unrealistic for many of the cores in the Ophiuchus ensemble. Finally we note that the levels of turbulence we have invoked need to be revised upwards in order to be properly compatible with the observations.

5.5 Future work

We plan to repeat these simulations using revised values for the initial levels of turbulence. We will also look into ways of reproducing the observed projected shapes –in some statistical sense – with triaxial ellipsoidal initial shapes. We will include radiative and mechanical feedback in our simulations to ascertain what effect they have on the

efficiency of star formation and the properties of the stars formed. Ultimately we would also like to include the magnetic field. These revisions will all be introduced incrementally, so that we are able to track cause and effect. We will also seek to improve the statistics of our results by performing multiple realisations of the turbulent velocity field and/or the de-projected three-dimensional shape.

Chapter 6

The effect of metallicity on the binary frequency

In this chapter we take a simplified look at the effect metallicity has on the collapse and fragmentation of low mass cores. Machida (2008) recently modelled the evolution of star-forming clouds for various metallicities and found that the binary frequency increases as cloud metallicty lowers, and binary separations in lower metallicity clouds are on average shorter than in higher metallicity clouds. His simulations support recent observations made by Lucatello et al. (2005). We revisit this study but instead perform simulations of relatively isolated, low turbulence, low-mass cores. We compute the statistical properties of the resulting stars, in particular the mass distribution and binary properties, to compare with the findings of Machida (2008).

6.1 Introduction

To describe the elemental composition of a star, we use X to represent the fraction by mass of hydrogen, Y to represent the fraction by mass of helium, and Z to represent the mass of the other (in general, heavier) elements such as oxygen, carbon and nitrogen. Z

is often referred to as the metallicity, and

$$X + Y + Z = 1\,. \tag{6.1}$$

The Sun, a Population I star, has an elemental composition of $X = 0.70$, $Y = 0.28$, and $Z = 0.02$, and is referred to as metal-rich. Population I stars are relatively young stars which have formed in the last few Gyrs. They are typically found in the disc of a galaxy.

Stars which formed very early in the Universe are termed Population III. Numerical simulations of the collapse and fragmentation of primordial clouds indicate that these stars were rather massive, with masses $\gtrsim 20\,M_\odot$ (Bromm et al. 2002), and had zero metallicity ($Z = 0$). No Population III star has ever been identified; if their masses were $\gtrsim 20\,M_\odot$ they must have burnt out long ago. However, recently a number of extremely metal-poor stars have been observed in the Galactic halo (Christlieb et al. 2001, Frebel et al. 2005). These include HE 0107-5240 and HE 1327-2326 which have [Fe/H] $\lesssim -5$ (i.e. iron mass fraction $\sim 5 \times 10^{-6} Z_\odot$)

6.1.1 Binary Frequency

It is thought that the binary frequency in the early universe was higher than that observed today. Currently, 60% of young, low-mass stars in the field are in binary or higher-order multiple systems (Duquennoy & Mayor 1991). Lucatello et al. (2005) examine the radial velocities of a sample of carbon-enhanced, very metal-poor s-process-rich stars (CEMP-s), and find that the binary fraction among these stars is higher than that found in the field. Based on the fact that only a small fraction of these CEMP-s can be detected, it is possible this fraction could be higher ($\lesssim 100\%$). Lucatello et al. (2005) also find that the binary separations of the stars are shorter than those of field stars.

Numerical simulations aiming to support this idea have recently been performed by Machida (2008). He follows the evolution of rotating clouds with an initial ratio

of rotational to gravitational energy $\beta_o = 10^{-1} - 10^{-6}$ and metallicity $Z = 0 - Z_\odot$. He finds that cloud rotation promotes fragmentation, whilst fragmentation is suppressed in clouds with higher metallicity. In the clouds that form multiple sysytems, he finds that the binary frequency is a decreasing function of cloud metallicity. In addition, the binary stars that form from low metallicity clouds have shorter orbital periods than those from high metallicity clouds.

6.1.2 The effect of metallicity

Bromm et al. (2001) have studied the effect of metallicity on the evolution of the gas in a collapsing dark matter mini-halo. They simulate two scenarios, one with a gas of metallicity $Z = 10^{-4} Z_\odot$, and the other with a gas of metallicity $Z = 10^{-3} Z_\odot$. They adopt a cooling function that takes into account the metal-line cooling, but assume that cooling from molecular hydrogen is negligible in this scenario and so do not treat it. They find that the gas with the lower metallicity fails to undergo continued collapse and fragmentation. In contrast, the gas with the higher metallicity collapses to form a disc-like structure, which then becomes gravitationally unstable and undergoes fragmentation forming a large number of high-density clumps. Therefore, Bromm et al. (2001) propose that there exists a critical metallicity, $Z_{\rm CRIT} = 5 \times 10^{-4} Z_\odot$, below which the presence of heavy elements does not greatly affect the outcome.

Jappsen et al. (2007) have simulated the collapse of warm ionised gas in small protogalactic halos. They find that at low metallicities ($Z < 10^{-3} Z_\odot$) metal-line cooling has an almost negligible effect on the evolution of low-density gas. At this stage, molecular hydrogen dominates the cooling of the gas, and so it is the amount of H_2 formed that determines whether or not the gas can collapse and form stars.

In this chapter we revisit the work of Machida (2008) regarding the effect of various metallicities on the binary frequency, by simulating the collapse and fragamentation of low-mass, low-turbulence prestellar cores, rather than molecular clouds. Machida im-

poses a $m = 2$ density perturbation to induce fragmentation, but this is not the approach we take with our cores. Since we do not incorporate the cooling due to molecular hydrogen in our simulations, we model metallicities $Z = Z_\odot$, $Z = 0.1\,Z_\odot$ and $Z = 0.01\,Z_\odot$. With these metallicities, the gas is sufficiently cool that H_2 cannot contribute to the cooling, since para-H_2 has its first excited level ($J = 2$) at $k_B(512\,\mathrm{K})$, and ortho-H_2 has its first excited level ($J = 3$) at $k_B(854\,\mathrm{K})$ (e.g. Black & Bodenheimer 1975). With the sink density we use here ($\rho_{\mathrm{SINK}} = 10^{-11}\,\mathrm{g\,cm^{-3}}$), the gas temperature rarely rises above $\sim 200\,\mathrm{K}$ and therefore the rotational levels of molecular hydrogen are not strongly excited. At metallicities $10^{-3}\,Z_\odot$ and below, cooling due to molecular hydrogen becomes important (Jappsen et al. 2007), hence we do not perform simulations with metallicities below $0.01\,Z_\odot$.

We examine the effect that reducing the metallicity has on the number of binary systems formed and their separations. We compare our findings with those of Machida (2008) and the observations of low metallicity stars made by Lucatello et al (2005).

6.2 Initial conditions

We use the same initial conditions as those described in Chapter 4, which are designed to fit the observed properties of prestellar cores. We adopt a Plummer-like density profile

$$\rho(r) = \frac{\rho_{\mathrm{KERNEL}}}{(1 + (r/R_{\mathrm{KERNEL}})^2)^2}\,. \tag{6.2}$$

Here $\rho_{\mathrm{KERNEL}} = 3 \times 10^{-18}\,\mathrm{g\,cm^{-3}}$ is the central density, and $R_{\mathrm{KERNEL}} = 5,000\,\mathrm{AU}$ is the radius of the central region within which the density is approximately uniform. The core extends out to $R_{\mathrm{CORE}} = 50,000\,\mathrm{AU}$, so its total mass is $M_{\mathrm{CORE}} = 5.4\,\mathrm{M}_\odot$ and the density at the boundary of the core is 10^4 times lower than at the centre. We set the initial temperature of the gas to be $T = 10\,\mathrm{K}$.

As in Chapter 4, we impose an initial divergence-free Gaussian random velocity field on each core. The power spectrum of this velocity field is set to be $P_k dk \propto k^{-4} dk$, and we consider an initial level of turbulence

$$\alpha_{\rm TURB} \equiv \frac{E_{\rm TURB}}{|E_{\rm GRAV}|} = 0.25 . \quad (6.3)$$

6.2.1 Metallicities

To treat the energy equation and associated radiative transport, we use the technique described in Section 4.2.2. Since metals make very small contributions to the equation of state, we assume the gas is 70% hydrogen and 30% helium by mass (i.e. $X = 0.70$, $Y = 0.30$, and $Z = 0$.) for the purpose of treating the gas-phase chemistry. However, metals make a substantial contribution to the opacity, particularly at low temperatures where dust dominates the opacity, and so to model cores of different metallicities we must adjust the opacity accordingly. Depending on what factor we are reducing the metallicity by, we reduce the opacity in the same way. The opacities in our code are evaluated once and for all time, and stored in a dense look up for reference and interpolation.

6.2.2 Numerical details

The cores are set up in the same way as those in Section (4.3.1), by cutting out a sphere of 25,000 particles from a settled uniform-density cube, and stretching it radially to produce a Plummer-like profile (Equation 6.2).

To identify stars that form, we invoke sink particles (see Section 2.10 for a description), adopting a sink density threshold $\rho_{\rm SINK} = 10^{-11}$ g cm^{-3} and radius $\rho_{\rm SINK} = 5$ AU.

To account for the chaotic nature of the turbulent velocity field that we impose on the cores, we must simulate multiple realisations. Therefore, we perform an ensemble

Table 6.1: Results of the simulations performed with metallicities $Z = Z_\odot$, $Z = 0.1\,Z_\odot$ and $Z = 0.01\,Z_\odot$, at time $t = 0.3$ Myr. See text for a description of each column.

ID	$Z/Z_\odot$	$\sum\{M_*\}/M_\odot$	N_*	N_{BD}	Mult	$M_*/M_\odot$
T041	1.0	3.369	7	2	BT	0.821^t, 0.809^t, 0.782^b, 0.778^b, 0.138^t, 0.025, 0.016
T042	1.0	3.055	4	0	T	1.083^t, 0.932^t, 0.913^t, 0.127
T043	1.0	3.306	9	3	BT	0.798^t, 0.586^b, 0.585^b, 0.494^t, 0.488^t, 0.271, 0.039, 0.033, 0.012
T044	1.0	3.260	14	8	BB	0.763^{b1}, 0.762^{b1}, 0.462^{b2}, 0.450^{b2}, 0.426, 0.235, 0.054, 0.032, 0.025, 0.016, 0.010, 0.009, 0.008, 0.008
T045	1.0	3.193	13	4	TQ	0.444^q, 0.438^q, 0.379^t, 0.378^t, 0.368^t, 0.342^q, 0.340^q, 0.332, 0.081, 0.034, 0.031, 0.018, 0.008
T046	1.0	3.362	5	0	T	0.853, 0.768^t, 0.768^t, 0.573^t, 0.400
T047	1.0	3.024	12	5	BT	0.591^b, 0.591^b, 0.411^t, 0.404^t, 0.403^t, 0.327, 0.110, 0.067, 0.057, 0.033, 0.019, 0.011
T048	1.0	3.509	11	4	TT	0.653^{t1}, 0.614^{t2}, 0.606^{t2}, 0.509^{t1},0.506^{t1}, 0.372^{t2}, 0.155, 0.040, 0.023, 0.023, 0.008
T049	1.0	2.466	6	1	T	0.679^t, 0.678^t, 0.455^t, 0.316, 0.312, 0.026
T050	1.0	3.010	8	1	BT	0.729^b, 0.697^b, 0.325^t, 0.319^t, 0.317^t, 0.307, 0.282, 0.034
T051	1.0	2.669	10	2	BB	0.654^{b1}, 0.526^{b1}, 0.440^{b2}, 0.323, 0.274^{b2}, 0.160, 0.129, 0.092, 0.048, 0.023
T052	1.0	3.717	13	6	Q	0.859^q, 0.856^q, 0.442^q, 0.439^q, 0.321, 0.318, 0.271, 0.057, 0.046, 0.037, 0.029, 0.024, 0.018
T053	1.0	3.343	12	5	T	0.762^t, 0.687^t, 0.660, 0.385, 0.285, 0.267, 0.161, 0.044, 0.036, 0.026, 0.016, 0.014^t
T054	1.0	3.506	12	5	B	0.779^b, 0.592^b, 0.504, 0.466, 0.350, 0.334, 0.315, 0.073, 0.027, 0.026, 0.022, 0.018
T055	1.0	3.791	6	1	Q	0.935^q, 0.924^q, 0.850^q, 0.847^q, 0.182, 0.053
T056	1.0	3.841	6	1	Q	1.111^q, 1.051^q, 0.563^q, 0.552^q, 0.531, 0.033
T057	1.0	3.712	4	0	Q	1.183^q, 0.913^q, 0.813^q, 0.803^q
T058	1.0	3.758	11	4	B	0.985, 0.966^b, 0.547^b, 0.457, 0.452, 0.105, 0.084, 0.059, 0.052, 0.032, 0.019
T059	1.0	3.510	10	2	BBT	0.847^{b1}, 0.786^{b1}, 0.663, 0.298^t, 0.296^t, 0.289^t, 0.127^{b2}, 0.122,^{b2} 0.078, 0.014
T060	1.0	3.882	8	3	T	1.155, 0.930^t, 0.885^t, 0.426^t, 0.418, 0.031, 0.023, 0.014
V041	0.1	3.330	8	3	Q	0.807^q, 0.804^q, 0.758^q, 0.748^q, 0.081, 0.054, 0.041, 0.037
V042	0.1	3.198	10	2	BQ	0.907^q, 0.899^q, 0.474^q, 0.270^q, 0.164, 0.159, 0.097^b, 0.096^b, 0.069, 0.063
V043	0.1	3.354	6	0	BQ	0.715^b, 0.712^b, 0.510^q, 0.509^q, 0.456^q, 0.452^q
V044	0.1	3.388	9	4	T	0.866^t, 0.860^t, 0.559^t, 0.536, 0.495, 0.040, 0.011, 0.011, 0.010
V045	0.1	2.713	10	2	TT	0.523^{t1}, 0.515^{t1}, 0.301^{t2}, 0.291, 0.288^{t2}, 0.274^{t2}, 0.266^{t1}, 0.185, 0.049, 0.021
V046	0.1	2.878	5	0	T	0.674^t, 0.590^t, 0.584^t, 0.571, 0.459
V047	0.1	3.509	8	1	TQ	0.613^t, 0.611^t, 0.535^q, 0.534^q, 0.444^q, 0.402^q, 0.362^t, 0.008
V048	0.1	3.369	11	5	BT	0.598^t, 0.594^t, 0.528^b, 0.524^b, 0.483, 0.461^t, 0.053, 0.05, 0.042, 0.024, 0.012
V049	0.1	3.302	3	0	T	1.400^t, 0.960^t, 0.942^t
V050	0.1	3.377	7	2	Q	0.895^q, 0.881^q, 0.685^q, 0.682^q, 0.189, 0.027, 0.018
V051	0.1	3.614	5	0	B	0.755, 0.740, 0.710^b, 0.705, 0.704^b
V052	0.1	3.679	6	0	B	0.926, 0.846^b, 0.740^b, 0.577, 0.399, 0.191
V053	0.1	3.732	7	2	BQ	0.800^q, 0.759^q, 0.755^q, 0.710^q, 0.645, 0.048^b, 0.015^b
V054	0.1	3.824	13	8	Q	0.987^q, 0.983^q, 0.613, 0.519^q, 0.512^q, 0.042, 0.042, 0.033, 0.029, 0.018, 0.017, 0.015, 0.014
V055	0.1	3.568	13	6	B	0.657^b, 0.646^b, 0.524, 0.464, 0.415, 0.358, 0.353, 0.043, 0.030, 0.029, 0.018, 0.017, 0.014
V056	0.1	3.571	16	8	BQ	0.809^q, 0.767^q, 0.450^q, 0.410^q, 0.360, 0.337, 0.133, 0.099^b, 0.055, 0.033, 0.028, 0.026^b, 0.022, 0.017, 0.016, 0.009
V057	0.1	3.475	10	4	Q	1.053^q, 0.646^q, 0.614^q, 0.383^q, 0.372, 0.298, 0.050, 0.025, 0.023, 0.011
V058	0.1	3.818	6	2	Q	1.026^q, 1.022^q, 0.873^q, 0.871^q, 0.016, 0.010
V059	0.1	3.849	8	5	T	1.620^t, 1.072^t, 1.072^t, 0.038, 0.015, 0.013, 0.010, 0.009
V060	0.1	3.886	4	0	Q	1.072^q, 1.071^q, 0.863^q, 0.860^q
W041	0.01	2.440	7	2	Q	0.966^q, 0.645^q, 0.638^q, 0.265^q, 0.152, 0.023, 0.011
W042	0.01	3.250	4	0	Q	0.929^q, 0.918^q, 0.886^q, 0.519^q
W043	0.01	3.250	6	0	Q	0.836^q, 0.834^q, 0.620^q, 0.613^q, 0.179, 0.171
W044	0.01	3.360	7	2	BT	0.794^t, 0.792^t, 0.585^b, 0.583^b, 0.562^t, 0.076, 0.015
W045	0.01	3.250	6	0	BQ	0.845^b, 0.637^b, 0.466^q, 0.463^q, 0.424^q, 0.419^q
W046	0.01	2.040	5	0	T	0.446^t, 0.427^t, 0.424^t, 0.398, 0.344
W047	0.01	3.340	6	0	T	0.867, 0.788, 0.555^t, 0.431^t, 0.427^t, 0.276
W048	0.01	3.380	9	2	BT	0.622^t, 0.594^t, 0.566^b, 0.563^t, 0.482^b, 0.377, 0.122, 0.038, 0.012
W049	0.01	2.770	7	2	Q	1.140^q, 1.105^q, 0.191^q, 0.188^q, 0.114, 0.020, 0.016
W050	0.01	3.140	6	0	Q	0.938^q, 0.709^q, 0.452^q, 0.450^q, 0.444, 0.145
W051	0.01	3.230	5	0	Q	0.927^q, 0.926^q, 0.619^q,, 0.617^q, 0.138
W052	0.01	3.760	5	0	T	1.070^t, 0.784, 0.704^t, 0.674^t, 0.524
W053	0.01	3.700	8	3	Q	0.992^q, 0.873,^{q} 0.862^q, 0.702^q, 0.108, 0.075, 0.051, 0.034
W054	0.01	3.850	4	0	Q	1.028^q, 1.024^q, 0.906^q, 0.894^q
W055	0.01	3.710	7	2	Q	0.962^q, 0.960^q, 0.797^q, 0.791^q, 0.132, 0.040, 0.026
W056	0.01	3.830	6	2	Q	1.060^q, 1.037^q, 0.827^q, 0.823^q, 0.060, 0.021
W057	0.01	3.850	3	0	T	1.781^t, 1.038^t, 1.029^t
W058	0.01	3.580	8	4	Q	0.928^q, 0.920^q, 0.817^q, 0.810^q, 0.049, 0.029, 0.020, 0.011
W059	0.01	3.890	3	3	T	1.740^t, 1.080^t, 1.070^t
W060	0.01	3.880	4	0	Q	1.099^q, 1.062^q, 0.868^q, 0.846^q

Table 6.2: We record the metallicity ($Z/Z_\odot$), the number of different realisations simulated ($N_{\rm REAL}$), the efficiency (i.e. mean fraction of the core mass converted into protostars, $\eta \equiv \sum\{M_\star\}/M_{\rm CORE}$), the mean number of stars formed from a single core ($\overline{N}_\star$), the numbers of singles (S), binaries (B), triples (T) and quadruples (Q), the multiplicity frequence (**mf**), the companion probability (**cp**), and the companion frequency (**cf**).

$Z/Z_\odot$	$N_{\rm REAL}$	η	$\overline{N}_\star$	S	B	T	Q	**mf**	**cp**	**cf**
1.00	20	0.623	9.05	98	12	13	5	0.23	0.46	0.90
0.10	20	0.643	8.25	81	8	8	11	0.25	0.51	1.19
0.01	20	0.624	5.80	37	3	7	13	0.38	0.68	1.81

metallicity has a much greater effect on the mean number of stars formed from a single core, $\overline{N}_\star$. Lowering the metallicity reduces the number of stars substantially.

In all of these simulations we see the same pattern of star formation. We can see the formation of the first star on a timescale of 50 to 70 kyr, and then the formation of a circumstellar disc around the primary from the material with too much angular momentum to accrete onto the central object. This disc then grows in mass and eventually becomes Toomre unstable and fragments to form multiple secondaries. This typically happens 10 to 100 kyr after the formation of the disc. Fig.6.1 and Fig.6.2 show the accretion histories for simulations with $Z = Z_\odot$, Fig.6.3 and Fig.6.4 for $Z = 0.1\,Z_\odot$, and Fig.6.5 and Fig.6.6 for $Z = 0.01\,Z_\odot$. We can see this pattern of accretion in these plots. The majority show the primary star forming, then a delay whilst the disc forms and increases in mass and becomes Toomre unstable, and then fragments to produce a clutch of secondaries. In the high metallicity simulations ($Z = Z_\odot$) some of these secondaries are ejected and become brown dwarfs, whilst the remaining secondaries stay in the disc and grow in mass to become hydrogen-burning stars. In the low metallicity simulations ($Z = 0.1\,Z_\odot$), a smaller number of secondaries are ejected, with the majority staying in the disc and accreting mass. This is because these fragments are initially higher in mass and fewer in number, and so are less likely to be ejected through interactions.

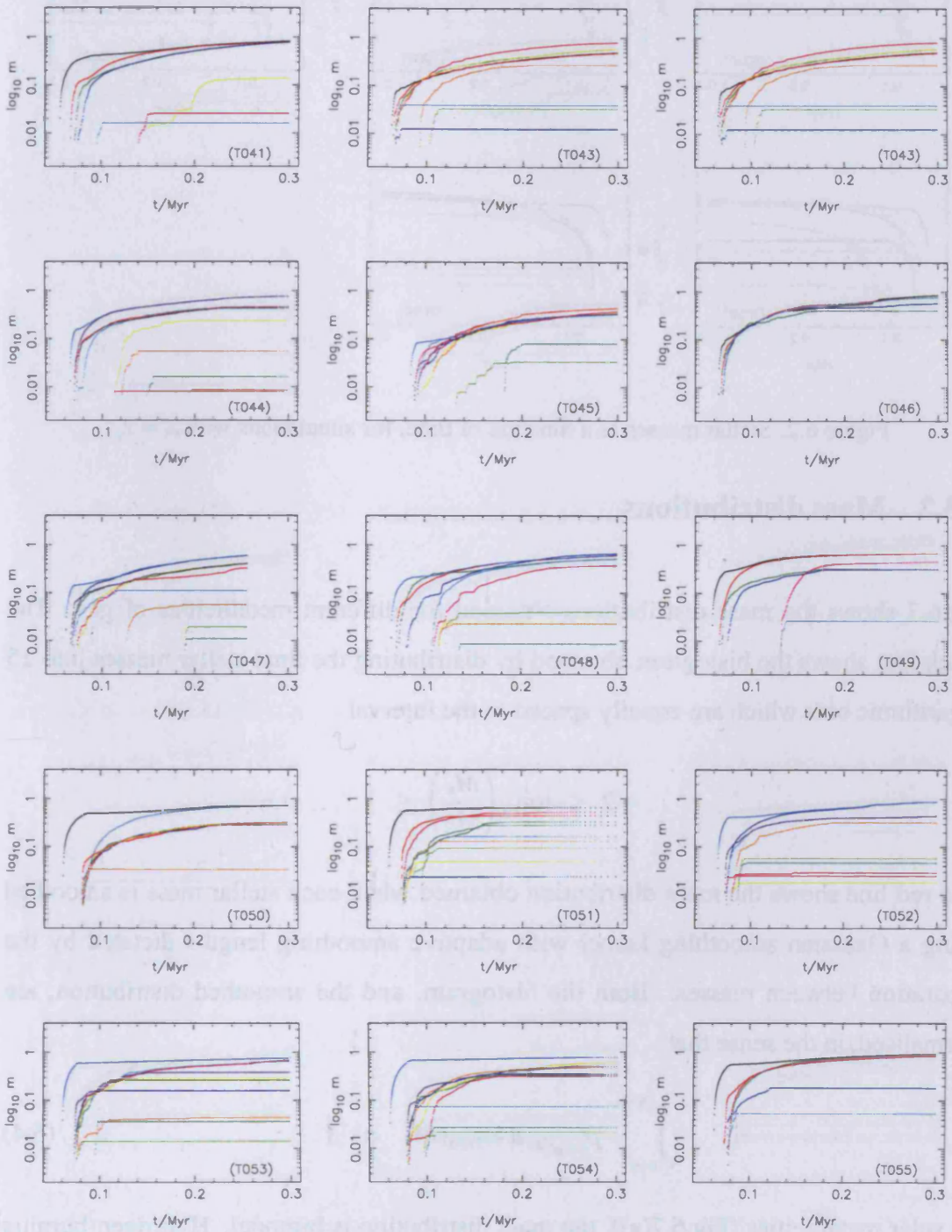

Figure 6.1: Stellar masses as a function of time, for simulations with $Z = Z_{\odot}$.

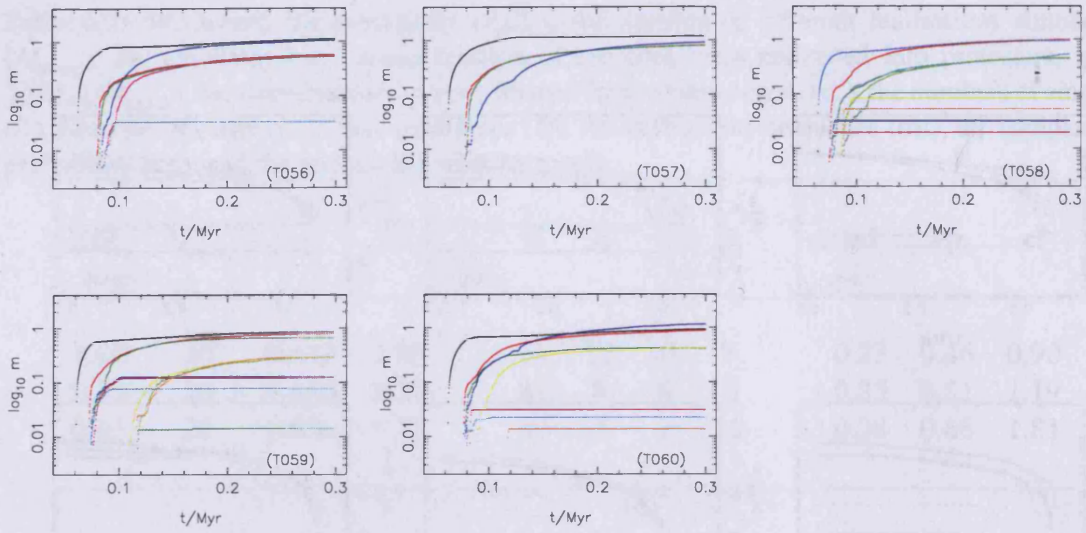

Figure 6.2: Stellar masses as a function of time, for simulations with $Z = Z_{\odot}$.

6.3.2 Mass distributions

Fig.6.7 shows the mass distributions obtained for different metallicities of gas. The black line shows the histogram obtained by distributing the final stellar masses into 15 logarithmic bins which are equally spaced in the interval

$$-2 \leq \log_{10}\left(\frac{M_{\star}}{\mathrm{M}_{\odot}}\right) \leq 1 .$$

The red line shows the mass distribution obtained when each stellar mass is smoothed using a Gaussian smoothing kernel with adaptive smoothing lengths dictated by the separation between masses. Both the histogram, and the smoothed distribution, are normalised, in the sense that

$$\int_{M=0}^{M=\infty} p_{\log_{10}(M)}\, d\log_{10}(M) \;=\; 1 . \qquad (6.4)$$

At solar metallicities (Fig.6.7(a)), the mass distribution is bimodal. Hydrogen-burning stars of masses 0.2 to 1.0 $\mathrm{M}_{\odot}$ make up the larger mode of the mass distribution, whilst brown dwarfs with masses in the range 0.02 to 0.06 $\mathrm{M}_{\odot}$ make up the secondary peak.

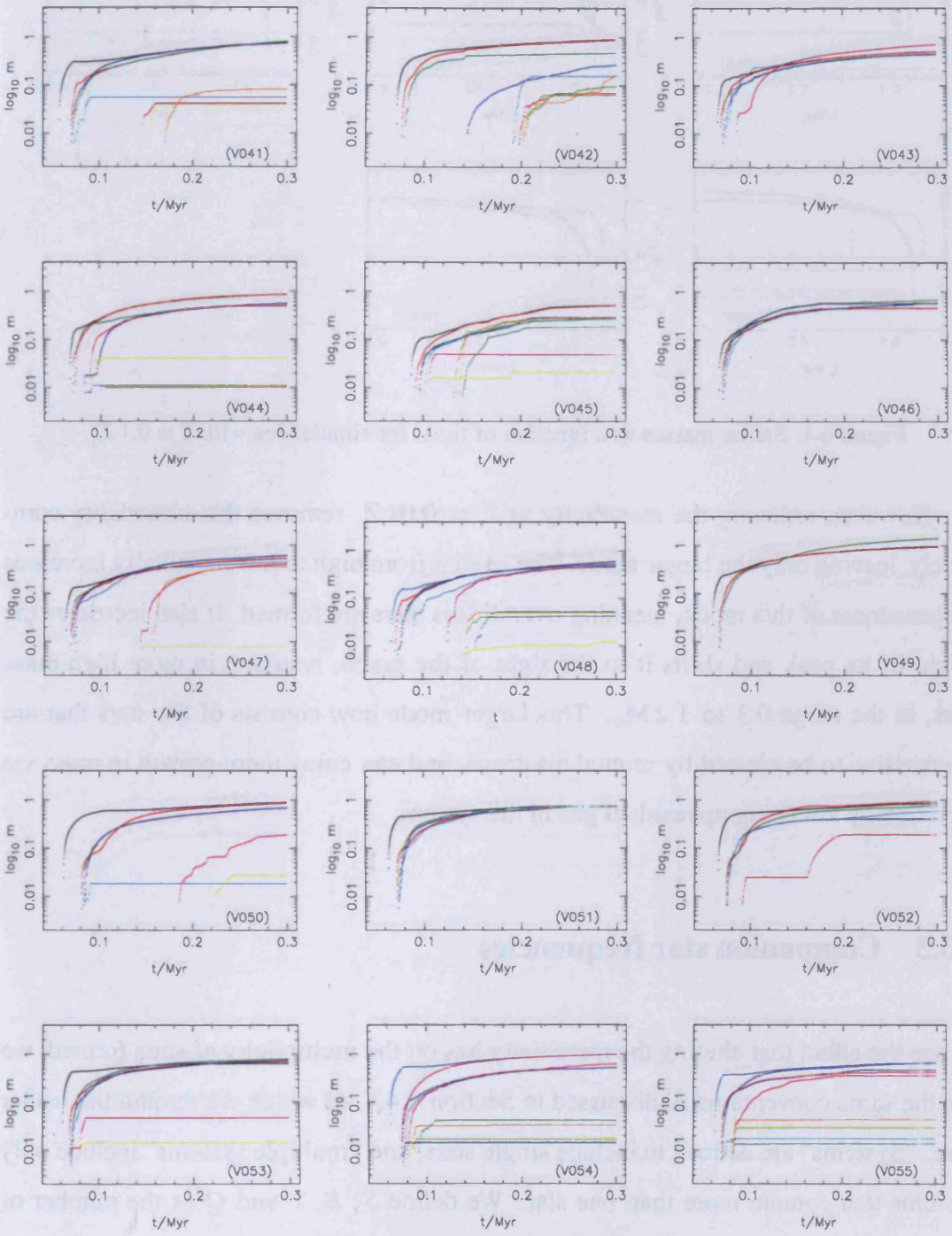

Figure 6.3: Stellar masses as a function of time, for simulations with $Z = 0.1\,Z_{\odot}$.

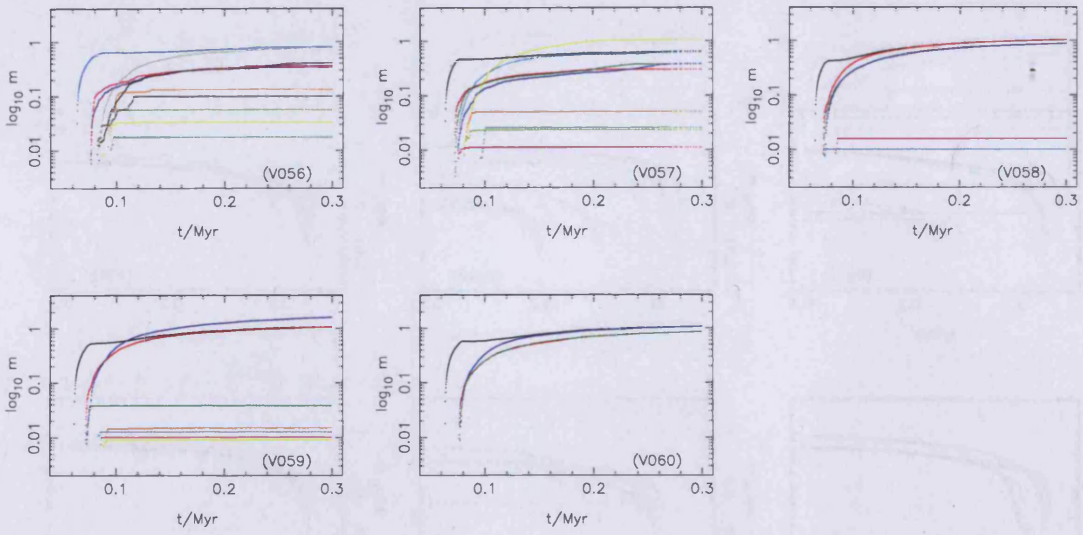

Figure 6.4: Stellar masses as a function of time, for simulations with $Z = 0.1\,Z_{\odot}$.

However, reducing the metallicity to $Z = 0.01\,Z_{\odot}$ removes this bimodality completely, leaving only the larger mode. The switch from high to low metallicity increases the broadness of this mode, meaning overall less stars are formed. It also increases the height of its peak and shifts it to the right of the graph, resulting in more high-mass stars, in the range 0.3 to $1.2\,M_{\odot}$. This larger mode now consists of the stars that are too massive to be ejected by mutual ejections, and can enjoy more growth in mass via accretion by sweeping up residual gas in the system.

6.3.3 Companion star frequencies

To see the effect that altering the metallicity has on the multiplicity of stars formed, we use the same conventions as discussed in Section 4.4.4, of which we remind the reader here. "Systems" are defined to include single stars, and "multiple systems" include only systems that contain more than one star. We define S, B, T and Q as the number of single, binary, triple and quadruple systems respectively.

The multiplicity frequency, **mf**, measures the fraction of systems which are multi-

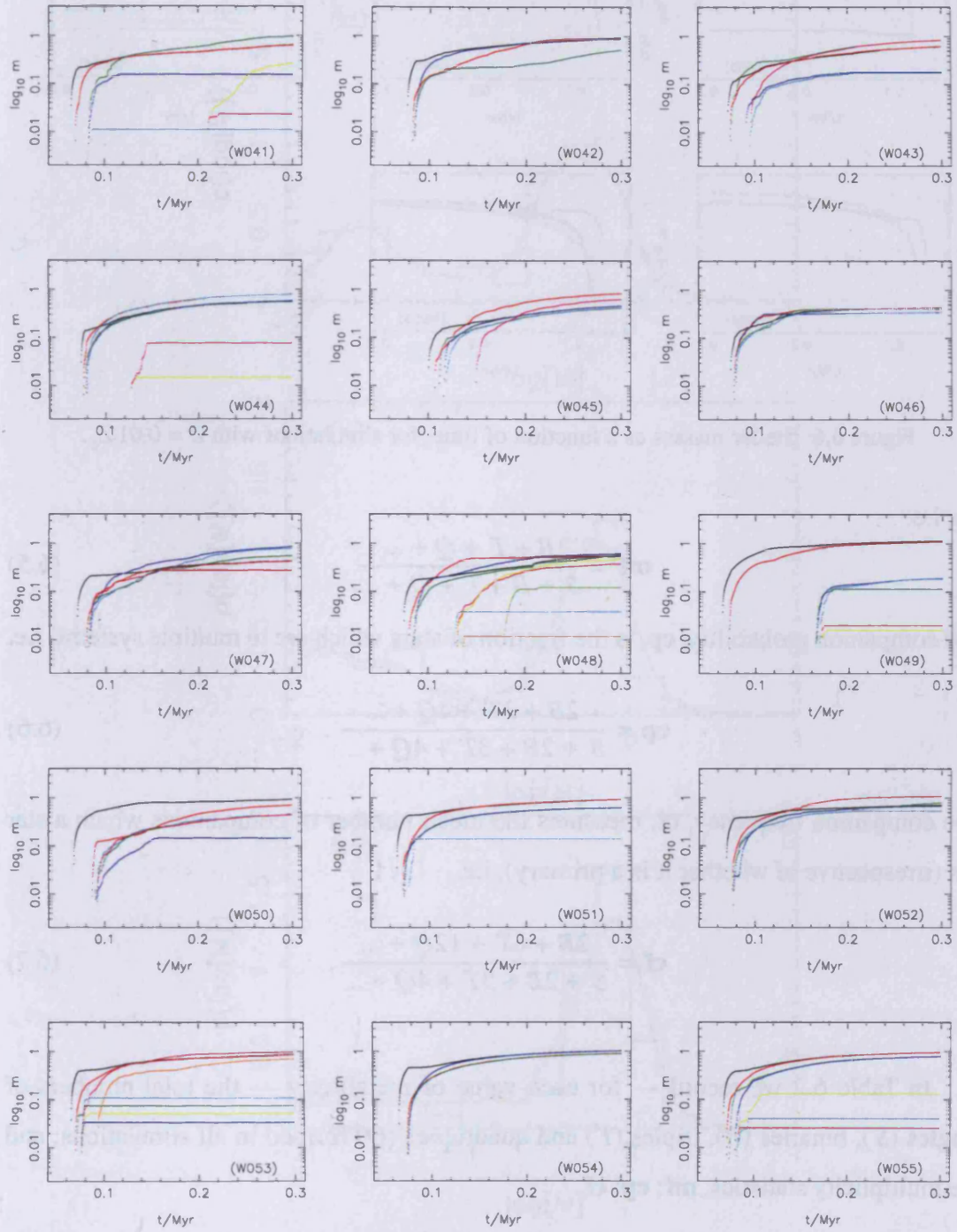

Figure 6.5: Stellar masses as a function of time, for simulations with $Z = 0.01\,Z_{\odot}$.

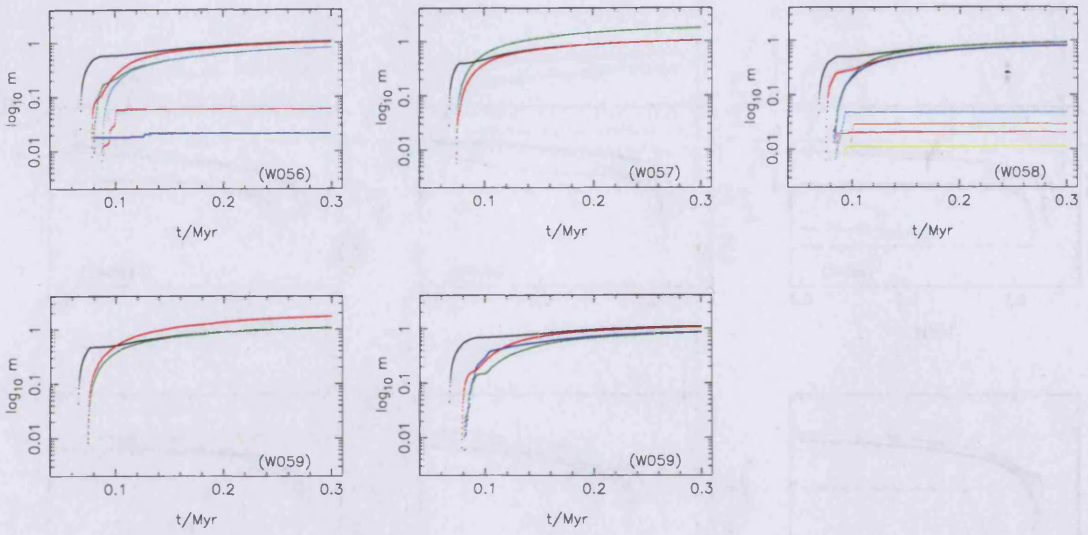

Figure 6.6: Stellar masses as a function of time, for simulations with $Z = 0.01\,Z_{\odot}$.

ple, i.e.

$$\mathbf{mf} = \frac{B + T + Q + ...}{S + B + T + Q + ...}. \tag{6.5}$$

The companion probability, **cp**, is the fraction of stars which are in multiple systems, i.e.

$$\mathbf{cp} = \frac{2B + 3T + 4Q + ...}{S + 2B + 3T + 4Q + ...}. \tag{6.6}$$

The companion frequency, **cf**, measures the mean number of companions which a star has (irrespective of whether it is a primary), i.e.

$$\mathbf{cf} = \frac{2B + 6T + 12Q + ...}{S + 2B + 3T + 4Q + ...}. \tag{6.7}$$

In Table 6.2 we record — for each value of metallicity — the total numbers of singles (S), binaries (B), triples (T) and quadruples (Q) formed in all simulations; and the multiplicity statistics, **mf**; **cp**; **cf**.

A core with $Z = 0.01\,Z_{\odot}$ spawns fewer single-star systems but more quadruple systems than a gas with $Z = Z_{\odot}$. This is reflected in the calculated quantities (**mf**, **cp**, **cf**). The fraction of stars in multiple systems (**cp**) increases as the metallicity decreases.

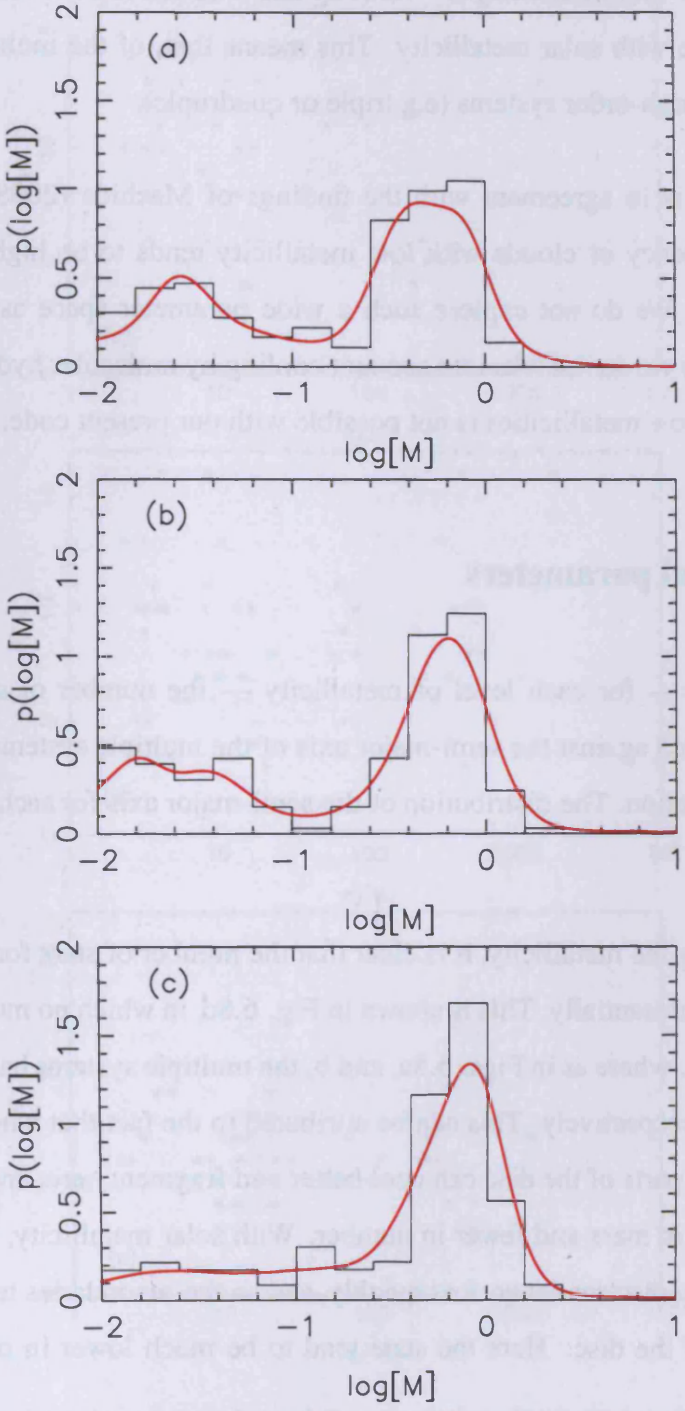

Figure 6.7: Normalised stellar mass distribution. The black lines represent a histogram of the raw data, and the red lines represent the distribution when smoothed by a Gaussian kernel.

Further to this, the mean number of companions (**cf**) increases sharply, so that star formation in a core with metallicity $Z = 0.01\,Z_{\odot}$ has twice as many companions as a star formed in a core with solar metallicity. This means that, of the multiple systems that form, more are high-order systems (e.g triple or quadruple).

This result is in agreement with the findings of Machida (2008). He finds that the binary frequency of clouds with low metallicity tends to be higher than for high metallicity gas. We do not explore such a wide parameter space as Machida (2008; $Z = 0 - Z_{\odot}$) since we do not take into account cooling by molecular hydrogen, and hence modelling very low metallicities is not possible with our present code.

6.3.4 Orbital parameters

Fig. 6.8 shows — for each level of metallicity — the number of stars formed in a simulation, plotted against the semi-major axis of the multiple systems identified at the end of the simulation. The distribution of the semi-major axis for each system is shown in Fig. 6.9.

By reducing the metallicity, it is clear that the number of stars formed in a simulation decreases substantially. This is shown in Fig. 6.8c, in which no multiple system has more that 9 stars, where as in Figs. 6.8a, and b, the multiple systems have a maximum of 14 and 16 stars respectively. This can be attributed to the fact that when the metallicity is low, the inner parts of the disc can cool better and fragment here, and so the stars that form are higher in mass and fewer in number. With solar metallicity, the inner parts of the circumbinary disc cannot cool as quickly, and so the secondaries tend to form in the outer regions of the disc. Here the stars tend to be much lower in mass, and high in number.

With a metallicity of $Z = Z_{\odot}$, the semi-major axis distribution of multiple systems formed has a mean $\mu_{\log_{10}(a)} \simeq 1.2$ and a standard deviation $\sigma_{\log_{10}(a)} \simeq 0.8$; with $Z = 0.1\,Z_{\odot}$

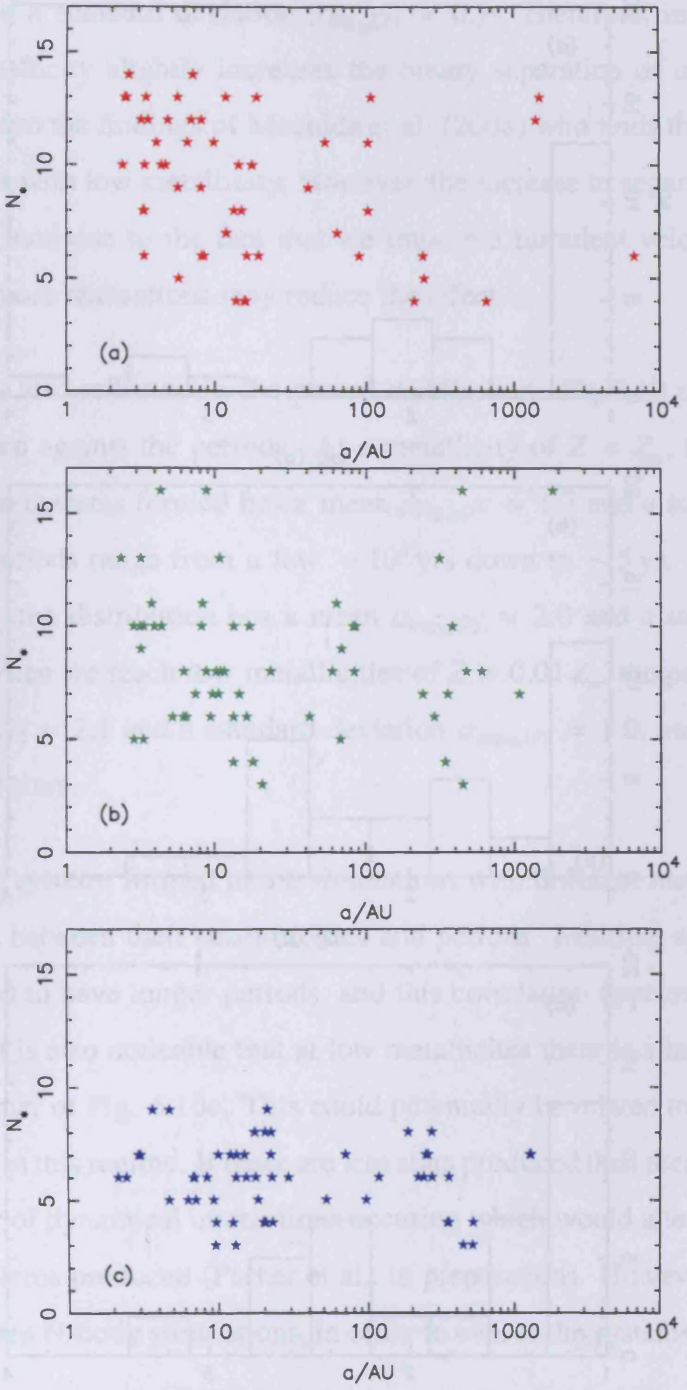

Figure 6.8: The total number of stars formed in a simulation, N_* plotted against the semi-major axis, a, of the multiple systems formed, with metallicities (a) $Z = Z_\odot$, (b) $Z = 0.1\,Z_\odot$, and (c) $Z = 0.01\,Z_\odot$.

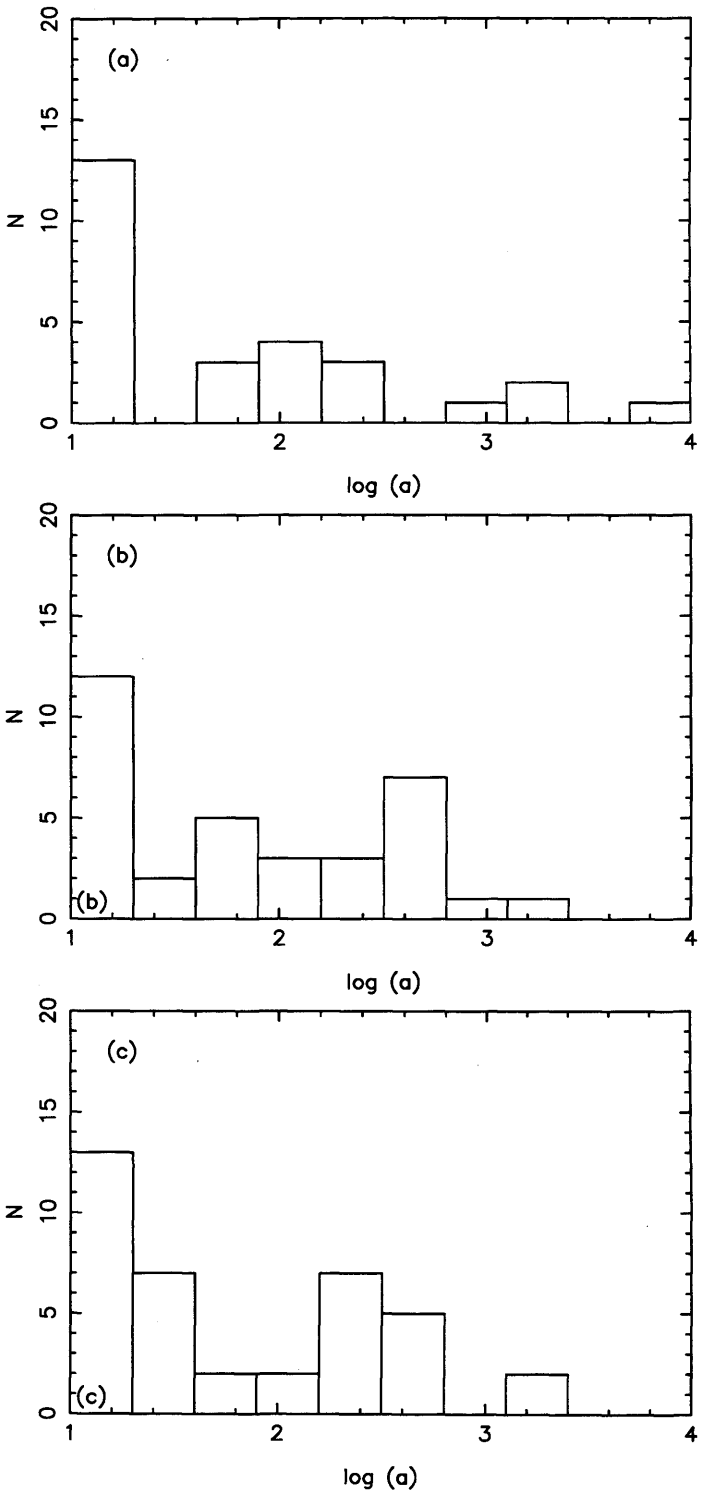

Figure 6.9: The distribution of the semi-major axis, a, of the multiple systems formed, with metallicities (a) $Z = Z_{\odot}$, (b) $Z = 0.1\,Z_{\odot}$, and (c) $Z = 0.01\,Z_{\odot}$.

a mean $\mu_{\log_{10}(a)} \simeq 1.4$ and standard deviation $\sigma_{\log_{10}(a)} \simeq 0.8$; with $Z = 0.01\,Z_{\odot}$ a mean $\mu_{\log_{10}(a)} \simeq 1.5$ and a standard deviation $\sigma_{\log_{10}(P)} \simeq 0.7$. Therefore, in our simulations lowering the metallicity slightly increases the binary separation of multiple systems. This is in contrast to the findings of Machida et al. (2008) who finds that the separation actually decreases with low metallicity. However, the increase in separation that we see is only marginal, and due to the fact that we impose a turbulent velocity field on the cores modelled, more realisations may reduce the effect.

This trend is also reflected in the period distribution. Fig.6.10 shows orbital eccentricities, plotted against the periods. At a metallicity of $Z = Z_{\odot}$, the period distribution of multiple systems formed has a mean $\mu_{\log_{10}(P)} \simeq 1.7$ and a standard deviation $\sigma_{\log_{10}(P)} \simeq 1.1$; periods range from a few $\sim 10^4$ yrs down to ~ 5 yr. With a metallicity of $Z = 0.1\,Z_{\odot}$ the distribution has a mean $\mu_{\log_{10}(P)} \simeq 2.0$ and a standard deviation $\sigma_{\log_{10}(P)} \simeq 1.1$. When we reach low metallicities of $Z = 0.01\,Z_{\odot}$, the period distribution has a mean $\mu_{\log_{10}(P)} \simeq 2.1$ and a standard deviation $\sigma_{\log_{10}(P)} \simeq 1.0$, and no simulations form more than 9 stars.

The multiple systems formed in the simulations with different metallicities show a slight correlation between their eccentricities and periods. Multiple systems that have elliptic orbits tend to have longer periods, and this correlation appears stronger in low metallicity gas. It is also noticable that at low metallicites there is a lack of stars in the top righthand corner of Fig. 6.10c. This could potentailly be related to the low number of stars produced in this regime. If there are less stars produced then there are likely to be a smaller number of dynamical interactions occuring which would alter the eccentricity of the orbital systems produced (Parker et al., in preparation). However, to investigate this further requires N-body simulations, in order to evolve the systems correctly.

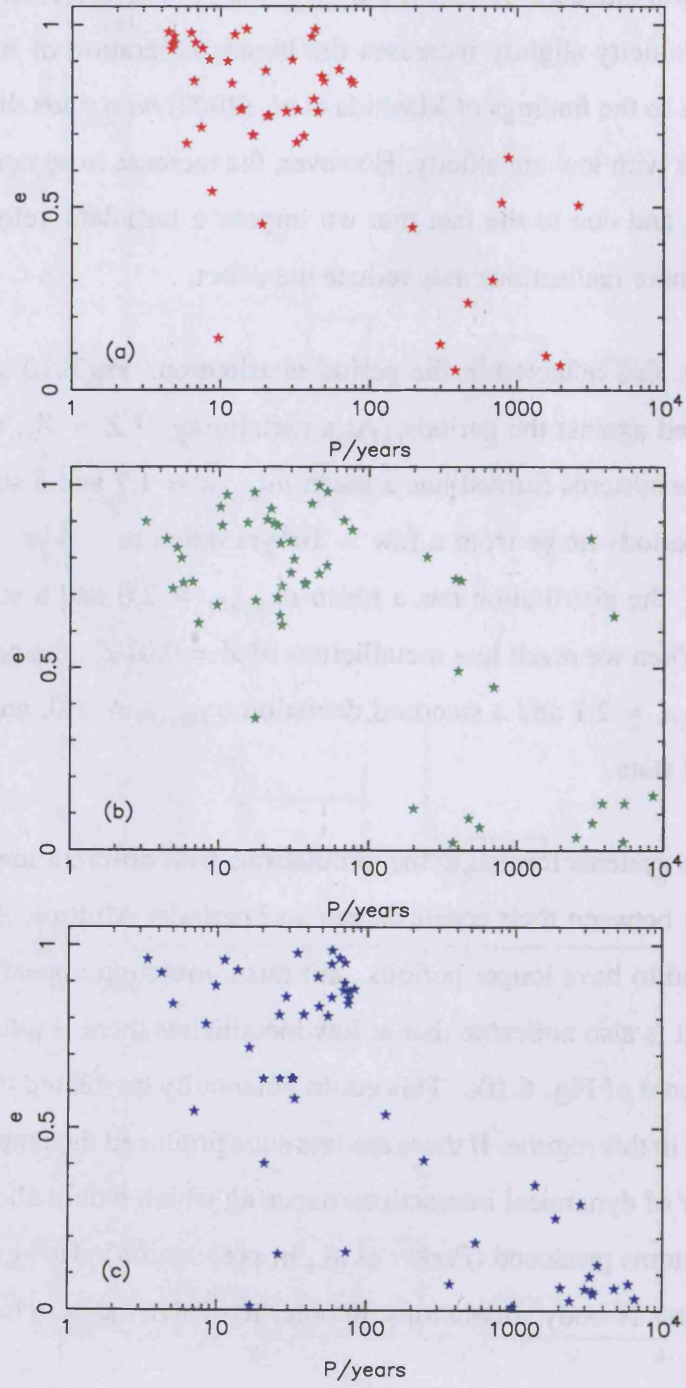

Figure 6.10: Orbital eccentricities, e, plotted against periods, P, for multiple prototars, with metallicities (a) $Z = Z_{\odot}$, (b) $Z = 0.1\,Z_{\odot}$, and (c) $Z = 0.01\,Z_{\odot}$.

6.3.5 The effect of reducing the metallicity

It has been known since the work of Low & Lynden-Bell (1976) that – at least in the regime where dust dominates the opacity – decreasing the metallicity increases the minimum mass for star formation. Hence it becomes harder to form brown dwarfs, and this is exactly what we observe in our simulations (in common with Machida 2008). In addition, we find that the separations of binaries increase somewhat with decreasing metallicity, although this is a small effect (and in the opposite sense to what Machida reports). These changes appear to be caused by a fundamental shift in the dominant pattern of star formation, due to the alteration in the cooling properties of the gas which accompanies a decrease in the metallicity.

When the metallicity is solar, a primary star forms from the material with low angular momentum, and then a disc often accumulates around this primary star. The inner parts of this circumprimary disc cannot fragment, because they are unable to cool fast enough (Gammie 2001; Stamatellos et al. 2008a). In contrast, the outer parts of the circumprimary disc usually fragment to produce a clutch of low-mass secondaries (brown dwarfs and very low-mass hydrogen-burning stars). Many of the resulting multiple systems are the result of one of these secondaries being scattered inwards to form a tight binary with the primary. However, many others are formed by two of the low-mass secondaries pairing up, and these systems also tend to be tight, because the components are of low mass and therefore have normally been born quite close together. Because there are usually many secondaries, there are multiple scattering events between the secondaries, and many of them are ejected as single stars.

When the metallicity is low, a primary star again forms from the material with low angular momentum, and again a disc often accumulates around this primary star. However, the inner parts of the circumprimary disc are now better able to cool. As a result more of the circumprimary discs fragments to produce secondaries, and these secondaries tend to have larger masses and greater separations at birth. As a result,

fewer very low-mass secondaries are produced, and hence fewer stars overall. Because there are fewer secondaries, the binary systems which are formed by a secondary being scattered inwards and pairing up with the primary are somewhat looser. And because the secondaries formed in the outer parts of the circumprimary disc are further apart, the binary systems that are formed by their pairing up also tend to be somewhat looser. In addition, because there are substantially fewer secondaries formed, there are fewer scattering events, and therefore fewer single stars are ejected. Consequently, the net multiplicity frequency, companion probability and companion frequency are all higher.

6.4 Summary

In this chapter we have looked at the effect which reducing the metallicity has on the mass distribution and binary statistics of stars formed from low-mass low-turbulence cores. We have performed an ensemble of simulations of the collapse and fragmentation of a $5.4\,M_\odot$ core with an initial level of turbulence $\alpha_{\rm TURB} = 0.25$ (as in Chapter 4). We have considered three different metallicities, $Z = Z_\odot$, $Z = 0.1\,Z_\odot$ and $Z = 0.01\,Z_\odot$. Reducing the metallicity appears to have the following effects.

- The mean mass of the stars increases, and the mean number of stars decreases. There appears to be little change in the efficiency of star formation, in the sense that the fraction of the core mass converted into stars after 300 kyr is in all cases $63 \pm 1\%$.

- There are many fewer brown dwarfs formed. The bimodal mass distribution observed with $Z = Z_\odot$ changes with decreasing metallicity in the sense that the low-mass mode (the one which comprises brown dwarfs and very low-mass hydrogen burning stars) steadily wanes, and the high-mass mode (the one comprising Sun-like stars) steadily waxes. Once the metallicity has decreased to $Z = 0.01\,Z_\odot$, the low-mass mode disappeares altogether, and is replaced by a flat extension to lower

masses (see Fig. 6.7).

- The binary frequency increases substantially; this is in agreement with the results of Machida (2008). However, in our simulations the binary separations increase somewhat, in contrast with what Machida finds. This has to do with the change in the pattern of disc fragmentation that accompanies a decrease in metallicity, as explained in the preceding section.

- There is some evidence that eccentricities and periods are anti-correlated (i.e. long-period systems tend to have low eccentricities).

Chapter 7

Summary

7.1 Numerical diffusion and numerical dissipation in star formation codes

In Chapter 3 we have measured the levels of numerical diffusion and numerical dissipation in our Smoothed Particle Hydrodynamics (SPH) code (described in Chapter 2). To do this we model acoustic oscillations of a self-gravitating isentropic monatomic gas-sphere. We explain that this is a highly relevent test code for star formation codes, in particular those that model the fragmentation of collapsing cores, since the pressure waves generated by the switch from approximate isothermality to approximate adiabacity play a crucial role at this stage of star formation.

We find that for SPH codes that adjust the smoothing length of a particle so as to keep the number of neighbours in the range $N_{\rm NEIB} \pm \Delta N_{\rm NEIB}$, $\Delta N_{\rm NEIB}$ should be set to zero. This ensures that the level of numerical diffusion of oscillation energy to other modes, and the level of numerical dissipation due to artifical viscosity, both remain low.

We propose that this should become a standard test for star formation codes, and encourage users of Adaptive Mesh Refinement codes to attempt to reproduce the results

obtained with SPH.

7.2 Treatment of the thermodynamics in collapsing cores

In Chapter 4 we have performed SPH simulations of the collapse and fragmentation of cores having different initial levels of turbulence ($\alpha_{\rm TURB}$ = 0.05, 0.10, 0.25). We use a new, more realistic treatment of the energy equation which captures (i) excitation of the rotational and vibrational degrees of freedom of H_2, dissociation of H_2, ionisation of H and He, and (ii) the transport of cooling radiation against opacity due to both dust and gas (including the effects of dust sublimation, molecules and H^- ions). We have also performed comparison simulations using a standard barotropic equation of state. The main results are summarised as follows.

- Increasing the level of turbulence generally tends to reduce the fraction of the core mass which is converted into stars, and increase the number of stars formed by a single core.
- Many simulations show the same pattern of star formation, in which the core collapses to form a primary after 50 to 70 kyr, with the accumulation of a massive disc around it. After 10 to 100 kyr this disc becomes Toomre unstable, and fragments to form a clutch of secondaries. Many of these secondaries are brown dwarfs or very low-mass hydrogen-burning stars. Some of them are ejected into the field.
- Switching from the standard barotropic equation of state to the new treatment of the energy equation has the following effects.
  - The fraction of core mass converted into stars is reduced (by $\sim$ 16%).
  - The number of protostars formed from a single core is greatly increased ($\sim$ 40%), with a higher proportion of brown dwarf stars.

- The mean period of multiple systems is reduced (by a factor ~ 3).
- The orbital eccentricities of multiple systems tend to be higher.
- The mass ratios of multiple systems tend to be higher (i.e. more nearly equal components).

We conclude that the differences in results obtained depending on the treatment of thermodynamics is due to the fact that the standard barotropic equation of state is designed to mimic the gross thermal behaviour of the gas at the centre of a collapsing, non-rotating 1 $M_\odot$ protostar. Therefore it becomes adiabatic at low densities. Alternatively the new treatment of the energy equation allows the gas in low-mass protofragments to stay approximately isothermal to higher densities. This is because the column density inhibiting the cooling of the fragments is lower, and their rate of contraction, and therefore rate of heating, is lower. Despite this method being still being an approximation for radiative transport, it is nevertheless a much more realistic treatment than a barotropic equation of state.

7.3 Prestellar cores in the Ophiuchus Main Cloud

In Chapter 5, we have modelled the evolution of an ensemble of prestellar cores in the Ophiuchus Main Cloud. We have simulated a range of masses, sizes and levels of turbulence, using initial conditions constrained by observations, and also recently revised dust temperatures, with a view to predicting the statistical properties of the stars that will form from these cores. The main results are summarised as follows.

- The star formation in the cores is extremely efficient, with typically a single star being produced on a timescale of 10 to 100 kyr. This is likely to be due to fact that the cores modelled have very high central densities, and so at the end of the

simulation all of the material in the outer parts of the core has had time to accrete onto the central star.

- Some of the cores produce multiple systems, according to the same pattern of star formation seen in Chapter 4, in which a primary star is formed followed by the formation and subsequent fragmentation of a disc into multiple secondaries. Of the multiple systems that form, the majority have highly eccentric orbits.

- The number of stars formed by a core is highest if the core has high mass. There is also a weak dependence on the initial level of turbulence and the initial density, in that cores with a high initial level of turbulence, and/or starting from a low initial density may produce more than one star.

7.4 The effect of metallicity on the core collapse

In Chapter 6 we have performed an ensemble simulations of the collapse and fragmentation of a 5.4 $M_\odot$ core with an initial level of turbulence $\alpha_{\rm TURB} = 0.25$, and explored the effects of different metallicities $Z = Z_\odot$, $Z = 0.1\,Z_\odot$ and $Z = 0.01\,Z_\odot$. We summarise the main results.

- Reducing the metallicity decreases the number of stars formed from a single core.

- Fewer brown dwarfs are formed at lower metallicities. At $Z = Z_\odot$, the mass distribution is bimodal, consisting of 2 modes, the first in the low mass region comprising brown dwarfs and very low-mass stars, and the second in the higher mass region comprising hydrogen-burning stars. At At $Z = 0.01Z_\odot$, the low-mass mode disappears completely.

- Reducing the metallicity increases the binary frequency, which is in agreement with previous authors. However, it also increases the binary separations, which

is not in agreement with the same authors. We explain this trend in terms of the pattern of disc fragmenation and how it changes with different metallicities.

7.5 Future work

I plan to continue to develop and improve our star formation code DRAGON. In particular, I would like to improve the sink algorithm. The current version of the algorithm may compromise our results, in terms of resolution. Physical processes may not be properly resolved on small scales, which may result in different results for the binary systems obtained in this thesis. Sinks also favour N-body interactions. We adopt gravitational softening for their interactions and this may cause stars to be wrongly ejected from systems, whilst suppressing dissipative interactions between, and mergers of, stars.

I will perform more simulations of collapsing cores covering a wider parameter space than that already explored, in order to further investigate what effects the initial level of turbulence, the core mass and the metallicity, have on the mass distribution, kinematics and binary statistics of the resulting stars. Also, I will perform more simulations of the existing parameter space to improve upon the results I have already obtained. The work in Chapter 5 on the models of prestellar cores in Ophiuchus will be revisited using the revised initial levels of turbulence. It would be interesting to see if our initial findings, regarding the effects that the core mass, initial level of turbulence and central density have on the outcome, still stand. I will also look into a way of reproducing the observed projected shapes, rather than assuming spherical geometry which is not realistic for all of the cores in the ensemble.

I plan to continue a systematic investigation into determining whether certain physical effects influence the outcome in any way. The next stage is to introduce feedback, both mechanical and radiative, into the simulations. The levels of star formation in the current results are very high. Including radiative feedback from the surrounding stars,

and mechanical feedback in the form of bipolar outflows is likely both to delay star formation and to reduce the efficiency of star formation.

Finally, it is thought that magnetic fields will have a serious effect on the findings in this thesis, and so I plan to continue to develop the existing Cardiff SPH code designed for handling non-ideal MHD effects. The code currently does not include divergence cleaning, and so I would like to develop this.

Bibliography

Alves J., Lombardi M., Lada C. J., 2007, A&A, 462, L17

André P., Belloche A., Motte F., Peretto N., 2007, A&A, 472, 519

Andre P., Ward-Thompson D., Barsony M., 1993, ApJ, 406, 122

Andre P., Ward-Thompson D., Barsony M., 2000, "Protostars and Planets IV", Ed. V. Mannings, A. Boss, A.P. Boss, S.S. Russel, The University of Arizona Press, p59

Andre P., Ward-Thompson D., Motte F., 1996, A&A, 314, 625

Balsara D. S., 1995, Journal of Computational Physics, 121, 357

Barnes J., Hut P., 1986, Nature, 324, 446

Bate M. R., Bonnell I. A., 1997, MNRAS, 285, 33

Bate M. R., Bonnell I. A., Bromm V., 2002a, MNRAS, 332, L65

Bate M. R., Bonnell I. A., Bromm V., 2002b, MNRAS, 336, 705

Bate M. R., Bonnell I. A., Bromm V., 2003, MNRAS, 339, 577

Bate M. R., Bonnell I. A., Price N. M., 1995, MNRAS, 277, 362

Bate M. R., Burkert A., 1997, MNRAS, 288, 1060

Bhattal A. S., 1996, Ph.D. Thesis, University of Wales, Cardiff

Black D. C., Bodenheimer P., 1975, ApJ, 199, 619

Bonnell I., Martel H., Bastien P., Arcoragi J.-P., Benz W., 1991, ApJ, 377, 553

Bonnell I. A., Bate M. R., Vine S. G., 2003, MNRAS, 343, 413

Bonnell I. A., Bate M. R., Zinnecker H., 1998, MNRAS, 298, 93

Boss A. P., Fisher R. T., Klein R. I., McKee C. F., 2000, ApJ, 528, 325

Boyd D. F. A., Whitworth A. P., 2005, A&A, 430, 1059

Bromm V., Coppi P. S., Larson R. B., 2002, ApJ, 564, 23

Bromm V., Ferrara A., Coppi P. S., Larson R. B., 2001, MNRAS, 328, 969

Burgasser A. J., Reid I. N., Siegler N., Close L., Allen P., Lowrance P., Gizis J., 2007, in Reipurth B., Jewitt D., Keil K., ed, Protostars and Planets V, p. 427

Burkert A., Bodenheimer P., 1993, MNRAS, 264, 798

Burkert A., Bodenheimer P., 2000, ApJ, 543, 822

Caselli P., Walmsley C. M., Terzieva R., Herbst E., 1998, ApJ, 499, 234

Chapman S., Pongracic H., Disney M., Nelson A., Turner J., Whitworth A., 1992, Nature, 359, 207

Christlieb N., Wisotzki L., Reimers D., Homeier D., Koester D., Heber U., 2001, A&A, 366, 898

Clarke C. J., 2008, ASP Conf.Ser. Vol. 390 76C

Commerçon B., Hennebelle P., Audit E., Chabrier G., Teyssier R., 2008, A&A, 482, 371

Duquennoy A., Mayor M., 1991, A&A, 248, 485

Elmegreen B. G., 2000, ApJ, 530, 277

Frebel A., Norris J. E., Christlieb N., Beers T. C., Asplund M., Bessell M. S., Aoki W., 2005, in Bulletin of the American Astronomical Society, Vol. 37, Bulletin of the American Astronomical Society, p. 1272

Gammie C. F., 2001, ApJ, 553, 174

Gingold R. A., Monaghan J. J., 1977, MNRAS, 181, 375

Goodwin S. P., Kroupa P., 2005, A&A, 439, 565

Goodwin S. P., Nutter D., Kroupa P., Ward-Thompson D., Whitworth A. P., 2008, A&A, 477, 823

Goodwin S. P., Ward-Thompson D., Whitworth A. P., 2002, MNRAS, 330, 769

Goodwin S. P., Whitworth A. P., Ward-Thompson D., 2004a, A&A, 414, 633

Goodwin S. P., Whitworth A. P., Ward-Thompson D., 2004b, A&A, 423, 169

Goodwin S. P., Whitworth A. P., Ward-Thompson D., 2006, A&A, 452, 487

Hernquist L., Katz N., 1989, ApJS, 70, 419

Hosking J. G., Whitworth A. P., 2004, MNRAS, 347, 994

Hubber D. A., 2006, Ph.D. Thesis, University of Wales, Cardiff

Hubber D. A., Goodwin S. P., Whitworth A. P., 2006, A&A, 450, 881

Hubber D. A., Whitworth A. P., 2005, A&A, 437, 113

Jappsen A.-K., Glover S. C. O., Klessen R. S., Mac Low M.-M., 2007, ApJ, 660, 1332

Jeans J. H., 1928, Astronomy and cosmogony. Cambridge [Eng.] The University press, 1928.

Jijina J., Myers P. C., Adams F. C., 1999, ApJS, 125, 161

Joergens V., 2008, arXiv:0809.4002

Johnstone D., Wilson C. D., Moriarty-Schieven G., Joncas G., Smith G., Gregersen E., Fich M., 2000, ApJ, 545, 327

Kratter K. M., Matzner C. D., 2006, MNRAS, 373, 1563

Krumholz M. R., Klein R. I., McKee C. F., 2007, ApJ, 656, 959

Lada C. J., 1987, in IAU Symposium, Vol. 115, Peimbert M., Jugaku J., ed, Star Forming Regions, p. 1

Larson R. B., 1969, MNRAS, 145, 271

Larson R. B., 1981, MNRAS, 194, 809

Loren R. B., 1989, ApJ, 338, 902

Low C., Lynden-Bell D., 1976, MNRAS, 176, 367

Lucatello S., Tsangarides S., Beers T. C., Carretta E., Gratton R. G., Ryan S. G., 2005, ApJ, 625, 825

Lucy L. B., 1977, AJ, 82, 1013

Luhman K. L., 2004, ApJ, 617, 1216

Luhman K. L., Joergens V., Lada C., Muzerolle J., Pascucci I., White R., 2007, in Reipurth B., Jewitt D., Keil K., ed, Protostars and Planets V, p. 443

Machida M. N., 2008, ApJ, 682, L1

Mamajek E. E., 2008, Astronomische Nachrichten, 329, 10

Martín E. L., Dougados C., Magnier E., Ménard F., Magazzù A., Cuillandre J.-C., Delfosse X., 2001, ApJ, 561, L195

Masunaga H., Inutsuka S.-i., 2000, ApJ, 531, 350

Matzner C. D., Levin Y., 2005, ApJ, 628, 817

Mazeh T., Goldberg D., Duquennoy A., Mayor M., 1992, ApJ, 401, 265

McDonald J. M., Clarke C. J., 1993, MNRAS, 262, 800

McDonald J. M., Clarke C. J., 1995, MNRAS, 275, 671

Mestel L., Spitzer L., Jr., 1956, MNRAS, 116, 503

Monaghan J. J., 1992, ARA&A, 30, 543

Monaghan J. J., Lattanzio J. C., 1985, A&A, 149, 135

Morris J. P., Monaghan M. M., 1997, Journal of Computational Physics, 136, 41

Motte F., Andre P., Neri R., 1998, A&A, 336, 150

Mouschovias T. C., 1976, ApJ, 207, 141

Mouschovias T. C., Spitzer L., Jr., 1976, ApJ, 210, 326

Myers P. C., 1983, ApJ, 270, 105

Myers P. C., 1998, ApJ, 496, L109

Myers P. C., Benson P. J., 1983, ApJ, 266, 309

Myers P. C., Ladd E. F., Fuller G. A., 1991, ApJ, 372, L95

Myers P. C., Linke R. A., Benson P. J., 1983, ApJ, 264, 517

Nelson A. F., 2006, MNRAS, 373, 1039

Nelson R. P., Papaloizou J. C. B., 1993, MNRAS, 265, 905

Nelson R. P., Papaloizou J. C. B., 1994, MNRAS, 270, 1

Nutter D., Ward-Thompson D., 2007, MNRAS, 374, 1413

Nutter D., Ward-Thompson D., André P., 2006, MNRAS, 368, 1833

Ochi Y., Sugimoto K., Hanawa T., 2005, ApJ, 623, 922

Offner S. S. R., Klein R. I., McKee C. F., 2008, arXiv:0806.1045

Price D. J., 2007, Publications of the Astronomical Society of Australia, 24, 159

Price D. J., Bate M. R., 2007, MNRAS, 377, 77

Price D. J., Bate M. R., 2008, MNRAS, 385, 1820

Price D. J., Monaghan J. J., 2004, MNRAS, 348, 139

Pudritz R. E., 2003, Les Houchess Summer School (Eds. V. Beskin, G. Henri, F. Menard); Springer, Berlin

Rafikov R. R., 2005, ApJ, 621, L69

Reipurth B., Clarke C., 2001, AJ, 122, 432

Reipurth B., Zinnecker H., 1993, A&A, 278, 81

Richer J. S., Shepherd D. S., Cabrit S., Bachiller R., Churchwell E., 2000, Protostars and Planets IV, 867

Rosswog S., Davies M. B., Thielemann F.-K., Piran T., 2000, A&A, 360, 171

Salmon J. K., Warren M. S., Winckelmans G. S., 1994, International Journal of Supercomputer Applications and High Performance Computing, 8, 129

Simpson R. J., Nutter D., Ward-Thompson D., 2008, arXiv:0807.4382

Spiegel E. A., 1957, ApJ, 126, 202

Stamatellos D., Hubber D. A., Whitworth A. P., 2007b, MNRAS, 382, L30

Stamatellos D., Whitworth A. P., 2008a, A&A, 480, 879

Stamatellos D., Whitworth A. P., 2008b, arXiv:0809.5042

Stamatellos D., Whitworth A. P., Bisbas B., Goodwin S., 2007a, A&A, 475, 37

Stamatellos D., Whitworth A. P., Boyd D. F. A., Goodwin S. P., 2005, A&A, 439, 159

Stamatellos D., Whitworth A. P., Ward-Thompson D., 2007c, MNRAS, 379, 1390

Stanke T., Smith M. D., Gredel R., Khanzadyan T., 2006, A&A, 447, 609

Steinmetz M., Mueller E., 1993, A&A, 268, 391

Tohline J. E., 1982, Fundamentals of Cosmic Physics, 8, 1

Toomre A., 1964, ApJ, 139, 1217

Truelove J. K., Klein R. I., McKee C. F., Holliman J. H., II, Howell L. H., Greenough J. A., Woods D. T., 1998, ApJ, 495, 821

Vrba F. J., 1977, AJ, 82, 198

Ward-Thompson D., André P., Crutcher R., Johnstone D., Onishi T., Wilson C., 2007, in Reipurth B., Jewitt D., Keil K., ed, Protostars and Planets V, p. 33

Ward-Thompson D., Motte F., Andre P., 1999, MNRAS, 305, 143

Ward-Thompson D., Scott P. F., Hills R. E., Andre P., 1994, MNRAS, 268, 276

Whitworth A. P., 1998, MNRAS, 296, 442

Whitworth A. P., Goodwin S. P., 2005, Memorie della Societa Astronomica Italiana, 76, 211

Whitworth A. P., Stamatellos D., 2006, A&A, 458, 817

Whitworth A. P., Zinnecker H., 2004, A&A, 427, 299

Wilking B. A., Lada C. J., Young E. T., 1989, ApJ, 340, 823

Wilking B. A., Meyer M. R., Greene T. P., Mikhail A., Carlson G., 2004, AJ, 127, 1131